Resonant Spin Flip Raman-Spectroscopy of Electrons and Manganese-Ions in the n-doped Diluted Magnetic Semiconductor (Zn,Mn)Se:Cl

Dissertation zur Erlangung des naturwissenschaftlichen Doktorgrades der Julius-Maximilians-Universität Würzburg

vorgelegt von

Alexander Gerhard Knapp

aus

Düsseldorf

Würzburg, 2018

Eingereicht am: 14. Dezember 2018
bei der Fakultät für Physik und Astronomie

1. Gutachter: Prof. Dr. J. Geurts
2. Gutachter: Prof. Dr. E. Batke
3. Gutachter: .....
der Dissertation.

Vorsitzende(r): .....

1. Prüfer: Prof. Dr. J. Geurts
2. Prüfer: Prof. Dr. E. Batke
3. Prüfer: .....
im Promotionskolloquium.

Tag des Promotionskolloquiums: .....

Doktorurkunde ausgehändigt am: .....

Contents

Introduction

For more than half a decade the mastery and optimization of semiconductors materials was one of the major factors of the technological achievements of our modern society. Semiconductor based electronic circuits are the key elements of each computer and modern devices, which we regularly encounter in our daily life. The number of these smart devices is expected to rapidly increase in the future, which boosts the development pressure of the semiconductor technology sector. Until today, most of the economically feasible circuits are using silicon as the main semiconductor material. To improve the computing efficiency of these devices, the fabrication of smaller sized electronic circuits is required, which has become a challenging task. Hence, alternative materials are attracting attention of ongoing studies and developments.

Materials, which empower not only the charge but also the spin properties of electrons, are potential candidates for the future technical development. The study of these materials is often referred to as spintronics, which is a combination of the two words spin and electronic. To enable semiconductor materials to have spin selective properties, atoms with a partially filled atomic shell are embedded within the semiconductor crystal. Transition metals like Fe, Mn, Co belong to this kind of materials, used as a magnetic substitute. The obtained new type of semiconductors is referred to as diluted magnetic semiconductors (DMS). When exposed to an external magnetic field, the total angular moment of the magnetic ion of the DMS aligns parallel to the field and as a result, drastically increases the magnetization of the material. Moreover, the exchange interaction of the aligned orbitals of these magnetic ions with the valence and conduction band states of the semiconductor leads to fascinating observable magneto optical effects like Faraday rotation and Voigt birefringence, as well as giant magneto resistance and spin selective transport. In 1999 Fiederling et al. were able to induce a pronounced spin polarized

current in GaAs by the use of the DMS $Be_xMn_yZn_{1-x-y}Se$ [FKR$^+$99]. This success created a huge interest in the scientific community on the research of DMS as a source for a spin current generator.
(Ga,Mn)As is the most widely known representative of DMS, due to the high Curie temperature T_c of about 170 K [NST03], which makes it a well-suited material to study the behavior of DMS. The disadvantage of (Ga,Mn)As is the fact that Mn acts as an acceptor in the III-V GaAs semiconductor. Hence, the incorporation of Mn not only affects the magnetic but also the electronic transport properties of GaMnAs, which is the major drawback of this DMS.

(Zn,Mn)Se overcomes this drawback, because manganese is isoelectric in the II-VI semiconductor ZnSe. This enables the independent modification of the magnetic properties, by choosing the amount of manganese and electronic transport characteristics, by the adjustment of the donor or acceptor doping concentration. This allows the study of the n-doped DMS (Zn,Mn)Se near the metal-insulator transition at a critical carrier concentration $n_c = 7 \cdot 10^{17} cm^{-3}$ of this transition, at independently chosen Mn concentrations [JWN$^+$14]. Jansson et al. performed magneto-transport measurements on a set of (Zn,Mn)Se:Cl with Mn concentrations ranging from 0% to 7.3% and doping concentrations between $1.9 \cdot 10^{17}$ cm^{-3} and $8.4 \cdot 10^{17}$ cm^{-3}. In their study, they observed a giant-magneto resistance for samples doped below the metal-insulator transition and explained the occurrence of this effect by a model of electrons hopping between states of different energy, due to locally different Mn concentrations.

To get a detailed understanding of the influence of the random distribution of Mn within the crystal on the donator wavefunctions, Raman spectroscopy on the identical samples studied by Jansson et al. is deployed in this thesis.
Raman spectroscopy is named after one of its discoverers Sir Chandrasekhara Venkata Raman, who observed this effect in 1928 by studying the optical properties of organic liquids [RK28]. For his work, he was awarded the Nobel price in physics in 1930. Raman spectroscopy is mostly known as a tool for the analysis of rotational and vibrational properties of molecules and condensed matter. Furthermore, Raman spectroscopy allows the study of mechanical strain within a crystal caused by external mechanical pressure or due to an internal tension, by the analysis of the phonon shift.
Beside these effects, this non-destructive optical technique can also be em-

ployed to get further insight on other low energy excitations. This is possible due to the creation of an electron hole pair as an intermediate step of the Raman process. The interaction of electron hole pair with different types of fundamental excitations allows the analysis of these excitations by Raman spectroscopy, for example of magnons or single particle stimulations of free and bound electrons.

Hence, Raman spectroscopy is a suitable technique to get further understanding of the behavior of the n-doped DMS (Zn,Mn)Se in an external magnetic field. In this thesis, Raman spectroscopy is utilized to measure the dynamics of the energy level distribution of the conduction band states at an external magnetic field and low temperatures. Due to the field-induced spin splitting, electron spin flips can be deployed for this purpose, and therefore, the used technique is referred as electron spin flip Raman scattering (ESFRS) [NPFG81] [HWW83]. This process shows a pronounced enhancement of the detected signal, when the excitation energy is tuned to fit to the energy difference of some valence and conduction bands [TMR$^+$04]. The occurring resonance profiles contain viable information about the density of states of the donor bound exciton (D^0, X) and free exciton (X^0) and are therefore analyzed in this thesis at magnetic fields ranging from 1 T to 7 T. Due to the localized characteristic of the donor bound exciton, the energy distribution for a set of (D^0, X) should depend on the statistics of the random distribution of the Mn [JBGO08]. This should lead to a widening of the resonance profile with increasing magnetic field, as will be confirmed in this thesis.
Furthermore, the spectral shape of the Raman signal from the electron spin flip process can also give new insights about the energy distribution of (D^0, X) and (X^0). Therefore, the shape of the Raman signal is analyzed in this thesis at different magnetic fields as well as variable excitation energies.
In addition, the obtained concentration distributions are utilized to determine the (D^0, X) and (X^0) radii. Thus electron spin flip Raman spectroscopy is suitable as a new method to investigate the volume of excitons in DMS.
Beside the studies of the electron spin flip, Raman scattering is used investigate the behavior of electron paramagnetic resonance of the manganese ions. Here, the resonance of the manganese spin flip and its combined process with the additional creation of the LO phonon are measured.
The thesis is composed of two main sections. In the fundamental part, the

theoretical basics of diluted magnetic semiconductor physics and Raman spectroscopy are introduced, with a focus on the resonance effects of Raman scattering and the optical setup and sample parameters are explained.
The second main section, in which the experimental results are presented and discussed, is divided into three chapters:

- Resonant electron spin flip Raman spectroscopy, in which the resonance profile of the ESFRS efficiency is studied. The obtained profiles consist of two overlapping resonance contributions, assigned to the (D^0, X) and (X^0) assisted spin flip process. The broadening of theses profiles with increasing B-field are described by a model, which is utilized to determine the radii of the (D^0, X) and (X^0).

- Shape analysis of the ESFRS profile: In this section, the ESFRS line shape at different excitation energies and external magnetic fields is studied, which is subsequently used as an alternative way to estimate the radii (D^0, X) and (X^0). These findings are compared with the results of the previous section.

- The direct and LO-assisted resonance of the Mn spin flip. Here, the experimental results of the paramagnetic resonance of the Mn spin flip and the combination process, which involves the additional creation of an LO phonon, are presented. The resonance profiles are studied and the optical transitions, responsible for the enhancement of the detected signal, are identified.

All obtained results are briefly summarized at the end of this thesis.

Part I

Fundamentals

Chapter 1

Diluted magnetic semiconductors

1.1 Fundamental properties of (Zn,Mn)Se

In this thesis, the electronic band structure and the electronic states of manganese of (Zn,Mn)Se with Cl doping concentrations up to $1.3 \cdot 10^{18}$ cm^{-3} and manganese concentrations of 0.01, 0.05, and 0.07 are studied by Raman spectroscopy. In the following section the fundamental properties of n-doped (Zn,Mn)Se are presented, with the focus on the electronic band structure near the fundamental band gap in an external magnetic field. Furthermore, the interaction of the individual Mn^{2+} ions with each other via the (d-d) super exchange and with the valence and conduction band states via the (s-d) and (p-d) exchange interaction is described.

1.1.1 Crystal structure of (Zn,Mn)Se

The II-VI semiconductor ZnSe usually crystallizes in the zincblende structure. In crystallographic terms, it is labeled as the $F\bar{4}3m$ space group and shows the T_d symmetry. The Zn^{2+} and the Se^{2-} ions form individual sublattices in a face centered cubic (fcc) crystal. The sublattices are shifted to each other by one quarter of the space diagonal. An fcc unit cell of ZnSe is visualized in Fig. 1.1 in a cubic structure. The lattice constant of ZnSe is $a_0 = 5.67$Å at room temperature [MMB80].
The ternary material $Zn_{1-x}Mn_xSe$ is formed by the partial substitution of Zn ions with Mn ions. The chemical concentration x of the Mn ions denotes the

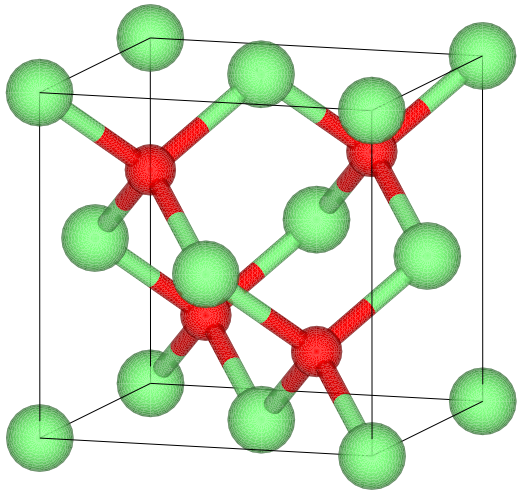

Figure 1.1: Zincblende crystal structure of ZnSe in cubic representation. Zn in green, Se in red. Image was generated with VESTA (Visualization for Electronic and Structural Analysis) [MI11].

relative quantity of Zn ions which are replaced by Mn ions, with the limits ZnSe for $x = 0.00$ and MnSe for $x = 1.00$. In contrast to ZnSe, MnSe crystallizes in wurtzite crystal structure. Consequently, $Zn_{1-x}Mn_xSe$ must undergo a transition from zincblende to wurtzite crystal structure. This occurs at a critical concentration x_{crit} of about 0.35 [LRA88] [YSDF85] [BBK$^+$86]. All samples which were studied in this thesis have a Mn concentration $x \leq 0.07$, which is well below x_{crit}. Therefore, the properties of $Zn_{1-x}Mn_xSe$ in zincblende structure are discussed in more detail.

In comparison to DMS based on III-V semiconductor materials, Mn^{2+} ions on the zinc sublattice behave isoelectronic, due to the outer $4S^2$ shell of Mn. Hence Mn does not act as an acceptor or donor in ZnSe. The half filled $3D^5$ shell of Mn^{2+} results in a total net spin of 5/2, which is responsible for the unique properties of diluted magnetic semiconductor (DMS) in a magnetic field.

It is well known that the lattice constant depends on the concentration of the substituted material. According to Vegard's law the lattice constant can be estimated by a linear interpolation [YSDF85]:

$$a_{A_{1-x}B_x} = (1-x) \cdot a_A + x \cdot a_B = 5.667\text{Å} + 0.233\text{Å} \cdot x \tag{1.1}$$

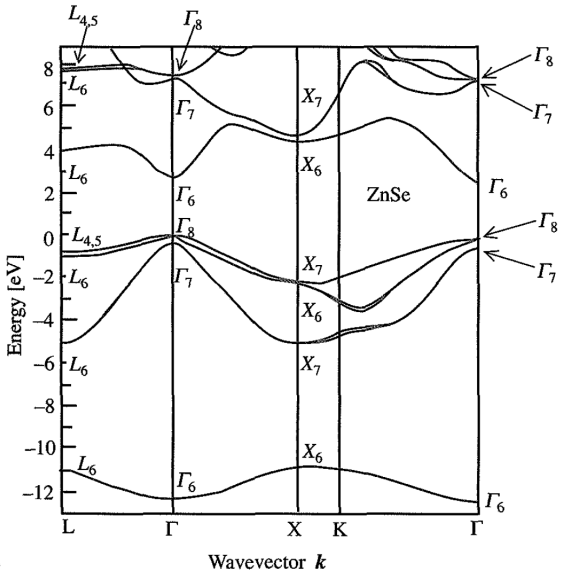

Figure 1.2: Electronic band structure of ZnSe, calculated by the pseudopotential method [CC88]. The fundamental band gap $E_0 \approx 2.8\,\mathrm{eV}$ is located at the Γ point between the Γ_8 valence band and the Γ_6 conduction band.

with $a_A = 5.667$Å the lattice constant of ZnSe, $a_B = 5.9$Å the lattice constant of cubic MnSe and $a_{A_{1-x}B_x}$ the lattice constant of the ternary material. For the samples, studied in this thesis, the lattice constants caluated by Eq. (1.1) are: $a_{A.99B.01} = 5.669$ Å; $a_{A.95B.05} = 5.679$ Å; and $a_{A.93B.07} = 5.683$Å, which leads to a mismatch between the lattice constants of $Zn_{1-x}Mn_xSe$ and the GaAs ($a_{GaAs} = 5.65$ Å) substrate of up to 0.6% [MRS01]. The mismatch induces a lateral compression of the $Zn_{1-x}Mn_xSe$ layer, which can affect the electronic and vibrational properties of the layer. The studied samples consists of a layer with a thickness of about 1 μm, which is equal to 2000 unit cells. At this layer thickness, the lattice is completely relaxed [GPK90]. The light penetration depth at photon energies above the fundamental band gap of $E_0 = 2.80\,\mathrm{eV}$ in ZnSe is as low as 100 nm [Geu93]. Therefore, the effect caused by strain has no significant influence on the Raman spectroscopy studies of the sample set presented in this thesis.

1.1.2 Electronic band structure of ZnSe and (Zn,Mn)Se

ZnSe is a direct band gap semiconductor, with the fundamental band gap energy $E_0 = 2.798\,\mathrm{eV}$ at $T = 6.5\,\mathrm{K}$ at the Γ point, i.e. $\vec{k} = 0$ [BBK$^+$86]. Fig. 1.2 shows a visualization of the ZnSe band structure, calculated by the

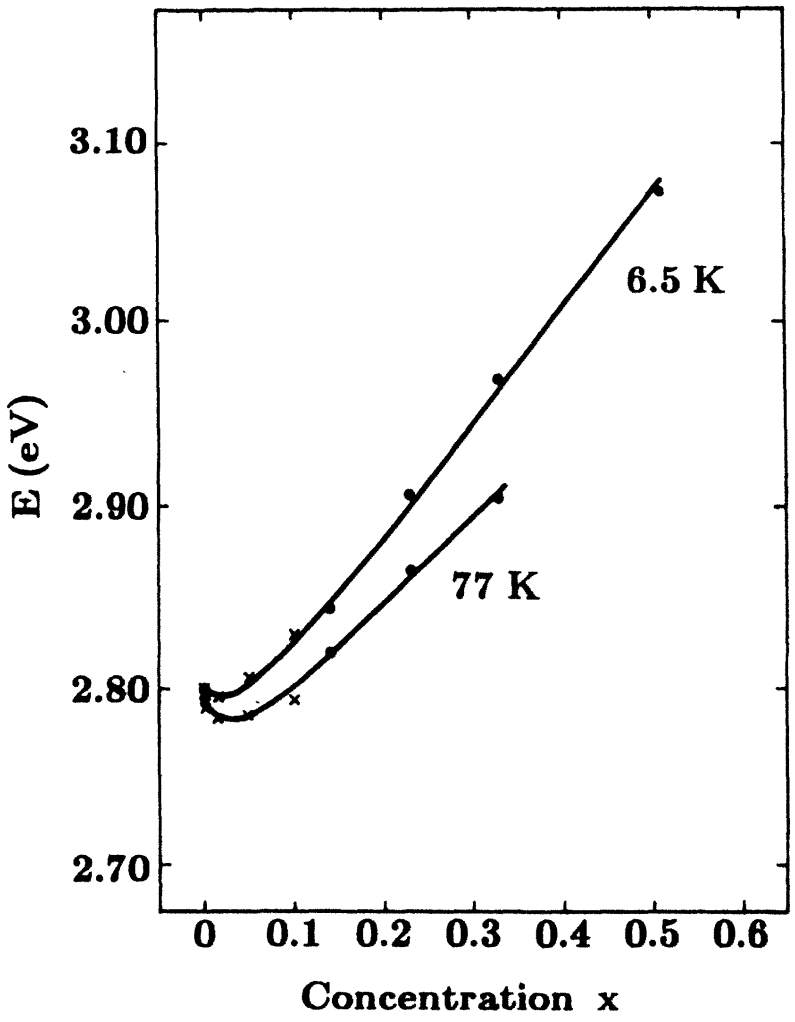

Figure 1.3: E_0 gap energy versus Mn concentration x in $Zn_{1-x}Mn_xSe$. The non linear trend of E_0 is observed in the x range from 0.00 to 0.15 [BBK$^+$86].

pseudopotential method [CC88]. The wave vector of the photons for Raman experiments is in the order of 10^5 cm^{-1}, which is about 1000 times smaller than the Brillouin zone. Hence, in a good approximation, optical transitions can be seen as vertical paths on the scale of the Brillouin zone. The Raman experiments presented in this thesis are based on optical transitions at the Γ point from the Γ_8 valence band (VB) to the Γ_6 conduction band (CB). In the following section, the properties of the two bands are described more detail.

The valence band originates primarily from 4p-orbitals of Se, therefore, it is often referred as a "p-like" band. Due to the spin orbit coupling, this band splits into the previously mentioned Γ_8 quartet and a Γ_7 doublet. The degeneracy

of these band levels is according to their total angular momentum quantum number J, thus Γ_8 is fourfold degenerated with $J = 3/2$ and Γ_7 two times with $J = 1/2$. The energy separation between Γ_8 and Γ_7 is $\Delta = 430\,\mathrm{meV}$ [WGR+97]. The Γ_7 is the energetically lower band and labeled as the split off band. This band is not subject to the optical studies of this thesis, because of its significant offset and therefore, is not further considered for the analysis of the experimental results.

For $\vec{k} \neq 0$ the Γ_8 band separates into two subbands with different curvature. The curvature of each subband is inversely proportional to the effective mass of its carriers. Due to the difference in mass, the subbands are referred as the heavy and light hole band, with the masses $m_{hh} = 1.1 \times \mathrm{m}_e$ and $m_{lh} = 0.2 \times \mathrm{m}_e$. The z-components of the total angular momenta are $J_z = \pm 3/2$ for the heavy hole band and $J_z = \pm 1/2$ for the light hole band.

The Γ_6 conduction band results by a superimposition of the 4s-orbitals of the Zn cations. Hence the angular momentum L is zero and only the spin momentum $S = 1/2$ remains and yields a total angular momentum J of $1/2$. The Γ_6 band states have a spherical symmetry, because $L = 0$ and consequently no splitting into subbands for $\vec{k} \neq 0$ occurs.

The band gap of wurtzit MnSe is $E_0 \approx 3.3\,\mathrm{eV}$ to $3.4\,\mathrm{eV}$ [HGT+93] [BBK+86], which is about $0.5\,\mathrm{eV}$ higher than the E_0 gap of ZnSe and consequently, the band gap energy of $\mathrm{Zn}_{1-x}\mathrm{Mn}_x\mathrm{Se}$ depends on the chemical Mn concentration x. In contrast to the Vegard's law, used for the determination of the lattice constant of the ternary crystal, Bylsma et al. observed a non linear trend of the E_0 band gap on x [BBK+86], shown in Fig. 1.3. Here, it can be seen that the minimum of E_0 does not occur at $x = 0$, instead it is located at a chemical concentration of about $x \approx 0.03$. This behavior is explained by the (p-d) exchange interaction, between the d-states of the Mn ions and the p-like VB states.

The Mn ion concentration of the sample set studied in this thesis is in the range of $0.01 \leq x \leq 0.07$. Thus the expected E_0 gap is estimated by the data shown in Fig. 1.3 to be (2.80 ± 0.02) eV for all samples.

1.2 Magnetization of diluted magnetic semiconductors

The magnetic properties of a diluted magnetic semiconductor (DMS) are modified by an incorporation of a small amount of magnetic materials in the crystal, e.g. manganese in ZnSe. The magnetic elements have a non completely filled electron shell, yielding a total angular moment $J \neq 0$. The $3d^5$ shell of Mn^{2+} ion in ZnSe is half filled, which results in $L = 0$, $S = 5/2$ and therefore $J = 5/2$ ground state. For a concentration of magnetic ions $x \leq 0.01$ the magnetic ions interact with an external magnetic field as independent magnetic dipoles. Therefore, this interaction can be described by an atomic paramagnetism. The Hamiltonian of the paramagnetic interaction reads as follows:

$$\hat{H}_{para} = \mu_B \cdot g_J \cdot \vec{J} \cdot \vec{B} \tag{1.2}$$

with the Bohr magneton μ_B and the Landé g-factor:

$$g_J = 1 + \frac{J(J+1) + S(S+1) - L(L+1)}{2J(J+1)} \tag{1.3}$$

The z-component $J_z \parallel B$ can be classified by the second total angular momentum quantum number $m_J \in \{J, J-1, ..., -J+1, -J\}$. The partition function Z of the system is the sum of all states:

$$Z = \sum_{m_J=-J}^{J} exp\left[- m_J \frac{g_J \mu_B \cdot B}{k_B T} \right] \tag{1.4}$$

and a parameter $y(B)$ is defined as:

$$y(B) = \frac{g_J \mu_B \cdot B}{k_B T} \cdot J \tag{1.5}$$

Substituting Eq. (1.5) into Eq. (1.4) allows to simplify Z by a hyperbolic function:

$$Z = \sum_{m_J=-J}^{J} exp\left[\frac{-m_J \cdot y}{J} \right] = \frac{sinh(\frac{2J+1}{2J} y)}{sinh \frac{y}{2J}} \tag{1.6}$$

The dependence of the thermodynamic free energy F on the partition function is:

$$F = -Nk_BT \cdot ln(Z) \tag{1.7}$$

And the magnetization M can be expressed as:

$$M(y) = -\frac{1}{V}\frac{\partial F}{\partial B} = \underbrace{x \cdot g_J\mu_B J}_{M_S} \cdot \underbrace{\left[\frac{2J+1}{2J}coth\left(\frac{2J+1}{2J}y\right) - \frac{1}{2J}coth\left(\frac{y}{2J}\right)\right]}_{\equiv B_J(y)} \tag{1.8}$$

Where x = N/V is the density of the magnetic ions. The limit of $M(y)$ for $B \to \infty$ yields the saturation magnetization M_S as follows:

$$M_S = x \cdot g_J\mu_B J \tag{1.9}$$

The second term in Eq. (1.8) is the Brillouin function $B_J(y)$, defined by:

$$B_J(y) = \frac{2J+1}{2J}coth\left(\frac{2J+1}{2J}y\right) - \frac{1}{2J}coth\left(\frac{y}{2J}\right) \tag{1.10}$$

When no external B-field is applied, $B_J(0) = 0$, thus the magnetization M is also zero. For the limit $B_J(y \to \infty) = 1$, resulting in a magnetization equal to its saturation value M_S.
Beside the behavior of B_J for the two external B-field limits, there are two special cases which can be described by the universal Brillouin function $B_J(y)$. The pure spin magnetization with $J = 1/2$

$$B_{1/2}(y) = 2 \cdot coth(2y) - coth(y) = \frac{1 + coth^2(y)}{coth(y)} - coth(y) = tanh(y) \tag{1.11}$$

and the classical limit with $J \to \infty$

$$B_\infty(y) = coth(y) - \frac{1}{2J}\frac{2J}{y} = coth(y) - \frac{1}{y} \equiv L(y) \tag{1.12}$$

which is known as the Langevin function. For the studied DMS (Zn,Mn)Se J is 5/2 and therefore $B_{5/2}(y)$ is plotted in addition to the Brillouin function of the two cases $J = 1/2$ and $y \to \infty$ in Fig. 1.4 a). The slope of the Brillouin

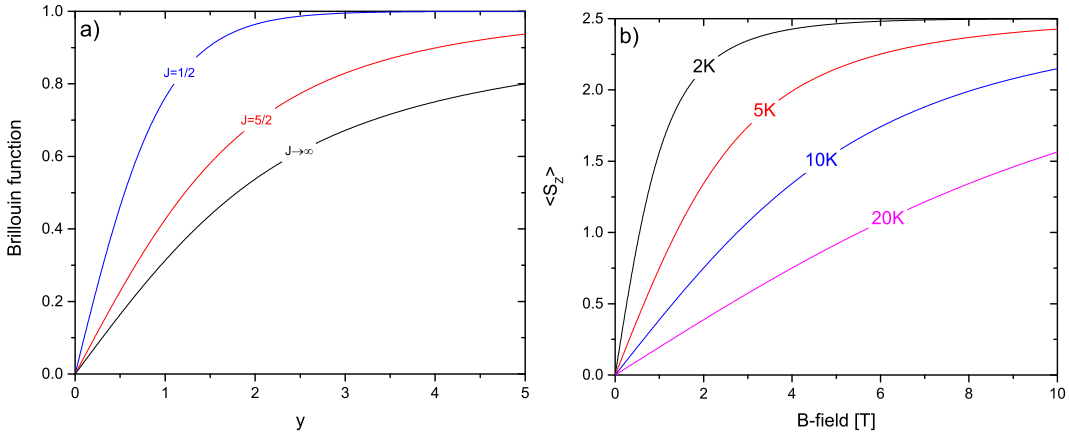

Figure 1.4: a) Brillouin function $B_J(y)$ for three different J values. blue: pure spin magnetism with $J = 1/2$, black: classical limit with $J \to \infty$ and red: $J = 5/2$ representing the spin alignment of Mn^{2+} ions in an external B-field. b) B-field dependence of the expectancy value of the total spin $\langle S_Z \rangle$ with $J = 5/2$ for the temperature T ranging from 2 K to 20 K.

function decreases with increasing J value, however, the saturation value of one for $y \to \infty$ is independent of J.

For magneto optical experiments the expectancy value of the z-component of the total spin $\langle S_z \rangle$ which is typically used as a parameter to describe the magnetic properties of DMS in an external magnetic, reads as follow:

$$\langle S_z \rangle(y) = -J \cdot B_J(y) \tag{1.13}$$

For (Zn,Mn)Se, $g_{Mn} = 2$ and $J = 5/2$ and $\langle S_z \rangle$ becomes:

$$\langle S_z \rangle(B,T) = -\frac{5}{2} B_{5/2}\left(\frac{5}{2}\frac{\mu_B g_{Mn} B}{k_B T}\right) = 3coth\left(6\frac{\mu_B B}{k_B T}\right) - \frac{1}{2}coth\left(\frac{\mu_B B}{k_B T}\right) \tag{1.14}$$

Here, the temperature T and the external magnetic field B are the two experimentally variable parameters to adjust $\langle S_z \rangle$. This can be interpreted as an ordering effect, generated by the B-field, which aligns the magnetic moments of the individual Mn ions. On the other hand, there is a disordering effect, caused by the increase of the thermal energy $k_B T$ of the Mn spin system, thus leading to a more random distribution of the Mn spin orientation.
The $\langle S_z \rangle$ for (Zn,Mn)Se at temperatures ranging from 2 K up to 20 K versus the external B-field are plotted in Fig. 1.4 b). It can be seen that with increas-

ing temperature, a higher B-field is required to achieve the identical degree of the spin orientation, i.e. identical $\langle S_Z \rangle$ value. This shows that the crystal temperature is a crucial parameter for the magnetization of the sample and therefore, all Raman experiments were performed in a helium bath cryostat at temperatures below 2 K.

1.3 Antiferromagnetic interaction between d-electrons and neighboring Mn ions

Indirect exchange interaction of Mn^{2+} ions mediated by hopping electrons between neighboring atoms has a non neglectable influence on the magnetic ground state of the system. One of these interactions is the so called super exchange, which can be described by a second order correction of the perturbation theory. This section will give a qualitative description of this effect. A detailed explanation can be found in literature [BS92].
When the concentration of the Mn ions x is above 0.01 the interaction between the Mn ions is non negligible and the ions cannot be described as isolated atoms within the lattice. The interaction between the d-electrons of the Mn ions is mediated by the electron of the Se ion, which is located between the interacting neighboring Mn ions. Assuming two Mn ions 1 and 2 with the spin components $S_{1,\alpha}$ and $S_{2,\beta}$ at the positions $\vec{R}_1$ and $\vec{R}_2$, the Hamiltonian of the (d-d) exchange interaction can be written as [LE89]:

$$\hat{H}_{d-d} = -\sum_{\alpha,\beta} \vec{S}_{1,\alpha} J_{\alpha,\beta}(\vec{R}_{12}) \vec{S}_{2,\beta} = \hat{H}_{iso} + \hat{H}_{asym} \tag{1.15}$$

where $J_{\alpha,\beta}$ denotes the interaction strength and $\vec{R}_{12}$ the distance $(\vec{R}_1 - \vec{R}_2)$ of the two Mn ions. The Hamiltonian can be separated into an isotropic $\hat{H}_{iso}$ and an asymmetric $\hat{H}_{asym}$ part The isotropic Hamiltonian is called Heisenberg Hamiltonian and the interaction strength $J(\vec{R}_{12})$ can be expressed as [GK10]:

$$\hat{H}_{iso} = -J(\vec{R}_{12}) \vec{S}_1 \cdot \vec{S}_2 \tag{1.16}$$

The interaction strength of the (d-d) interaction between neighboring Mn ions on the Zn-sublattice of ZnSe amounts to $J_{NN}/k_B = -12.6\,\mathrm{K}$ [SO87] and for the

(d-d) interaction of next nearest neighbors to $J_{NNN}/k_B = -2.4\,\mathrm{K}$ [Fur88]. The negative algebraic sign indicates that both interactions are antiferromagnetic. This reduces the magnetization of the DMS caused by the spin orientation of the Mn ions, compared to the assumption that only non-interacting Mn ions are considered.
The asymmetric part $\hat{H}_{asym}$ is caused by the spin orbit interaction, which excites one of the two neighboring Mn ions. This excited state interacts with the ground state of the other Mn ions. The anisotropic interaction is called Dzyaloshinskii-Moriya interaction and can be written as follows [Mor60]:

$$\hat{H}_{asym} = -\vec{D}(\vec{R}_{12}) \cdot (\vec{S}_1 \times \vec{S}_2) \tag{1.17}$$

If the crystal field has an inversion symmetry with respect to the two Mn ions, the interaction vector $\vec{D}(\vec{R}_{12})$ vanishes. For a non-vanishing $\hat{H}_{asym}$ the interaction vector $\vec{D}(\vec{R}_{12})$ is not in the plane spanned by $\vec{S}_1$ and $\vec{S}_2$, resulting in a weak ferromagnetic moment perpendicular to this plane. In most cases, the isotropic interaction dominates the asymmetric part and therefore, the Dzyaloshinskii-Moriya interaction can be neglected.
To include the antiferromagnetic interaction, instead of the chemical concentration x, an effective concentration x_{eff} is used as a relevant parameter to describe the observation of magneto Raman experiments. This is necessary, to consider the formation of pairs of neighboring Mn ions and also of larger Mn clusters, which decreases the magnetically active amount of Mn ions. Hence, the modified magnetization for (Zn,Mn)Se can be expressed as:

$$M(B,T) = 5 \cdot x_{eff} \cdot \mu_B \cdot B_{5/2}\left(\frac{5\mu_B B}{k_B[T + T_{AF}(x)]}\right) \tag{1.18}$$

where $T_{AF}(x)$ is a phenomenological parameter. To my knowledge no model, based on theoretical predictions, exists to dertermine of the phenomenological temperature T_{AF}. Keller et al. approximated the obtained T_{AF} for x ranging from 0.00 to 0.15 by a polynomial of third grade, resulting in [KYK+01]:

$$T_{AF}(x) = 47.2 \cdot x - 281 \cdot x^2 + 714 \cdot x^3 \tag{1.19}$$

For the Mn concentrations of the set of samples studied in this theses, the $T_{AF}(x)$ values are: $T_{AF}(0.01) = 0.4\,\mathrm{K}$; $T_{AF}(0.05) = 1.8\,\mathrm{K}$; $T_{AF}(0.07) = 2.2\,\mathrm{K}$.

1.3.1 Determination of the effective Mn concentration x_{eff}

As stated above, due to the antiferromagnetic interaction between the magnetic ions, for magneto optical experiments instead of the chemical concentration x the effective concentration x_{eff} must be taken into account to describe the magnetic properties of the DMS in an external magnetic field. In the following section, a theoretical model to calculate $x_{eff}(x)$ is presented.
The interaction strength of the (d-d) super exchange indicates that the nearest neighboring interaction is much larger than the next nearest neighboring interaction (see previous section). This enables the approximation to calculate the effective Mn concentration x_{eff} by the determination of the Mn cluster formation purely considering interactions between nearest neigboring Mn ions [SFR$^+$84]. Assuming that the Mn ions are randomly incorporated on the cation sites of the ZnSe fcc lattice, with a chemical concentration x, the probabilities that a Mn ion is isolated (single) or belongs to a pair, an open triangle (OT) or a closed triangle (CT) are [Beh58]:

$$\text{single:}\quad P_1(x) = (1-x)^{12} \tag{1.20}$$

$$\text{pair}\quad :\quad P_2(x) = 12x\cdot(1-x)^{18} \tag{1.21}$$

$$\text{OT}\quad :\quad P_3(x) = 18x^2\cdot(7-5x)(1-x)^{23} \tag{1.22}$$

$$\text{CT}\quad :\quad P_4(x) = 24x^2\cdot(1-x)^{22} \tag{1.23}$$

Beside the probabilities, the saturation magnetization of each cluster in respect to the single Mn ion must be considered to determine x_{eff}. For a single Mn ion the relative magnetization is one, because no antiferromagnetic interaction takes place. The pair couples antiferromagnetically, thus reducing the saturation to zero. For the open triangle, the spin of two of the three Mn ions cancel each other out and one single Mn spin is effectively soley, which lowers the saturation value of the cluster to one third of the saturation magnetization of three single magnetic ions. The saturation of the closed triangle is 1/15 of the saturation magnetization of three single atoms, because no perfect antiferromagentic ordering can be achieved and the spins are frustrated. A detailed explanation for the factor 1/15 can be found in literature [SFR$^+$84] [NGM$^+$80].
Combining the probabilities with the relative saturation allows the calculation

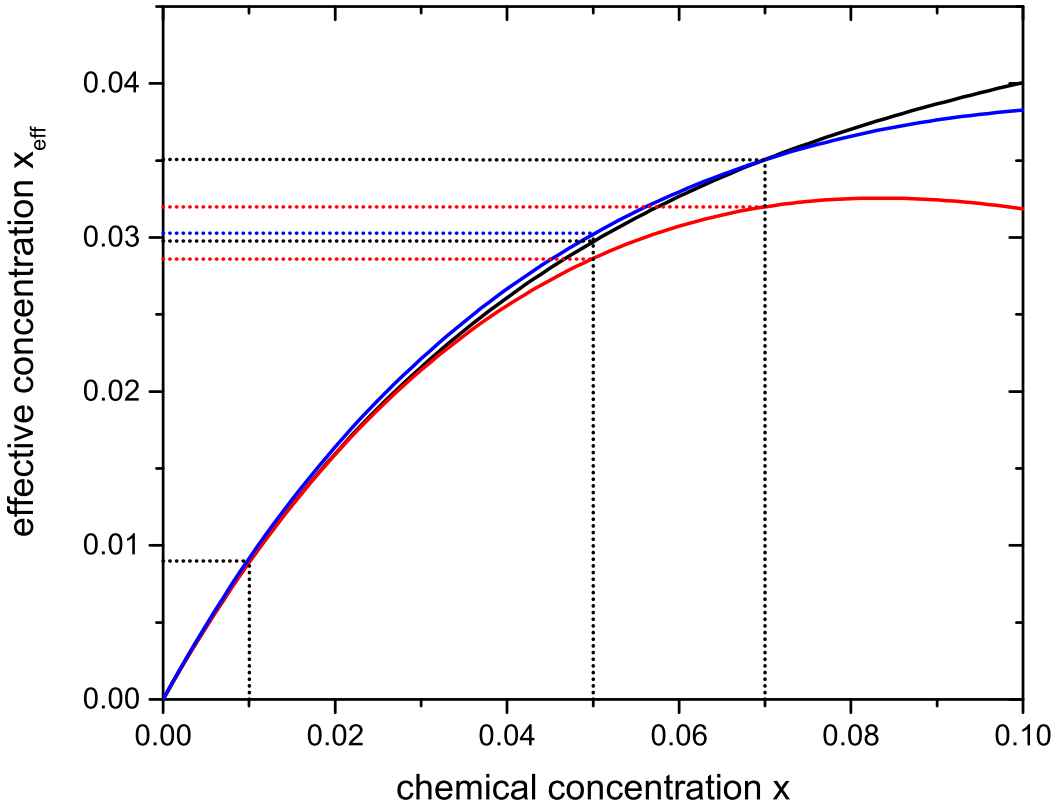

Figure 1.5: Transition from the chemical Mn concentration x to the effective concentration x_{eff}, according to Eq. (1.25) (black), Eq. (1.24) (red) and calculations by Keller et al. (blue) [KYK+01]. The black dashed vertical lines mark the Mn concentrations of the studied sample set (x = 0.01; x = 0.05; x = 0.07) and the horizontal dashed lines the corresponding x_{eff} values, calculated for each transformation.

of x_{eff}:

$$x_{eff}(x) = x \cdot [P_1(x) + 0 \cdot P_2(x) + \frac{1}{3}P_3(x) + \frac{1}{15}P_4(x)] \qquad (1.24)$$

Shapira et al. observed a deviation of the predicted x_{eff} with experimentally observed values above $x > 0.08$. In this case, the formation of clusters with four or even more Mn ions must be taken into account. The probability P_5 for larger clusters is estimated by the converse probability, i.e. $P_5(x) = [1 - P_1(x) - P_2(x) - P_3(x) - P_4(x)]$ and the saturation strength is 1/5. Thus, Eq. (1.24) is modified for $x > 0.08$ to:

$$x_{eff}(x) = x \cdot [P_1(x) + 0 \cdot P_2(x) + \frac{1}{3}P_3(x) + \frac{1}{15}P_4(x) + \frac{1}{5}P_5(x)] \qquad (1.25)$$

Beside this model, based on a random distribution of the Mn ions, calculations of x_{eff} based on experimental observations and simple interpolations also exist. For a comparison, the x_{eff} values predicted by Eqs. (1.24) and (1.25) and an experimentally obtained interpolation by Keller et al. ($x_{eff} = -0.3216 \cdot x + 0.1472 \cdot x/(x+0.109)$) are plotted in Fig. 1.5. For chemical concentrations up to 0.01, all curves show an almost identical linear trend. For larger concentrations, the curves diverge from this trend and above $x = 0.04$ the transformation according to Eq. (1.24) starts noticeably to separate from the other two curves and the distinction becomes more striking for even larger x concentrations.

1.4 Interaction between d-electrons of Mn^{2+} ions and valence- and conduction band electrons

To study the magnetic properties of DMS, a suitable description of the interaction between the electrons of the magnetic Mn^{2+} ions and the valence and conduction band electrons must be given. In (Zn,Mn)Se, this interaction of the "p-like" valence band and the "s-like" conduction band states with the d-electrons of the Mn^{2+} ions can be expressed by the $\hat{H}_{s/p-d}$ Hamiltonian [Liu61]:

$$\hat{H}_{s/p-d} = -\sum_j J_{s/p-d}(\vec{r} - \vec{R}_j)\vec{S}_j \cdot \vec{\sigma} \tag{1.26}$$

where $J_{s/p-d}$ denotes the exchange strength of (s/p-d) interaction between the d-electrons of the Mn^{2+} ions and the band electrons. $\vec{S}_j$ represent the total spin and $\vec{R}_j$ the position vector of the j-th Mn^{2+} ion. The band electron is located at position $\vec{r}$ with spin σ. For a typically sized sample, the number of Mn ions is in the range of 10^{20} and consequently the calculation of the sum is not possible.

Instead, the Hamiltonian is simplified by the assumption that the band electrons are delocalized, to enable the use of the mean field approximation. Here, the spin $\vec{S}_j$ of the individual Mn ions is replaced by the expectancy value $\langle S_z \rangle$. Furthermore the virtual crystal approximation can be applied. In this case, the sum in Eq. (1.26) is extended to include all cation sites, and not only those which are occupied by magnetic ions. Consequently, this sum must then be

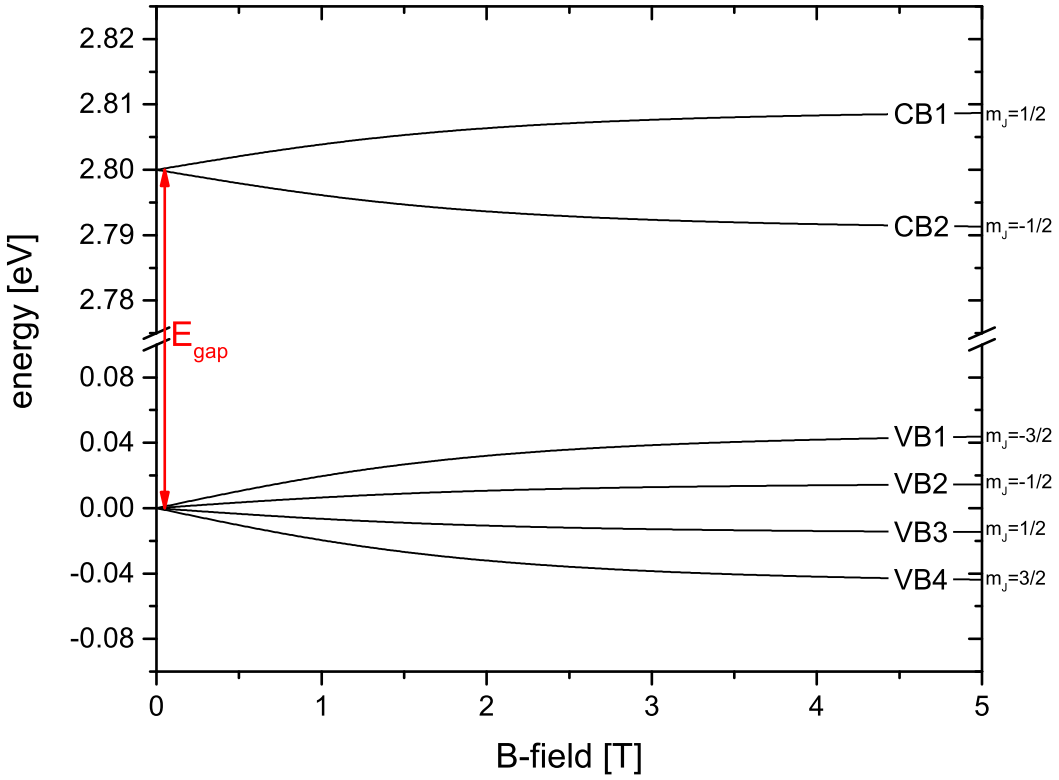

Figure 1.6: Calculated valence band (VB) and conduction band (CB) spitting for $Zn_{.95}Mn_{.05}Se$ in an external B-field. The bands separate into subbands according to their respective m_J quantum number.

multiplied by the Mn concentration x to yield the identical result as the sum in Eq. (1.26). The simplified Hamiltonian is written in the following form:

$$\hat{H}_{s/p-d} = -x\langle S_z\rangle\sigma_z \sum_i J_{s/p-d}(\vec{r} - \vec{R}_i) \tag{1.27}$$

The Luttinger theory [Lut55] enables to find a basis which diagonalized the Hamiltonian $\hat{H}_{s/p-d}$ for all valence band and conduction band state simultaneously. The obtained diagonalizes $\hat{H}_{s/p-d}$ yields the splitting of the Γ_8 VB and Γ_6 CB as follows:

$$\Delta E_{\Gamma_8} = \frac{1}{3} m_J \cdot N_0\beta \cdot x_{eff}\langle S_z\rangle \text{ with } m_J = \pm\frac{1}{2}, \pm\frac{3}{2} \tag{1.28}$$

$$\Delta E_{\Gamma_6} = m_J \cdot N_0\alpha \cdot x_{eff}\langle S_z\rangle \text{ with } m_J = \pm\frac{1}{2} \tag{1.29}$$

Twardowski et al. experimentally determined the exchange constants $N_0\alpha$ and $N_0\beta$ of the interaction for (Zn,Mn)Se [TODP84]:

$$N_0\alpha = 260meV \quad \& \quad N_0\beta = -1310meV \tag{1.30}$$

The Coulomb contribution to the exchange interaction of the CB electrons with the d-electrons of the Mn^{2+} ions is ferromagnetic, hence the spins of the carriers orientate parallel to the Mn spin. This is indicated by the positive value of $N_0\alpha$.

A second contribution to the interaction is the hybridisation of the 3d states of the Mn^{2+} ions with the s-CB and p-VB states. Due to symmetry arguments, the (s-d) hybridisation is forbidden [Fur88]. The (p-d) hybridisation results in an antiferromagnetic contribution to the (p-d) exchange interaction, which dominates this term and yields a negative $N_0\beta$ value [BFC83]. Fig. 1.6 shows the calculated splitting of the CB and VB levels for $Zn_{0.95}Mn_{0.05}Se$ according to Eqs. (1.29) and (1.28) at a B-field ranging from 0 T to 5 T. The energy levels have a Brillouin like behavior, caused by the alignment of the Mn spin with increasing B-field and hence, an enhanced strength of the (s/p-d) interaction. This is also reflected in the dependence of the photoluminescence and electron spin flip energy, described in the next chapter.

Chapter 2

Raman spectroscopy

Raman spectroscopy is a non invasive optical method, based on the inelastic scattering of light on molecules and crystals, to study a large variety of fundamental properties. It can be used to get further insight into vibrational properties, mechanical strain on the material, crystal purity of the sample, and also into single particle and quasi particle physics. Hence, Raman spectroscopy finds applications in many scientific fields, for example physics, chemistry, biology and material science.
In this thesis, Raman spectroscopy is applied to analyze the electron and manganese spin flip under resonance condition. Therefore, the macroscopic and microsopic theory of Raman scattering is described in this chapter and subsequently the resonant spin flip Raman scattering process for the CB electrons and manganese ions are explained.

2.1 Macroscopic theory of Raman scattering

In the following section, Raman scattering is derived by a macroscopic theory, based on the wave characteristics of light. The electric field of a harmonic electromagnetic plane wave can be described by:

$$\vec{E}(\vec{r},t) = \vec{E_i}(\vec{k_i},\omega_i) \cdot cos(\vec{k_i} \cdot \vec{r} - \omega_i t) \tag{2.1}$$

with the amplitude $\vec{E_i}$, wave vector $\vec{k_i}$ and angular frequency ω_i. In a medium, the electric field induces a polarization $\vec{P}(\vec{r},t)$:

$$\vec{P}(\vec{r},t) = \vec{P_i}(\vec{k_i},\omega_i) \cdot cos(\vec{k_i} \cdot \vec{r} - \omega_i t) \tag{2.2}$$

with same angular frequency ω_i and wave vector $\vec{k_i}$ as those of the incident radiation. For an isotropic medium, the electric susceptibility χ can expressed as a scalar and the amplitude of the polarization $\vec{P_i}$ is proportional to χ and the amplitude of the driving electric field:

$$\vec{P_i}(\vec{k_i}, \omega_i) = \epsilon_0 \chi(\vec{k_i}, \omega_i) \cdot \vec{E_i}(\vec{k_i}, \omega_i) \tag{2.3}$$

At a finite temperature, the atoms are thermally excited, which manifest itself in vibrations of these atoms. These vibrations can be described as displacements $\vec{Q}(\vec{r}, t)$ of the atoms with respect to their equilibrium state, which is expressed as:

$$\vec{Q}(\vec{r}, t) = \vec{Q}(\vec{q}, \omega_0) \cdot cos(\vec{q} \cdot \vec{r} - \omega_0 t) \tag{2.4}$$

ω_0 denotes the phonon frequency and $\vec{q}$ the wave vector. Theses atomic vibrations will modify χ, i.e. χ is a function of $\vec{Q}(\vec{r}, t)$. The displacement $\vec{Q}(\vec{r}, t)$ of the atoms is small compared to the lattice constant, which justifies the expansion of χ as a Taylor series in $\vec{Q}(\vec{r}, t)$:

$$\chi(\vec{k_i}, \omega_i, \vec{Q}) = \chi_0(\vec{k_i}, \omega_i) + \left(\frac{\partial \chi}{\partial \vec{Q}}\right)_0 \vec{Q}(\vec{r}, t) + ... \tag{2.5}$$

χ_0 is the electric susceptibility of the medium without fluctuations. The oscillating susceptibility induced by the lattice wave $\vec{Q}(\vec{r}, t)$ is represented by the second term. Substituting the expression for $\chi(\vec{k_i}, \omega_i, \vec{Q})$ and $\vec{P_i}(\vec{k_i}, \omega_i)$ into Eq. (2.2) describes the E-field-induced polarization of the medium considering the displacement of the atoms:

$$\vec{P}(\vec{r}, t, \vec{Q}) = \epsilon_0 \left[\chi_0(\vec{k_i}, \omega_i) + \left(\frac{\partial \chi}{\partial \vec{Q}}\right)_0 \vec{Q}(\vec{r}, t)\right] \cdot \vec{E_i}(\vec{k_i}, \omega_i) \cdot cos(\vec{k_i} \cdot \vec{r} - \omega_i t) \tag{2.6}$$

This can be separated into $\vec{P_0}(\vec{r}, t)$, a polarization vibrating in phase with the incident radiation, and $\vec{P}_{ind}(\vec{r}, t, \vec{Q})$, a polarization contribution which is modulated by the phonon.

$$\vec{P_0}(\vec{r}, t) = \epsilon_0 \chi_0(\vec{k_i}, \omega_i) \cdot \vec{E_i}(\vec{k_i}, \omega_i) \cdot cos(\vec{k_i} \cdot \vec{r} - \omega_i t) \tag{2.7}$$

$$\vec{P}_{ind}(\vec{r}, t, \vec{Q}) = \epsilon_0 \left(\frac{\partial \chi}{\partial \vec{Q}}\right)_0 \vec{Q}(\vec{r}, t) \cdot \vec{E_i}(\vec{k_i}, \omega_i) \cdot cos(\vec{k_i} \cdot \vec{r} - \omega_i t) \tag{2.8}$$

To identify the frequency and wave vector of $\vec{P}_{ind}(\vec{r},t,\vec{Q})$, Eq. (2.4) is substituted into Eq. (2.8)

$$\begin{aligned}\vec{P}_{ind}(\vec{r},t,\vec{Q}) =&\epsilon_0 \left(\frac{\partial\chi}{\partial\vec{Q}}\right)_0 \vec{Q}(\vec{q},\omega_0) \\ &\cdot cos(\vec{q}\cdot\vec{r}-\omega_0 t)\cdot\vec{E}_i(\vec{k_i},\omega_i)\cdot cos(\vec{k_i}\cdot\vec{r}-\omega_i t)\end{aligned} \tag{2.9}$$

$$\begin{aligned}=&\epsilon_0\cdot\frac{1}{2}\left(\frac{\partial\chi}{\partial\vec{Q}}\right)_0 \vec{Q}(\vec{q},\omega_0)\vec{E}_i(\vec{k_i},\omega_i) \\ &\cdot\{cos[(\vec{k_i}+\vec{q})\vec{r}-(\omega_i+\omega_0)t] \\ &+cos[(\vec{k_i}-\vec{q})\vec{r}-(\omega_i-\omega_0)t]\}\end{aligned} \tag{2.10}$$

$\vec{P}_{ind}$ consists of two contributions, a Stokes shifted harmonic wave with wave vector $\vec{k}_s=\vec{k}_i-\vec{q}$ and frequency $\omega_s=\omega_i-\omega_0$ and an anti-Stokes shifted wave with $\vec{k}_{as}=\vec{k}_i+\vec{q}$ and $\omega_{as}=\omega_i+\omega_0$. The Stokes process is the creation of a phonon, consequently the frequency of the Stokes shifted wave is lowered, whereas the anti-Stokes process is the annihilation of a phonon, increasing the frequency in respect to the incident wave frequency.

In a Raman experiment, a visible laser is tyically used as the light source. Therefore the wave vector of the incident light is of the order of 10^5 cm^{-1}, which is 1/1000 of the size of the Brillouin zone in a semiconductor. For the scattering process the wavevector and the energy are conserved. Consequently the wave vector q of the phonon must be smaller than twice the photon wave vector and hence one-phonon Raman scattering probes only Brillouin zone-center phonons.

Besides one-phonon Raman processes multi-phonon Raman processes are also possible, which can be derived when extending Eq. (2.5) to higher orders. The second order term leads to an induced polarization whose frequencies are $\omega_s=(\omega_i\pm\omega_A\pm\omega_B)$ with the frequencies ω_A and ω_B of the two phonons A and B. The Raman peaks with frequency $\omega_A+\omega_B$ and $\omega_A-\omega_B$ refer to the combination and difference mode, respectively. When $\vec{q}_A\pm\vec{q}_B\approx 0$, where $\vec{q}_A$ and $\vec{q}_B$ are the wave vectors of the two involved phonons, the wave vector conservation is satisfied.

2.2 Microscopic theory of Raman scattering

In this section, the microscopic model of Raman scattering is introduced. To describe the Raman scattering process by this approach, it seems reasonable to assume at the first glance that the interaction between photons in the visible spectral range and phonons could be sufficient to describe the scattering process. However, the interaction strength of this process is very weak and so far is only proposed theoretically [Hum72]. Hence, to describe the Raman scattering process, the model must include the electron-photon and electron-phonon interaction. Therefore it is necessary to describe the Hamiltonian of the crystal. This Hamiltonian can be simplified using the Born-Oppenheimer approximation, which relies on the fact that the electron mass in a crystal is much lighter compared to the ion mass. Consequently, the electrons move much faster and interact with quasi stationary ions. The approximated Hamiltonian can now be expressed as the sum of three terms:

$$\hat{\boldsymbol{H}} = \hat{\boldsymbol{H}}_{\boldsymbol{ion}}(\vec{R}_j) + \hat{\boldsymbol{H}}_{\boldsymbol{e}}(\vec{r}_i, \vec{R}_{j0}) + \hat{\boldsymbol{H}}_{\boldsymbol{e-ion}}(\vec{r}_i, \delta\vec{R}_j) \tag{2.11}$$

where $\hat{\boldsymbol{H}}_{\boldsymbol{ion}}(\vec{R}_j)$ is the Hamiltonian, describing the motion of ions under the influence of the ionic potential plus the time-averaged adiabatic electron potential. The Hamiltonian $\hat{\boldsymbol{H}}_{\boldsymbol{e}}(\vec{r}_i, \vec{R}_{j0})$ describes the energy of the electron within the ionic potential, when the ions are in their equilibrium position $\vec{R}_{j0}$ and $\hat{\boldsymbol{H}}_{\boldsymbol{e-ion}}(\vec{r}_i, \delta\vec{R}_j)$ the change of the electron energy when the ions are displaced by $\delta\vec{R}_j$ to this equilibrium position. Since motions of ions in a solid are vibrations, $\hat{\boldsymbol{H}}_{\boldsymbol{e-ion}}(\vec{r}_i, \delta\vec{R}_j)$ can be seen as the electron-phonon interaction.
A semiconductor sample usually contains more than 10^{23} electrons. This justifies the simplification of the electron Hamiltonian by the use of the mean-field approximation. Here, it is assumed that all electrons are influenced by an average potential $V(\vec{r})$, and the Hamiltonian can be written as:

$$\hat{\boldsymbol{H}}_{\boldsymbol{e}} = \frac{p^2}{2m} + V(\vec{r}) \tag{2.12}$$

As mentioned before, the electron-phonon interaction is the main contribution for the Raman scattering process. The adiabatic approximation allows to express $\hat{\boldsymbol{H}}_{\boldsymbol{e-ion}}(\vec{r}_i, \delta\vec{R}_j)$ as a Taylor series expansion of the electronic Hamiltonian

$\hat{\boldsymbol{H}}_{\boldsymbol{e}}$:

$$\hat{\boldsymbol{H}}_{\boldsymbol{e-ion}}(\vec{r}_i, \delta\vec{R}_j) = \sum_j \left(\frac{\partial \hat{\boldsymbol{H}}_{\boldsymbol{e}}}{\partial \vec{R}_j} \right) \Bigg|_{\vec{R}_{j0}} \cdot \vec{R}_j + ... \tag{2.13}$$

In most cases, the electronic Hamiltonian is not known and consequently approximations are needed to calculate the electron-phonon interaction. A discussion of these approximations is beyond the scope of this thesis and a more detailed description can be found in literature [YC10].
Furthermore, the electron-radiation interaction, described by the Hamiltonian $\hat{\boldsymbol{H}}_{\boldsymbol{eR}}$, must be considered for the microscopic theory of Raman scattering. Using the Coulomb gauge, i.e. scalar potential $\Phi = 0$ and $\nabla\vec{A} = 0$ applies for the vector potential $\vec{A}$, $\hat{\boldsymbol{H}}_{\boldsymbol{eR}}$ can be expressed as [Gas12]:

$$\hat{\boldsymbol{H}}_{\boldsymbol{eR}} = \frac{e}{mc}\vec{A}(\vec{r}) \cdot \vec{p} \tag{2.14}$$

The inelastic scattering of photons by phonons is a coherent three step process, involving an electron-hole pair and two intermediate states $|n\rangle$ and $|n'\rangle$. For example, this three-step process can occur in the following order:

- The creation of an electron-hole pair, by the excitation of the electron system from its initial state $|i\rangle$ into an intermediate state $|n\rangle$ by interacting with an incident photon with frequency ω_i via the electron-radiation interaction $\hat{\boldsymbol{H}}_{\boldsymbol{eR}}$.
- The electron-hole pair emits a phonon via the electron-phonon interaction Hamiltonian $\hat{\boldsymbol{H}}_{\boldsymbol{e-ion}}(\vec{r}_i, \delta\vec{R}_j)$. The electron system is then in the intermediate state $|n'\rangle$.
- Emission of a scattered photon with frequency ω_s by recombination of the electron-hole pair. The electron system is then in its final state $|f\rangle$.

This is one exemplary sequence of the total Raman scattering process. In principle all possible sequences of the individual steps may contribute to the inelastic scattering process. By permuting the order of the individual steps, all other possibilities are derived in which the scattering process can proceed. Feynman diagrams are a shown in Fig. 2.1, which are visualizations of the sequences. In Feynman diagrams, photons, phonons and electron-hole pairs are represented as lines (propagators) and the interactions between two excitations as intersections of the propagators. If the arrow drawn at the lines is pointing towards the intersection, the excitation is created, whereas when it is

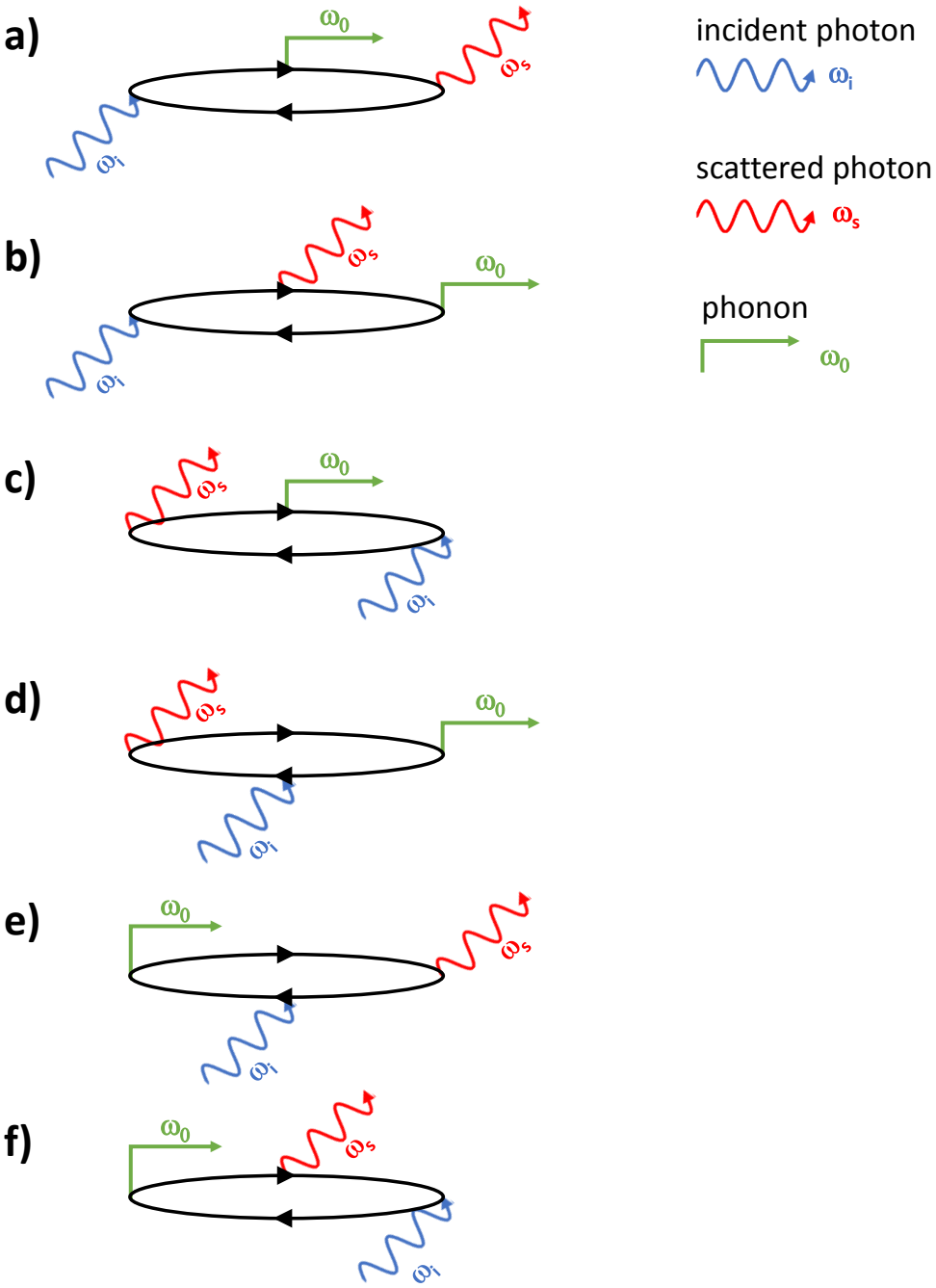

Figure 2.1: Feynman diagrams for the six scattering processes that may contribute to one phonon Stokes Raman scattering. Based on [YC10].

pointing away, the excitation is annihilated.
To determine the total probability of the scattering process, all possible permutations of the three step process must be included. For the sake of simplicity, the approach to obtain the scattering probability is explained only for one of the six contributions. The finding is then used to derive the scattering probabilities of the remaining process sequences, to determine the total probability of the scattering process. The excitation step can be expressed by the interaction between the photon and electron-hole pair as follows:

$$\sum_{n} \frac{\langle n|\hat{\boldsymbol{H}}_{\boldsymbol{eR}}(\omega_i)|i\rangle}{[\hbar\omega_i - (E_n - E_i)]} \tag{2.15}$$

where E_i and E_n are the energy values of the initial state $|i\rangle$ and the intermediate state $|n\rangle$, respectively. To include the subsequent second step, the equation is extended:

$$\sum_{n,n'} \frac{\langle n'|\hat{\boldsymbol{H}}_{\boldsymbol{e-ion}}(\omega_0)|n\rangle\langle n|\hat{\boldsymbol{H}}_{\boldsymbol{eR}}(\omega_i)|i\rangle}{[\hbar\omega_i - (E_n - E_i)] \cdot [\hbar\omega_i - \hbar\omega_0 - (E_{n'} - E_i)]} \tag{2.16}$$

with the frequency of the phonon ω_0 and the energy $E_{n'}$ of the second intermediate state $|n'\rangle$. It is important to note that the electronic states are unchanged after the scattering process. Therefore the final state $|f\rangle$ as well as the energy of the final state E_f is identical to the initial state $|i\rangle$ and its corresponding energy E_i. Consequently, the denominator of the last step term to become $(\hbar\omega_i - \hbar\omega_0 - \hbar\omega_s)$, which vanishes because of the energy conservation of the scattering process. As a result, the denominator is replaced by the delta function $\delta[\hbar\omega_i - \hbar\omega_0 - \hbar\omega_s]$, leading to the scattering probability of the first contribution of the Raman process:

$$\begin{aligned} P(\omega_s) =& \frac{2\pi}{\hbar} \left| \sum_{n,n'} \frac{\langle i|\hat{\boldsymbol{H}}_{\boldsymbol{eR}}(\omega_s)|n'\rangle\langle n'|\hat{\boldsymbol{H}}_{\boldsymbol{e-ion}}(\omega_0)|n\rangle\langle n|\hat{\boldsymbol{H}}_{\boldsymbol{eR}}(\omega_i)|i\rangle}{[\hbar\omega_i - (E_n - E_i)] \cdot [\hbar\omega_i - \hbar\omega_0 - (E_{n'} - E_i)]} \right|^2 \\ & \times \delta[\hbar\omega_i - \hbar\omega_0 - \hbar\omega_s] \end{aligned} \tag{2.17}$$

To get the total scattering probability, all prior steps for each of the six individual diagrams shown in Fig. 2.1 are repeated. The sum of the obtained individual scattering probabilities results in the total scattering probability of

the Raman process as follows:

$$
\begin{aligned}
P(\omega_s) =& \frac{2\pi}{\hbar}\Bigg| \sum_{n,n'} \frac{\langle i|\hat{\boldsymbol{H}}_{\boldsymbol{eR}}(\omega_i)|n\rangle\langle n|\hat{\boldsymbol{H}}_{\boldsymbol{e-ion}}(\omega_0)|n'\rangle\langle n'|\hat{\boldsymbol{H}}_{\boldsymbol{eR}}(\omega_s)|i\rangle}{[\hbar\omega_i - (E_n - E_i)]\cdot[\hbar\omega_i - \hbar\omega_0 - (E_{n'} - E_i)]} \\
&+ \frac{\langle i|\hat{\boldsymbol{H}}_{\boldsymbol{eR}}(\omega_i)|n\rangle\langle n|\hat{\boldsymbol{H}}_{\boldsymbol{eR}}(\omega_s)|n'\rangle\langle n'|\hat{\boldsymbol{H}}_{\boldsymbol{e-ion}}(\omega_0)|i\rangle}{[\hbar\omega_i - (E_n - E_i)]\cdot[\hbar\omega_i - \hbar\omega_s - (E_{n'} - E_i)]} \\
&+ \frac{\langle i|\hat{\boldsymbol{H}}_{\boldsymbol{eR}}(\omega_s)|n\rangle\langle n|\hat{\boldsymbol{H}}_{\boldsymbol{e-ion}}(\omega_0)|n'\rangle\langle n'|\hat{\boldsymbol{H}}_{\boldsymbol{eR}}(\omega_i)|i\rangle}{[-\hbar\omega_s - (E_n - E_i)]\cdot[-\hbar\omega_s - \hbar\omega_0 - (E_{n'} - E_i)]} \\
&+ \frac{\langle i|\hat{\boldsymbol{H}}_{\boldsymbol{eR}}(\omega_s)|n\rangle\langle n|\hat{\boldsymbol{H}}_{\boldsymbol{eR}}(\omega_i)|n'\rangle\langle n'|\hat{\boldsymbol{H}}_{\boldsymbol{e-ion}}(\omega_0)|i\rangle}{[-\hbar\omega_s - (E_n - E_i)]\cdot[-\hbar\omega_s + \hbar\omega_i - (E_{n'} - E_i)]} \\
&+ \frac{\langle i|\hat{\boldsymbol{H}}_{\boldsymbol{e-ion}}(\omega_0)|n\rangle\langle n|\hat{\boldsymbol{H}}_{\boldsymbol{eR}}(\omega_i)|n'\rangle\langle n'|\hat{\boldsymbol{H}}_{\boldsymbol{eR}}(\omega_s)|i\rangle}{[-\hbar\omega_0 - (E_n - E_i)]\cdot[-\hbar\omega_0 + \hbar\omega_i - (E_{n'} - E_i)]} \\
&+ \frac{\langle i|\hat{\boldsymbol{H}}_{\boldsymbol{e-ion}}(\omega_0)|n\rangle\langle n|\hat{\boldsymbol{H}}_{\boldsymbol{eR}}(\omega_s)|n'\rangle\langle n'|\hat{\boldsymbol{H}}_{\boldsymbol{eR}}(\omega_i)|i\rangle}{[-\hbar\omega_0 - (E_n - E_i)]\cdot[-\hbar\omega_0 - \hbar\omega_s - (E_{n'} - E_i)]}\Bigg|^2 \\
&\times \delta[\hbar\omega_i - \hbar\omega_0 - \hbar\omega_s]
\end{aligned}
\tag{2.18}
$$

Loudon et al. estimated the scattering probability to be in the range of $10^{-6} - 10^{-7}$ [sterad cm]$^{-1}$ [Lou63], in spite of the large number of parameters.

According to this equation, several intermediate states at specific energy levels are involved in the total Raman scattering process. When one of the denominators, tends to zero, the corresponding term diverges and a drastic increase of the scattering probability occurs. This is known as resonant Raman scattering, which is discussed in the next section.

2.3 Resonant Raman scattering

The scattering efficiency of the Raman process is in general relatively low, as seen in the previous section. Resonant Raman spectroscopy is a feasible technique to overcome the experimental obstacle of inefficiency of the Raman scattering process. Resonance conditions can be achieved, when the ingoing photon energy $\hbar\omega_i$ equals the energy $(E_n - E_i)$ or the scattered photon energy $\hbar\omega_s$ to the energy $(E'_n - E_i)$. In this cases, the corresponding denominator in Eq. 2.18 becomes zero and the scattering probability is drastically increased. One can find different approaches to fulfill these resonance conditions in experiments, for example, by varying the temperature, applying pressure to the

sample or modifying other experimental parameters, which influence the band gap energy of the semiconductor [AAC84]. The second, more straightforward technique, is the variation of the incident photon energy by the use of a tunable light source, to achieve a match of the incoming or outgoing photon energy with the energy difference $(E_n - E_i)$ or $(E'_n - E_i)$, respectively. This approach is used in this thesis.

Typically resonance conditions cannot be fulfilled for all possible scattering paths simultaneously. This can be seen by comparing the denominators in Eq. (2.18) of each individual scattering probability. Assuming that the first term in Eq. (2.18) is in resonance and the initial state is the ground state $|i\rangle$ with energy set to zero, Eq. (2.18) can be approximated to:

$$P(\omega_i) = \frac{2\pi}{\hbar}\left|\frac{\langle i|\hat{\boldsymbol{H}}_{\boldsymbol{eR}}(\omega_i)|n'\rangle\langle n'|\hat{\boldsymbol{H}}_{\boldsymbol{e-ion}}(\omega_0)|n\rangle\langle n|\hat{\boldsymbol{H}}_{\boldsymbol{eR}}(\omega_s)|i\rangle}{[\hbar\omega_i - E_{n'}]\cdot[\hbar\omega_s - E_n]} + C\right|^2 \tag{2.19}$$

where C is a constant, including the five other paths as well as the sum of all intermediate states other than $|n\rangle$. This simplification is justified under resonance conditions, i.e. for an incoming resonance $\hbar\omega_i$ equals $E_{n'}$ and for an outgoing resonance $\hbar\omega_s$ is identical to $E_{n'}$.

When a resonance condition is fulfilled, the scattering probability diverges according to Eq. (2.19). This unphysical outcome is avoided by including the finite lifetime τ_n and $\tau_{n'}$ of the intermediate states. This is considered by a modification of the energy terms in Eq. (2.19), including the damping constants Γ_n and $\Gamma_{n'}$, which are related to the lifetime of their corresponding states by $\Gamma_n = \hbar/\tau_n$ and $\Gamma_{n'} = \hbar/\tau_{n'}$. Thus Eq. (2.19) can be expressed as:

$$P(\omega_i) = \frac{2\pi}{\hbar}\left|\frac{\langle i|\hat{\boldsymbol{H}}_{\boldsymbol{eR}}(\omega_i)|n'\rangle\langle n'|\hat{\boldsymbol{H}}_{\boldsymbol{e-ion}}(\omega_0)|n\rangle\langle n|\hat{\boldsymbol{H}}_{\boldsymbol{eR}}(\omega_s)|i\rangle}{[\hbar\omega_i - (E_{n'} - i\Gamma_{n'})]\cdot[\hbar\omega_s - (E_n - i\Gamma_n)]} + C\right|^2 \tag{2.20}$$

If the lifetime of the phonon is comparable to the lifetime of the intermediate state, the damping constant Γ_0 of the phonon must also be included by replacing $\hbar\omega_s$ with $\hbar\omega_i - (\hbar\omega_0 - i\Gamma_0)$.

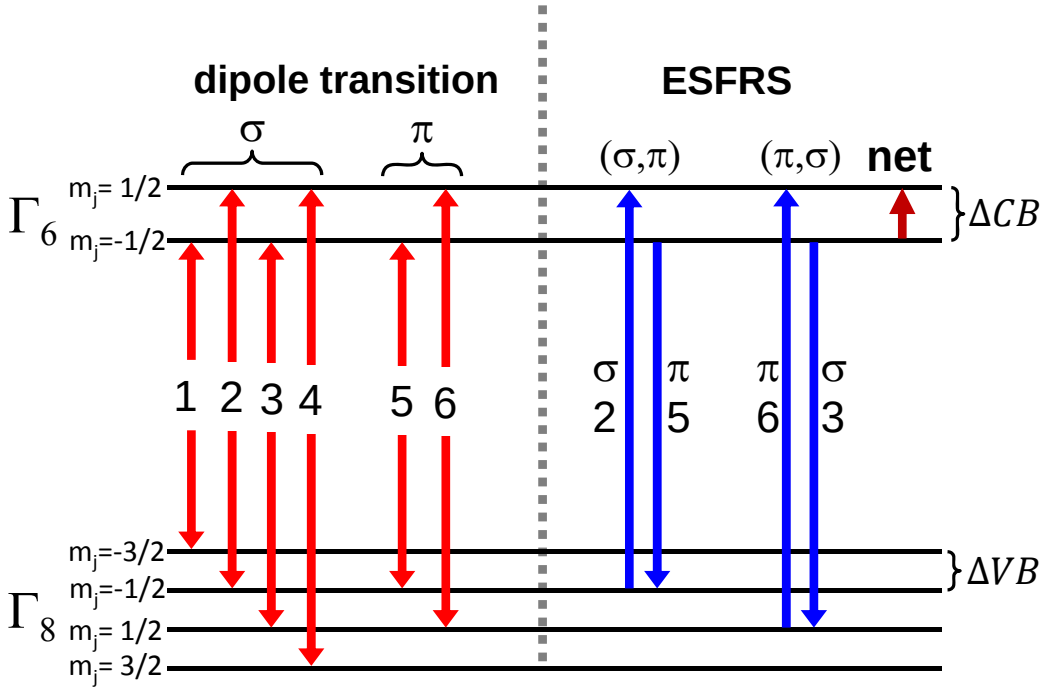

Figure 2.2: Schematic representation of the Γ_8 valence band and Γ_6 conduction band splitting for $B \neq 0$. The energy splitting of the valence band states with adjacent m_j values is denoted as ΔVB and for the conduction band as ΔCB. The dipole-allowed transitions in Voigt configuration are labeled as 1 to 6, represented by the red double arrows. The possible ESFRS processes which result in a net spin effect of the Γ_6 electron are shown on the right side of the diagram as a combination of two transitions (blue arrows). σ and π denote the light polarization directions.

2.4 Description of the electron spin flip Raman process

Electron spin flip Raman scattering (ESFRS) is the main experimental method used in this thesis. To understand this technique, it is first necessary to describe the dipole allowed transitions in a semiconductor under the influence of an external magnetic field. Two optical configurations are utilized for the majority of experimental studies: The Faraday and the Voigt configuration. In the Faraday configuration, the wave vector $\vec{k}$ of the light waves is parallel to the external B-field and the polarisation of the light is typically chosen to be either right σ^+ or left σ^- circular polarized. In Voigt configuration the wave vector $\vec{k}$ is perpendicular to the B-field and the linear polarization is either parallel (π) or perpendicular (σ) to the external B-field. In backscattering

geometry, used in the Raman experiments of this thesis, the electron spin flip can only be detected in Voigt configuration. Hence, in the following section the dipole allowed transitions in this configuration are described, which are visualized in Fig. 2.2. For $B \neq 0$ the Γ_8 VB and Γ_6 CB split into subbands, which are labeled according to their corresponding m_j quantum number. Optical transitions with a difference of $\Delta m_j = 0; \pm 1$ for the two involved states are dipole allowed. All possible transitions are shown in Fig. 2.2, where transitions no. 5 and 6 with $\Delta m_j = 0$ require an interaction with a π polarized photon and transitions no. 1 to 4 with $\Delta m_j \pm 1$ with a σ polarized photon.
The electron spin flip Raman scattering induces an increase (Stokes process) or decrease (anti-Stokes process) of m_j by one. Due to energy conservation of the Raman process, the relevant transitions originate from the same VB state. Hence, for the Stokes electron spin flip process, the following two paths are solely possible (also shown in Fig. 2.2):

- The incident photon is π polarized and excites a electron from the $m_j = 1/2$ VB state to the $m_j = 1/2$ CB state by creating an electron hole pair (transition no. 6). A second electron in the m_j = -1/2 CB state recombines with the hole by emitting a σ polarized photon (transition no. 3).

- The incident photon is σ polarized and excites a electron from the m_j = -1/2 VB state to the $m_j = 1/2$ CB state by creating an electron hole pair (transition no. 2). A second electron in the m_j = -1/2 CB state recombines with the hole by emitting a π polarized photon (transition no. 5).

In both cases, the CB electron spin is increased by one, which causes an excitation of the CB electron by the energy difference ΔCB. This splitting can experimentally be obtained by measuring the energy difference of the incident to the scattered photon.
The scattering probability of the ESFRS process reads as follows [HK04]:

$$P(\omega_i) \propto \left| \frac{\langle 0|\hat{\boldsymbol{H}}_{\boldsymbol{eR}}(\omega_i)|n\rangle\langle n|\hat{\boldsymbol{H}}_{\boldsymbol{eR}}(\omega_s)|f\rangle}{\hbar\omega_i - E_n} \right|^2 \tag{2.21}$$

where $|0\rangle$ is the ground state, $|n\rangle$ the intermediate state and $|f\rangle$ the final state. Note that the ESFRS process consists only of two steps, compared to

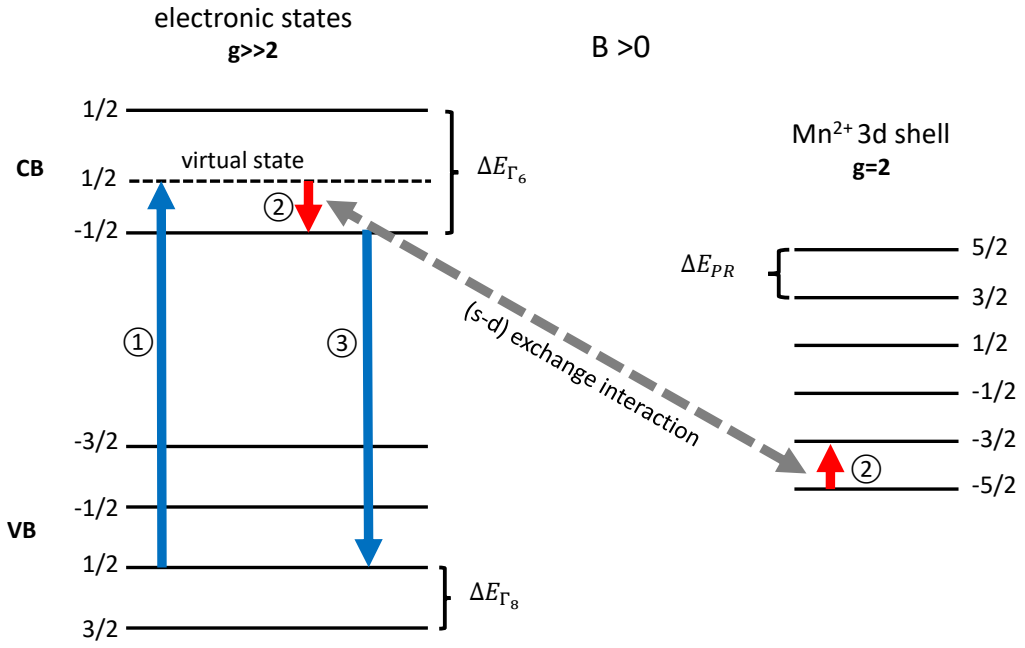

Figure 2.3: Scheme of the three step PR-transition at B>0 T, with an enlarged energy scale of the Mn-ion states in respect to the VB and CB energy splitting, because ΔE_{PR} is in the range of a few hundred μeV, compared to ΔE_{Γ_6} and ΔE_{Γ_8} which are in the meV range.

the previously mentioned LO phonon scattering process and more importantly the intermediate state is an eigenstate of the system. When the incoming resonance condition is fulfilled, the relaxation step is automatically in resonance. Consequently, the ESFRS process is a double resonance, yielding an extremely pronounced scattering efficiency enhancement. Therefore the ESFRS resonance is a powerful and sensitive tool to analyze the properties of the CB energy distribution in an external magnetic field.

2.5 Electron paramagnetic resonance of Mn^{2+}-ions

In a II-VI diluted magnetic semiconductor, manganese substitutes the group-II element. The electrons of the half filled 3d-shell of Mn^{2+} form according to Hund's rule a $^6S_{5/2}$-multiplet with J=5/2 in the ground state [Fur88]. In an external magnetic field B, this ground state splits into six equidistant spin

states, showing a linear Zeeman effect as follows:

$$\Delta E_{PR}(B) = m_s \cdot g_{Mn} \cdot \mu_B \cdot B \tag{2.22}$$

with the magnetic quantum number $m_s \in \{-\frac{5}{2}, -\frac{3}{2}, -\frac{1}{2}, \frac{1}{2}, \frac{3}{2}, \frac{5}{2}\}$, the g-factor of manganese g_{Mn} and the Bohr magneton μ_B. The $^6S_{5/2}$ ground state of Mn^{2+} has no orbital momentum, hence only pure spin magnetism with a g-factor of two for Mn^{2+} arises [DNS84]. The splitting of the $^6S_{5/2}$ states in an external field is visualized on the right side in Fig. 2.3. Raman scattering can be deployed to measure the energy splitting of the atomic states of the Mn ion, which is known as electron paramagnetic resonance (EPR).
A possible EPR process is shown in Fig. 2.3 and is described by a three step process [PPV+83]:

1. An electron is optically excited by a photon with frequency ω_i from a VB state with $m_j = +1/2$ into the CB state with $m_j = +1/2$.

2. A spin flip with $\Delta m_j = -1$ of the electron to the lower CB state, which simultaneously induces a flip of the Mn spin with $\Delta m_j = +1$ via the (s-d) exchange interaction between the CB electron and the manganese electron.

3. The recombination of the CB electron with the VB hole, by emission of a photon with frequency ω_s.

It should be noted that the energy splitting of the Mn states is in most cases much lower than the splitting of the CB and VB states. Therefore, in comparison to the resonant ESFRS process, no double resonance is possible at simple reachable experimental conditions for the EPR.
Besides a single Mn spin flip, multiple spin flips were observed. The theoretical explanation of the process is beyond the scope of this thesis and can be found in literature [SSD+95] [KM97].

Chapter 3

Experimental

3.1 Optical setup

The results presented in this theses were performed at a low-temperature magneto-Raman setup. This setup consists of three main sections: The tunable light source, the magneto-optical cryostat and the spectrometer. A sketch of this setup is shown in Fig. 3.1.

Tunable light source: A dye laser (Coherent: CR-599) is deployed as a tunable light source, which is optically pumped by an Argon ion laser (Coherent: Innova-400). The UV lines at 358 nm and 368 nm of the argon ion laser with a maximum achievable output power of 6 W are used to optically excite the dye Stilbene 3. Stilbene 3 shows a broad photoluminescence between 2.72 eV and 2.95 eV, corresponding to a wavelength range from 420 nm to 455 nm. A birefringent filter inside the cavity of the dye laser allows a tuning of the emitted coherent light in the prior mentioned energy range, with an accuracy better than 1 meV. The tuning of the excitation energy is required to study resonance effects of $Zn_{1-x}Mn_xSe$ with a band gap of about 2.8 eV. The maximum outgoing dye laser power of 100 mW is reached at a pump power of 3.5 W. A further increase of the pump power locally heats the dye solvent above the boiling point, which generates bubbles within the dye jet, causing an instability of the output laser power.

Beside the strong laser line, the dye laser emits a broad background. This background hampers measurements of weak Raman signals and therefore a

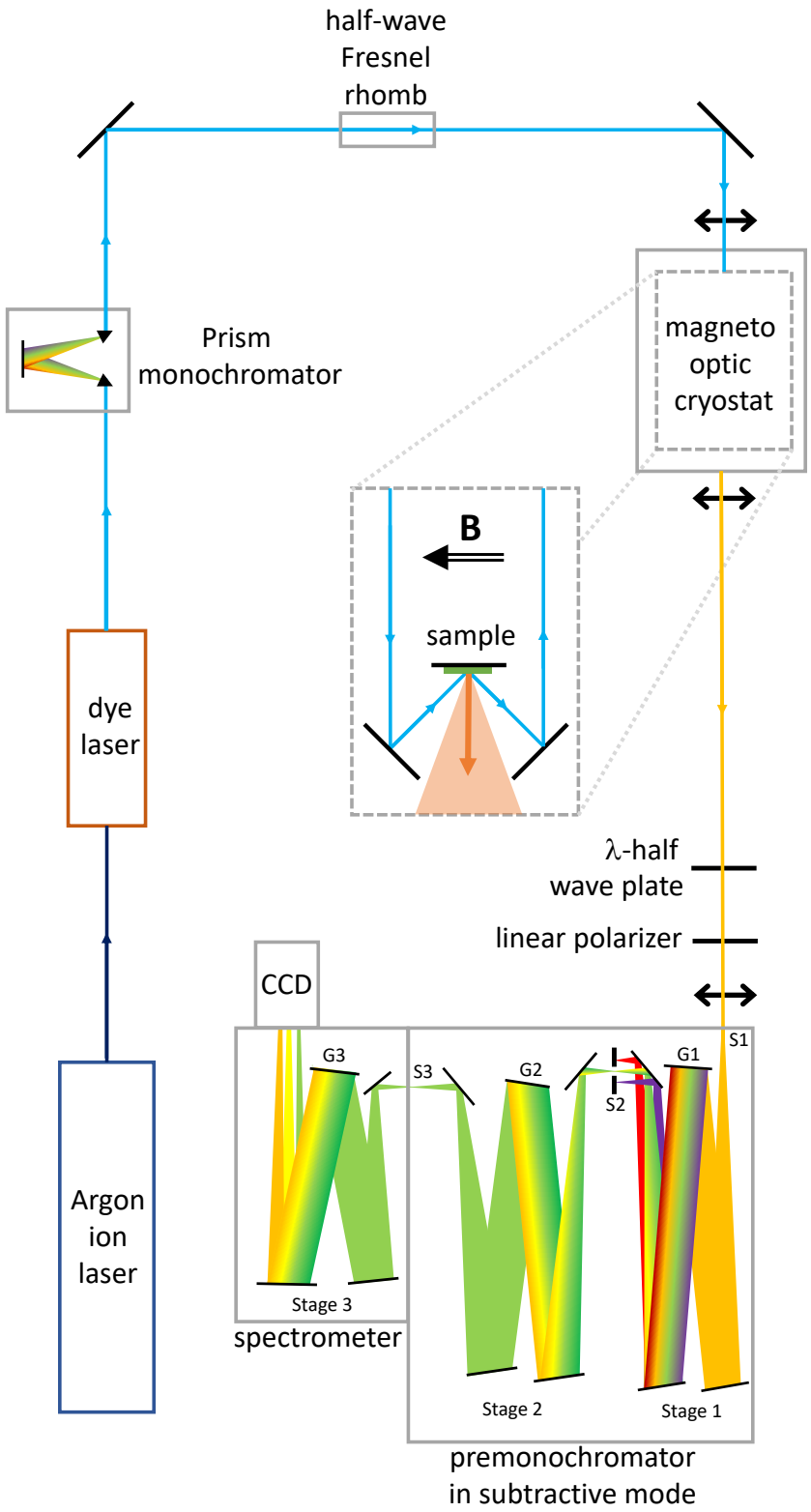

Figure 3.1: Scheme of the experimental setup for the resonant Raman scattering spectroscopy studies. S1 is the entrance slit of the premonochromator stage, S2 the intermediate slit, and S3 the entrance slit of the spectrometer stage. The gratings are labeled as G1, G2 and G3.

prism monochromator is placed in the optical path behind the dye laser. This acts as a tunable laser line filter, which drastically reduces the intensity of the emitted background.

Magneto-optical cryostat: All measurements were performed at temperatures below $T = 2\,\mathrm{K}$ and B-fields up to $7\,\mathrm{T}$. For this purpose, a bath cryostat (Oxford Instruments) equipped with a split-coil superconducting magnet is used. The samples are immersed in liquid helium and by reducing the vapor pressure to less than $10\,\mathrm{mbar}$, the helium bath temperature is lowered to $T \approx 1.5\,\mathrm{K}$. This is below the λ-point of liquid helium at $2.18\,\mathrm{K}$, at which the transition to the superfluid phase occurs. The extremely high thermal conductivity of superfluid helium is advantageous to avoid unwanted gaseous helium bubbles, which would occur in the normal fluid phase of helium, caused by the optical excitation and subsequent heating of the sample. The laser beam would be scattered by these bubbles, increasing the optical background level. The samples are analyzed in the backscattering geometry, i.e. the wave vector of the incident and scattered photon are anti parallel to each other and perpendicular to the sample surface. To realize this geometry, two small mirrors are mounted inside the sample chamber. In this geometry, the beam of the elastically scattered light is not entering the entrance slit of the spectrometer. This drastically suppresses the intensity of the Rayleigh scattered photons.
The magneto-optic bath cryostat is capable of applying an external B-field up to $7\,\mathrm{T}$, which is orientated parallel to the sample surface and perpendicular to the wave vector of the incident and scattered photon. This arrangement of the B-field to the wave vector is known as Voigt geometry. The linear polarization of the incident light can be set by a half-wave Fresnel rhomb, which is positioned in the beam path between the dye laser and the cryostat, to enable either parallel (π) or perpendicular (σ) polarization with respect to the B-field. The polarization of the scattered light is analyzed in π or σ configuration. This is achieved by a combination of an achromatic λ-half wave plate and a linear polarizer. It is important to control the incident and scattered photon polarization for Raman experiments, because Raman scattering is a coherent process.

Spectrometer: The scattered light is analyzed by a Dilor XY triple monochromator. This kind of monochromator is often deployed for Raman experiments, especially when low energy excitations, like paramagnetic resonance Raman scattering, are investigated. The assembly of a triple monochromator consists of a double monochromator (premonochromator stage) and an additional single monochromator stage. The double monochromator can either be set in additive mode, where the dispersion of the both gratings adds up to the total dispersion of the monochromator. This mode is useful, when a high spectral resolution is needed. The monochromator stage can also be operated in subtractive mode. In this mode, the dispersions of the two gratings cancel each other, effectively resulting in a zero dispersion of the premonochromator stage. By placing a small slit (S2) in the focal plane between the two stages (stage 1 and 2), a wavelength selective, variable filtering of the scattered light is achieved. For all experiments presented in this thesis, the monochromator was set to the subtractive mode, because a tunable light source was used and Raman signals of low energy excitations were detected. With a focal length of 50 cm of the spectrometer and 1800 grooves per mm of the gratings, a resolution of $0.8\,\mathrm{cm}^{-1}$ per pixel is achieved in the wavelength range between 420 and 460 nm.
For detection of the scattered photons, a Peltier-cooled CCD (ANDOR iDus series) is used, cooled to $-80°\mathrm{C}$ to reduce the thermal noise. The combination of the low thermal noise and the high quantum efficiency of up to 95% enables the detection of extremely weak signals. The sensor array consists of 1024×256 pixels, with a size of $26\,\mu\mathrm{m} \times 26\,\mu\mathrm{m}$ per pixel.

3.2 (Zn,Mn)Se samples

The $Zn_{1-x}Mn_xSe$:Cl samples were grown by the research group of Dr. Michael Hetterich at the Karlsruhe Institute of Technology (KIT) by molecular beam epitaxy (MBE) with Mn content $x \in \{0.01;\ 0.05;\ 0.07\}$ on semi-insulating (100) GaAs substrates. The evaporation of $ZnCl_2$ provided chlorine as n-type dopant. The layer structures consist of an undoped ZnSe buffer, followed by the n-type $Zn_{1-x}Mn_xSe$:Cl layer. These $Zn_{1-x}Mn_xSe$:Cl layers have a thickness of about $1\,\mu$m [ADKH06]. The n-doping is between nominally undoped and $N_{Cl} = 1.3\times10^{18}\mathrm{cm}^{-3}$, which is above the critical carrier concentration N_c of the metal-insulator transition of about $7 \times 10^{17}\mathrm{cm}^{-3}$ [JWN+14]. X-ray diffraction

Table 3.1: Parameters of the $Zn_{1-x}Mn_xSe$:Cl samples in this study: Mn content x, dopant concentration N_{Cl}, and ZnSe layer thickness

sample	Mn x	N_{Cl} (cm^{-3})	thickness (μm)
BD-95	0.07	$<10^{16}$	0.70
BD-229	0.05	2.0×10^{17}	0.93
BD-230	0.05	4.2×10^{17}	1.04
BD-274	0.05	1.3×10^{18}	0.90
B0-175	0.01	4.3×10^{17}	1.05

(XRD) analysis was used to verify the Mn content. The relevant parameters of the studied samples are listed in Table 3.1.

Part II

Results and Discussion

Chapter 4

Resonant Electron Spin Flip Raman Spectroscopy

In this chapter the results of the electron spin flip Raman spectroscopy measurements at B-fields ranging from $B = 1\mathrm{T}$ *up to* $B = 7\mathrm{T}$ *in* (π, σ) *Voigt configuration are presented. At excitation energies between* $E_{exc} = 2.800\,\mathrm{eV}$ *and* $2.835\,\mathrm{eV}$ *a distinct increase of the scattering efficiency of the electron spin flip Raman scattering (ESFRS) process occurs. This resonance profile consists of two partially overlapping peaks, which can be assigned to the donor bound exciton* (D^0, X) *and free exciton* (X^0) *assisted EFSRS process. By increasing the B-field from* $1\,\mathrm{T}$ *up to* $7\,\mathrm{T}$*, a clear broadening of the* (D^0, X) *assisted process is observed. To explain this observation a model is proposed, based on the random distribution of the magnetic Mn-ions on the Zn-sublattice and the finite size of the* (D^0, X) *and* (X^0) *excitons. The model allows a quantitative analysis of the local Mn distribution in the range of the* (D^0, X) *and moreover the estimation of the* (D^0, X) *and* (X^0) *radii. For Mn content ranging from* $x = 0.01$ *to* $x = 0.07$ *and n-doping concentrations up to* $n = 1.3{\cdot}10^{18}\ \mathrm{cm}^{-3}$*, the determined radii range from* $1.96\,\mathrm{nm}$ *up to* $5.9\,\mathrm{nm}$ *for the* (D^0, X) *and from* $2.09\,\mathrm{nm}$ *up to* $11.5\,\mathrm{nm}$ *for the* (X^0)*.*

4.1 Magneto photoluminescence and magneto Raman spectroscopy on n-doped (Zn,Mn)Se:Cl

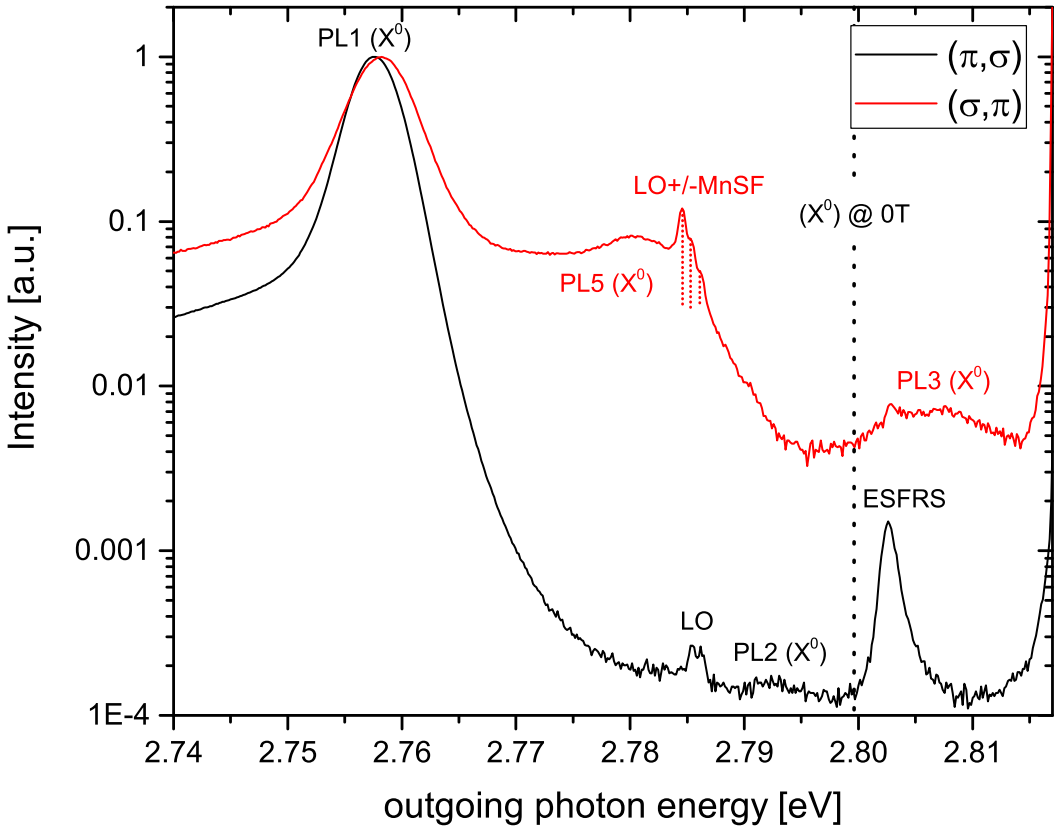

Figure 4.1: Two spectra with Raman and PL signatures of sample BD-230, at $B = 7\,\mathrm{T}$ and a bath temperature of $T = 1.7\,\mathrm{K}$, in the Voigt configurations (σ, π) (red line) and (π, σ) (black line), with an excitation energy of $E_{in} = 2.8174\,\mathrm{eV}$ and $E_{in} = 2.8177\,\mathrm{eV}$, respectively. The photoluminescence peaks are assigned according to Fig. 2.2. The dotted line marks the position of the PL at $B = 0\,\mathrm{T}$. Three Raman signals occur: The LO phonon at E = 2.7855 eV, the combination process of an LO and a spin flip of the Mn ion (LO ± MnSF) and only in (π, σ)-configuration the ESFRS at $E = 2.8026\,\mathrm{eV}$.

In Fig. 4.1 two exemplary spectra with Raman and PL signatures of sample BD-230, at an external magnetic field of $B = 7\,\mathrm{T}$ and a bath temperature of $T = 1.7\,\mathrm{K}$, in (σ, π) and (π, σ) Voigt configuration, and an incident photon energy of $E_{in} = 2.8174\,\mathrm{eV}$ and $E_{in} = 2.8177\,\mathrm{eV}$, respectively are shown. The small difference of the incident photon energy of 0.3 meV has no significant influence on the two spectra and can therefore be neglected for the analysis of

the polarization dependence.

Both spectra are normalized to their most intense feature, which is the peak at $E = 2.758\,\text{eV}$. The absolute count rate per second of the peak in (π, σ)-configuration is about 100 times larger than in (σ, π)-configuration and clearly indicates, that this peak is σ polarized. Hence this peak can be identified as the photoluminescence, corresponding to transition no. 1 ($|$CB,-1/2$\rangle$ to $|$VB,-3/2$\rangle$) (see Fig. 2.2) of the free exciton (X^0) due to its polarization and its lowest absolute energy at the external B-field of 7 T. In principle, the peak could also originate from the donor bound exciton (D^0, X), especially for an n-doped sample. However, it was shown by Heiman et al., that at magnetic fields above 1.5 T, the (D^0, X) becomes energetically instable and hence, the (X^0) is the main source for the observable photoluminescence [HBK$^+$86].

A small mismatch of 0.7 meV of this PL peak for the two polarization configurations is detected. This is most likely caused by heating of the Mn spin system possibly due to a difference of the excitation density for these two experimental conditions [KYK$^+$01]. The heating effect is discussed in section 4.3 in more detail.

The broad feature at $E = 2.781\,\text{eV}$ only occurs in (σ, π)-configuration, suggesting that this peak is π polarized. This reduces the number of possible transitions to the transition no. 5 ($|$CB, -1/2$\rangle$ to $|$VB, -1/2$\rangle$) and no. 6 ($|$CB, 1/2$\rangle$ to $|$VB, 1/2$\rangle$). Because the observed peak shifts to lower energies with increasing B-field, it is identified as transition no. 5. This peak originates from the (X^0) because the (D^0, X) is thermally unstable at $B = 7\,\text{T}$ as explained before. Therefore the peak is labeled as PL5 (X^0).

Additionally, in (σ, π)-configuration a feature at $E = 2.8068\,\text{eV}$ can be assigned to transition no. 3, because it only slightly shifts to higher energies with increasing B-field. A weak PL feature at $E = 2.7924\,\text{eV}$ is only visible in (π,σ)-configuration. Due to the slight redshift with increasing B-field and its σ polarization, this PL is referred to transition no. 2 of the (X^0).

It should be noted that due to the symmetry of the B-field induced energy level splitting, PL no. 2 and no. 3 both are shifted by the same absolute value of 7.2 meV with opposite sign when applying a B-field of 7 T.

Furthermore, there are two weak, narrow Raman features. The first is detectable at $E = 2.7855\,\text{eV}$ in both polarization configurations. Calculating the energy difference between the signal and the incident photon energy yields $\Delta E = 32\,\text{meV}$ equal to a Raman-Shift of $\Delta\tilde{\nu} = 255\,\text{cm}^{-1}$, therefore identified

as the LO phonon peak of ZnSe [Ric68]. A closer inspection of this feature in (σ,π)-configuration reveals that it consists of three individual peaks. The origin of this "fork like" triple peak structure is a combination process of the LO phonon and additional Mn spin flip Stokes and anti-Stokes processes, hence the structure is labeled as LO ± MnSF. A detailed study of this LO-assisted Mn spin flip is presented in chapter 6. The second narrow feature only arises in the (π,σ)-configuration at $E = 2.8026\,\mathrm{eV}$, which corresponds to $\tilde{\nu} = 121\,\mathrm{cm}^{-1}$ for the incident photon energy of $E_{in} = 2.8177\,\mathrm{eV}$. It will be shown in this chapter that this peak originates from the electron spin flip between the conduction band states |CB, +1/2⟩ and |CB, -1/2⟩.
Topic of this chapter is the study of this electron spin flip Raman scattering (ESFRS). The resonant enhancement of the ESFRS process is used as an experimental tool, to get further insight in the physics the ESFRS process and the behavior of the CB and VB states in an external magnetic field. Moreover, the influence of the carrier concentration on the ESFRS resonance behavior is studied. The resulting observations are analyzed to determine the radius of the free and donor bound excitons.

4.1.1 B-field dependence of the photoluminescence and Raman features

To get further insight in the B-field dependent behavior of the previously mentioned PL and Raman peaks, the development of these features at B-fields ranging from $B = 0\,\mathrm{T}$ to $7\,\mathrm{T}$ is investigated. Spectra of sample BD-230 in (σ,π) Voigt configuration are shown in Fig. 4.2. The most intense peak at $E = 2.787\,\mathrm{eV}$ and $B = 0\,\mathrm{T}$ shifts to lower absolute energies, when an external magnetic field is applied. At $B = 1.25\,\mathrm{T}$ a second feature with 6 meV higher energy than the main feature occurs. This energy difference stays constant for B-fields between 1.25 T and 2 T, when both peaks are distinguishable. Above $B = 2\,\mathrm{T}$, the formerly weaker peak becomes dominant, whereas the other peak vanishes. This observation can be explained by the thermal instability of the bound exciton with increasing B-field [HBK$^+$86]. At low magnetic fields, the exciton binds to a donor, forming a (D^0, X). For $B \neq 0\,\mathrm{T}$ the $S = 1/2$ state increases and the $S = -1/2$ state lowers its energy with increasing B-field. Due to the symmetry of this energy level splitting,

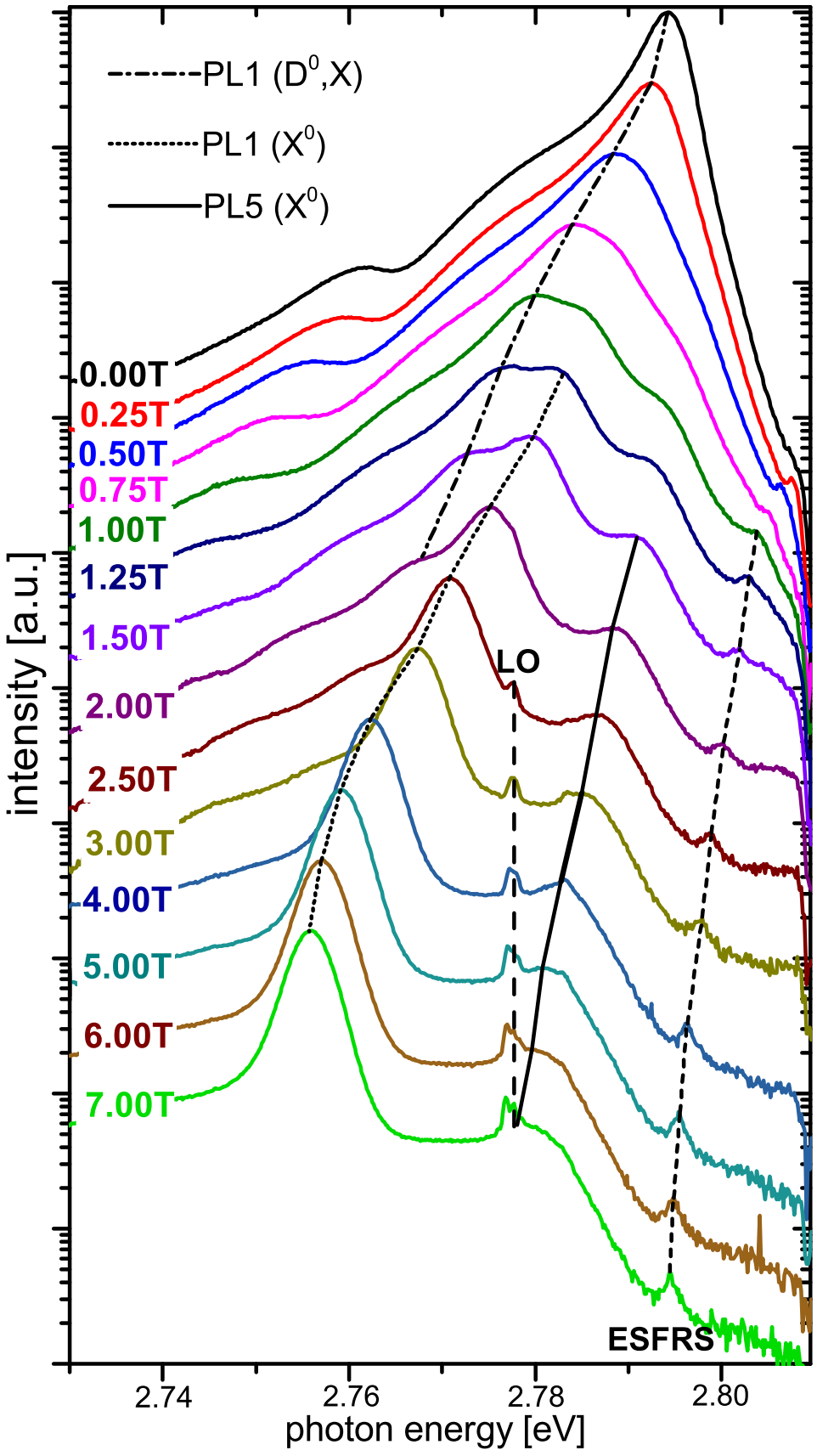

Figure 4.2: Waterfall plot of the spectra of sample BD-230 with B-fields from 0T to 7T in (σ,π)-configuration with incident photon energy E_{in} = 2.8095eV. The full, dashed and dotted lines are guides to the eye for the PL features and the LO and ESFRS Raman peaks.

the combined energy of the two electrons is B-field independent. At a critical magnetic field $B_{crit} \approx 1.5\,\mathrm{T}$, the energy splitting of these two electron states exceeds the binding energy of the (D^0, X) and hence, the formation of the donor bound exciton becomes energetically disadvantageous. Thus above B_{crit}, the free exciton is the thermally stable state and the origin of the PL. This model explains the observation of the B-field dependence of the two PL peaks, which is typical for the transition from the donor bound exciton (D^0, X) to the free exciton (X^0). Heiman et al. performed a detailed study of this transition for (Cd,Mn)Te and (Cd,Mn)Se [HBK+86].
Another PL feature is the high-energy shoulder of the main PL peak, which becomes visible at $B = 1\,\mathrm{T}$. This additional signal starts to separate at B-fields above 1.5 T. Due to its position relative to the main PL peak and its less pronounced shift with increasing B-field, it is assigned to transition no. 5 (see Fig. 2.2). As explained for PL no. 1, this peak should also originate from the (D^0, X) for low B-fields and above B_{crit} mainly from the (X^0), but this transition cannot be resolved for PL no. 5.
Two weaker signals are also detectable, which were identified as Raman signals in a previous section. The first Raman peak is B-field independent and has a Raman-shift of $\tilde{\nu} = 256\,\mathrm{cm}^{-1}$. Thus, this feature corresponds to the LO phonon of ZnSe. Above $B = 4\,\mathrm{T}$ this Raman feature broadens and further separates into three distinguishable peaks at even higher B-fields. As mentioned before, these LO satellites are the sum process of a LO phonon and the Stokes and anti-Stokes Mn spin flip. A careful analysis of the B-field dependent splitting reveals a linear trend with increasing B-field, which yields a g-factor of two, equal to the g-factor of Mn in ZnSe. A detailed study of these features is presented in chapter 6.

The second Raman peak arises at B-field $> 1\,\mathrm{T}$ and shifts to a lower absolute energy with increasing B-field, i.e. an increasing Raman shift. In Fig. 4.3, the peak position is plotted versus the external magnetic field. The shift of this peak can be described by a Brillouin function (Eq. 1.14) and a fit of the data points is also presented in Fig. 4.3. The fit yields a saturation of $\tilde{\nu} = 124\,\mathrm{cm}^{-1}$ for $B \to \infty$. Due to this observation and the polarization dependence (see Fig. 4.1), the peak is identified as the electron spin flip from the CB state with $m_j = +1/2$ to the CB state with $m_j = -1/2$ (see Fig. 2.2). According to the theory of the ESFRS process, it is also allowed in (π, σ)-configuration (see chapter 2). Typically, at a specific excitation energy the ESFRS can only

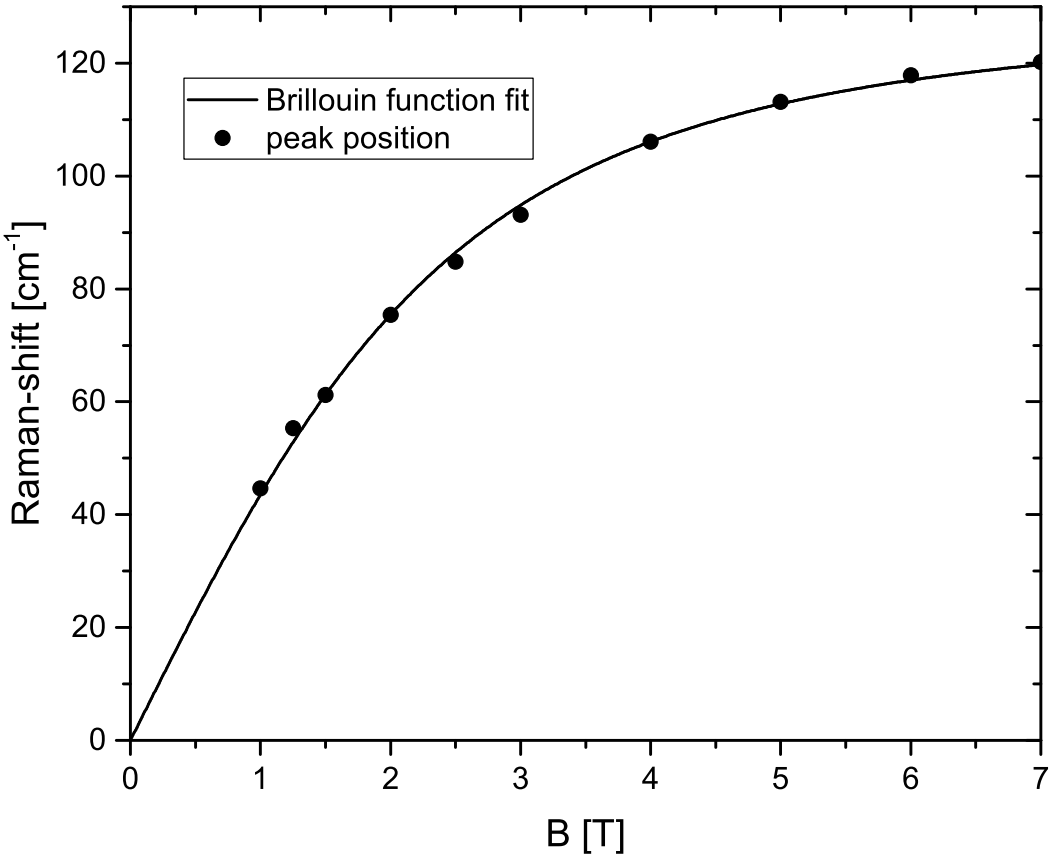

Figure 4.3: ESFRS peak position of spectra of Fig. 4.1 (black dots) versus external magnetic field. Black line: Brillouin function fit of data points, with $\tilde{\nu}_{sat} = 124\,\mathrm{cm}^{-1}$ for $B \to \infty$.

be detected in either one of the two configurations, due to its distinct resonance enhancement, which differs for the two configurations. For the presented spectra, the ESFRS peak appears close to PL no. 5 (ΔE up to 10 meV), which causes an enhancement of the ESFRS process in (σ, π)-configuration (see chapter 2).

4.1.2 Influence of the n-doping concentration on the magneto photoluminescence

PL spectroscopy is not the main experimental method used in this thesis, therefore only a brief overview about the influence of the n-doping concentration on the PL features is presented. The spectra of the intrinsic sample BD-95 and an n-doped sample BD-230 with a doping concentration of n = $4.2{\cdot}10^{17}\mathrm{cm}^{-3}$

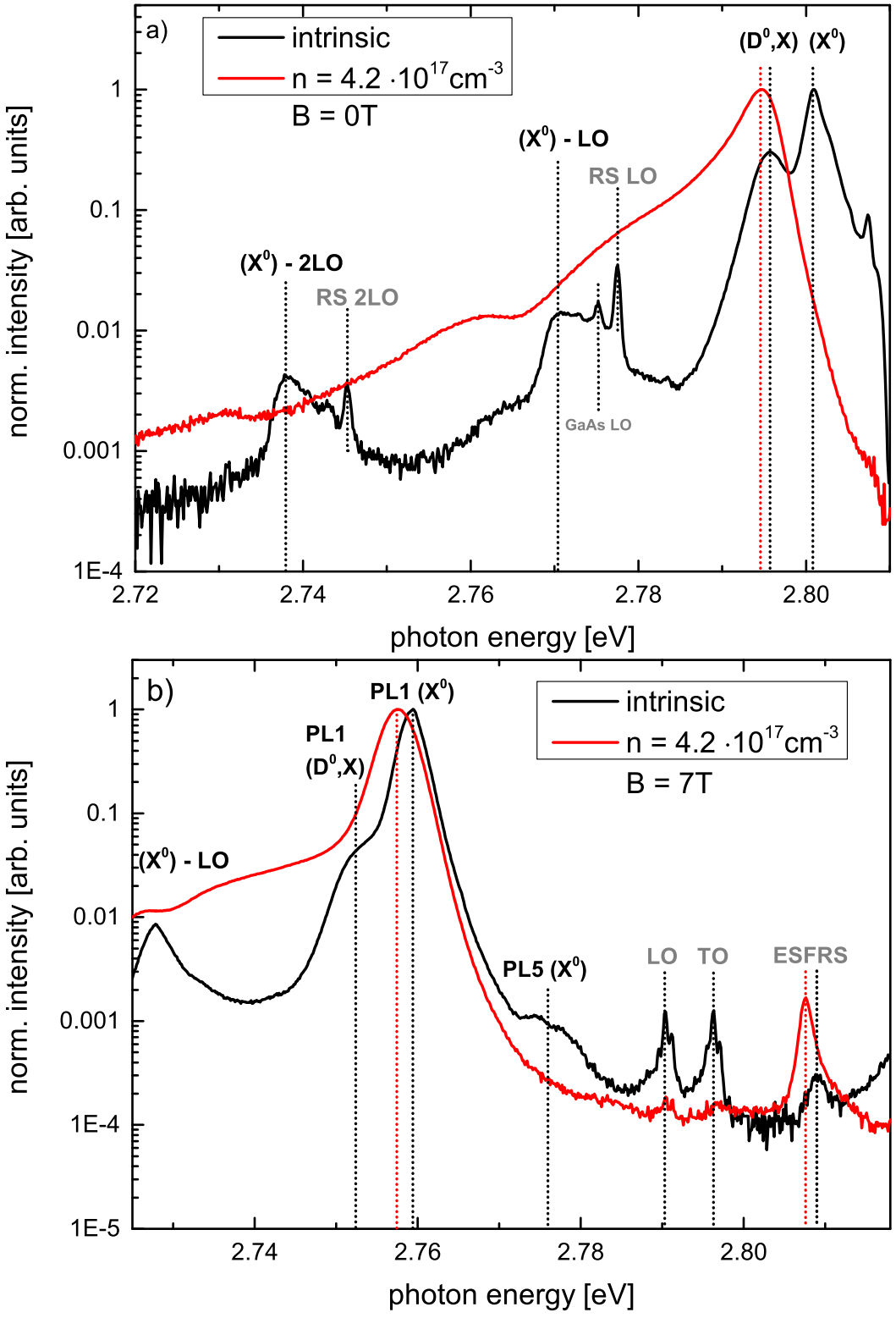

Figure 4.4: Spectra in (π, σ)-configuration of sample BD-95 ($x = 0.07$; intrinsic) black curve and BD-230 ($x = 0.05$, n = $4.2{\cdot}10^{17}\mathrm{cm}^{-3}$) red curve. a) at $B = 0\,\mathrm{T}$ and b) $B = 7\,\mathrm{T}$.

at $B = 0\,\mathrm{T}$ and $B = 7\,\mathrm{T}$ are discussed in this section. The Mn incorporation of the samples is $x = 0.07$ and $x = 0.05$, respectively.

In Fig. 4.4 a) the spectra of both samples at $B = 0\,\mathrm{T}$, a helium bath temperature of $T = 1.5\,\mathrm{K}$ and an excitation energy of $E_{exc} = 2.809\,\mathrm{eV}$ are plotted. The most noticeable difference of the two spectra are the overall significantly narrower features of the undoped sample. This allows to resolve two separate intense peaks at $E = 2.801\,\mathrm{eV}$ and $E = 2.796\,\mathrm{eV}$ at $B = 0\,\mathrm{T}$, whereas for the doped sample a broad peak at $E = 2.795\,\mathrm{eV}$ is detected. The energy difference of the two peaks of the undoped sample amounts to $\Delta E = 5\,\mathrm{meV}$, which is equal to the binding energy of the (D^0, X) with resprect to (X^0) [DSP+88]. Therefore, these two peaks are identified as the PL of the (D^0, X) and (X^0). Moreover, the strongest peak of the doped sample coincides with the (D^0, X) of the undoped sample. This is plausible, because the n-doping increases the chance of the formation of a (D^0, X), which enhances the ratio of the (D^0, X) to (X^0) PL intensities.

Furthermore, for the intrinsic sample LO phonon replicas of (X^0) appear as (X^0)-LO and (X^0)-2LO. The (X^0)-LO phonon coupling strength benefits from the rather strong polarity of the II-VI bonds. Due to the broad characteristic of the PL features of the doped sample, these replicas are not individually resolvable and instead manifest itself as a subtle decaying flank of the main PL feature.

Beside these PL features, three Raman peaks are detected: the sharp peak at $E = 2.7775\,\mathrm{eV}$, which is Stokes-shifted by $31.5\,\mathrm{meV}$ with respect to the laser line at $2.809\,\mathrm{eV}$, belongs to the LO phonon of ZnSe, and its second order peak 2LO appears at $2.7455\,\mathrm{eV}$ (equal to a Stokes-shift of $\tilde{\nu} = 63.5\,\mathrm{meV}$). The weaker narrow feature at $E = 2.7752\,\mathrm{eV}$ equals to a Raman-shift of $33.8\,\mathrm{meV}$ and is assigned to the LO of the GaAs substrate. These Raman peaks are not visible in the spectrum of the doped sample, due to the broad and intense PL background, which overlaps the weaker expected Raman features.

Spectra of the two samples at $B = 7\,\mathrm{T}$ in (π,σ)-configuration and an excitation energy of $E_{exc} = 2.823\,\mathrm{eV}$ are shown in Fig. 4.4 b). The PL peaks are assigned according to the previously given explanation for the B-field dependent development of the individual PL peaks. Comparing the two spectra at $B = 7\,\mathrm{T}$ reveals that the undoped sample still shows sharper PL features, which enables the assignment of the (D^0, X) transition no. 1 even at a high magnetic field. The (X^0) PL1 peak is located at $E = 2.7594\,\mathrm{eV}$ and $E = 2.7576\,\mathrm{eV}$ for the

undoped and doped sample, respectively. This is a small mismatch of 1.8 meV and the even smaller energy difference of about 1 meV of the ESFRS peak between the two samples, is most likely caused by the different Mn concentration of the two samples, because the saturation value of the energy levels is directly proportional to the effective Mn concentration. Besides the ESFRS, additional Raman peaks are also detectable for the undoped sample. These are the LO and TO phonon of ZnSe, located at a Raman shift of $\tilde{\nu} = 256\,\mathrm{cm}^{-1}$ and $\tilde{\nu} = 205\,\mathrm{cm}^{-1}$, respectively. Furthermore, satellite features, which are caused by additional Stokes and anti-Stokes Mn spin flip are located close to the LO and TO peak.
The excitation energy was adjusted from $E_{exc} = 2.809\,\mathrm{eV}$ at $B = 0\,\mathrm{T}$ to $E_{exc} = 2.823\,\mathrm{eV}$ at $B = 7\,\mathrm{T}$, to fulfill the resonance condition in (π,σ) Voigt configuration of the ESFRS process. Without this adjustment, the ESFRS peak would be much weaker at $B = 7\,\mathrm{T}$. In the following section, this influence of the excitation energy on the ESFRS signal intensity for all samples and magnetic fields ranging from $B = 1\,\mathrm{T}$ up to $B = 7\,\mathrm{T}$ is studied in detail.

4.2 Resonant ESFRS spectroscopy

As explained in chapter 2 the ESFRS process induces a net spin transfer from the photon to the electron system and therefore, can be measured either in (π,σ) or (σ,π) Voigt configuration. For both configurations, a resonant enhancement can be achieved by adjusting the excitation energy, so that it matches either transition no. 6 or 2 for the (π,σ) or (σ,π) Voigt configuration, respectively (see Fig. 2.2). Thus in principle both configurations are equally applicable to study the the ESFRS resonance profile. In (π,σ)-configuration and resonant excitation, the scattered photon energy equals transition no. 3; in (σ,π)-configuration this energy is equal to transition no. 5. These two transitions are separated by 1/3 of the total VB splitting, which is up to 25 meV at $B = 7\,\mathrm{T}$ for the studied samples. Moreover, the peak of PL3 is noticeable further separated from the strong PL1 than PL5, which can for example be seen in Fig. 4.1. Considering that the ESFRS peak is several orders of magnitude weaker than the PL peaks, it is crucial for an accurate determination of the ESFRS peak intensity to achieve a PL background intensity as low as possible. Thus (π,σ) is the preferred polarization configuration to study the ESFRS

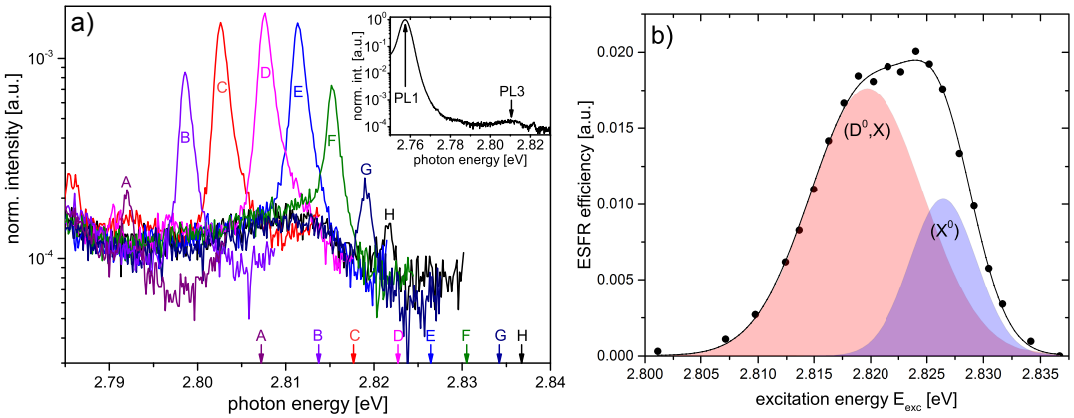

Figure 4.5: a) Series of spectra of sample BD-230 in (π, σ)-configuration at $B = 7\,\mathrm{T}$, recorded with different excitation energies E_{exc}. The arrows, denoted with the letters A to H, mark the E_{exc} values, the corresponding ESFRS peaks are denoted along the same scheme. The inset shows a wider spectral range, which includes PL1 and PL3, which induces the ESFRS resonance. b) The corresponding ESFRS efficiency profile. Full line: Fit curve, consisting of two Gaussians, which are colored in red ((D^0, X)-contribution) and blue ((X^0)-contribution).

resonance and all following presented results were acquired in this Voigt configuration.

In Fig. 4.5 a) a series of spectra of sample BD-230 ($x = 0.05$, n = $4.2{\cdot}10^{17}\mathrm{cm}^{-3}$) for varying excitation energies E_{exc}, $B = 7\,\mathrm{T}$ and $T = 1.7\,\mathrm{K}$ is plotted. The ESFRS peak is detectable for the whole range of excitation energies, at a constant Raman-shift of $\tilde{\nu} = 121\,\mathrm{cm}^{-1}$ with respect to the excitation energy E_{exc}. The E_{exc} values are indicated by the vertical arrows on the abscissa, labeled with the indices A to H. All spectra are normalized to their corresponding intensity of PL1, to minimize experimental errors, for example occurring due to fluctuations of the laser power, misalignment of the beam path or other effects. Obviously, the ESFRS peak strongly varies its intensity depending on the excitation energy (note the logarithmic intensity scale) and a maximum occurs when the ESFRS peak optimally overlaps with the broad PL background, corresponding to PL3. This is the expected behavior of the resonant enhancement of the ESFRS process in (π,σ)-configuration. The inset covers a larger energy range to verify the separation of 57 meV between PL1 and PL3 and thus, the PL1 background should not hamper the analysis of the ESFRS efficiency.

For a quantitative analysis of the ESFRS resonance enhancement, all ESFRS

peaks are individually fitted by a Gaussian curve. The determined areas of the Gaussians are considered as the relevant measure to describe the ESFRS scattering efficiency. These resulting scattering efficiencies of the measurements shown in Fig. 4.5 a) are represented as full circles versus the excitation energy in Fig. 4.5 b). It is striking that the ESFRS scattering efficiency shows a strong excitation dependent enhancement with a maximum at $E_{exc} = 2.824\,\mathrm{eV}$. For this excitation energy, the scattering efficiency is amplified by a factor of 22, compared to the weakest detected ESFRS intensity.
The ESFRS resonance profile consists of two partially overlapping structures. Each contribution can be fitted by a Gaussian curve. These fit results are also shown in Fig. 4.5 b). These two peaks are separated by about $\Delta E = 6\,\mathrm{meV}$, which is close to the binding energy of the (D^0, X) [DSP+88]. Hirsch et al. performed ESFRS and PLE studies on $Cd_{1-x}Mn_xTe$ and proved that due to the extremely fast ESFRS process, the intermediate state of the ESFRS process has not to be thermodynamically stable [HMW93]. This enables the ESFRS process via the (D^0, X) even for magnetic fields above the critical B-field of 1.5 T, even when the (D^0, X) becomes instable. Thus, it is reasonable to conclude that the intermediate state of the ESFRS process can be either (D^0, X) or (X^0) excitation state, explaining the double peak structure of the spectral profile of the ESFRS efficiency.

4.2.1 B-field dependence of the ESFRS resonance profile

For a more detailed analysis of the ESFRS resonance, the influence of the external magnetic field is investigated. Selected ESFRS efficiency profiles for B-fields between 1 T and 7 T are plotted in Fig. 4.6. At all applied B-fields the resonance profile has a double peak structure. The separation between both peak maxima is between 5 meV and 7.5 meV and does not show an obvious B-field dependence. This observation strengthens the assertion that the two contributions of the resonance profile arise from the (D^0, X) or (X^0) intermediate step, because the binding energy of the (D^0, X) is about 5 meV and B-field independent [DSP+88]. Furthermore, with increasing external magnetic field, the ESFRS resonance profile shifts to higher excitation energies. This is explained by the B-field dependent shift of transition no. 6, which corresponds

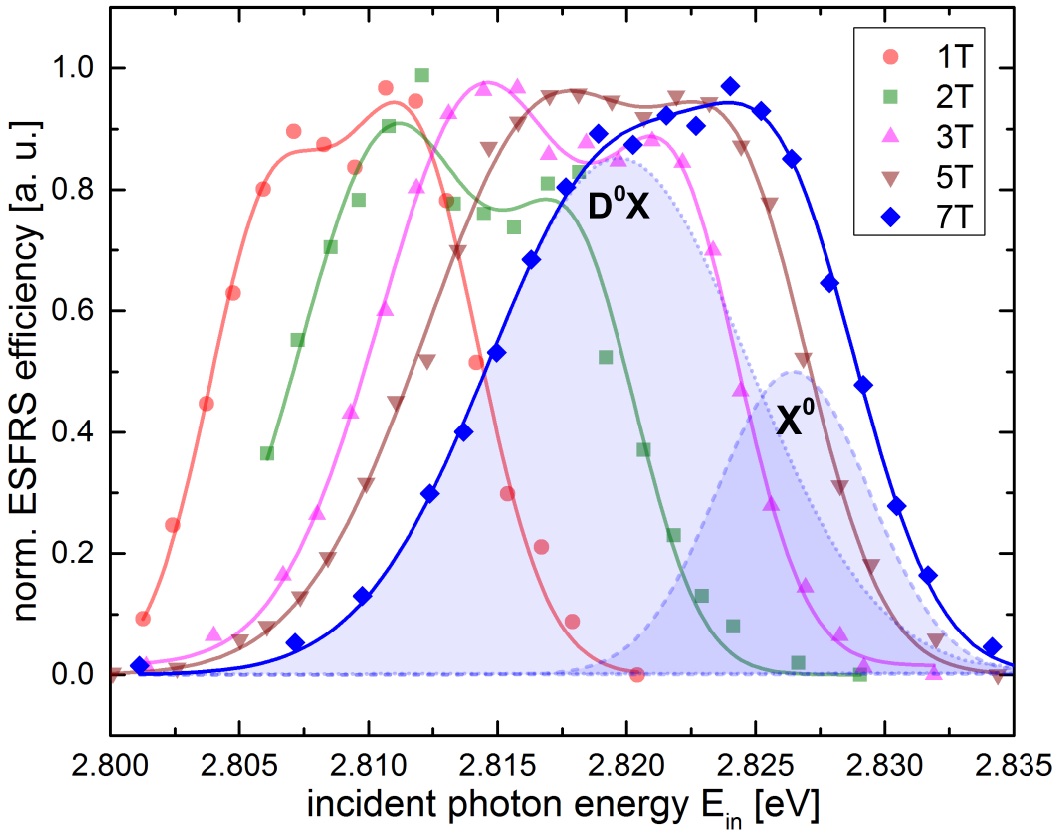

Figure 4.6: ESFRS efficiency profile of sample BD-230 for different B-fields up to 7 T. Full lines: Fit curves with two Gaussians ((D^0, X)-contribution and (X^0)-contribution), dashed and dotted line: separate contributions for $B = 7$ T.

to the incoming ESFRS resonance in (π,σ)-configuration.

The fit of the ESFRS resonance profile yields the widths and the energy positions of the (D^0, X) and (X^0) resonance contributions. The resonance maximum positions and the corresponding FWHM of the resonance profiles are plotted versus the external B-field in Fig. 4.7 a) and b), respectively. Here, the shift of the maximum position becomes striking, ranging from $E_{in,res} = 2.806$ eV at $B = 1$ T to $E_{in,res} = 2.820$ eV at $B = 7$ T for the (D^0, X) and $E_{in,res} = 2.812$ eV at $B = 1$ T to $E_{in,res} = 2.826$ eV at $B = 7$ T for the (X^0). Moreover, the resonance maximum shifts behave according to the Brillouin function, due to the trend of the underlying resonance transition no. 6 in an external B-field.

The ESFRS resonance widths of the (D^0, X) and (X^0) contribution, which are plotted in Fig. 4.7 b), show two distinct trends with increasing B-field. The resonance width of the (X^0) contribution fluctuates between 4.5 meV and 7.4 meV and only a slight increase of the width with increasing B-field is observed.

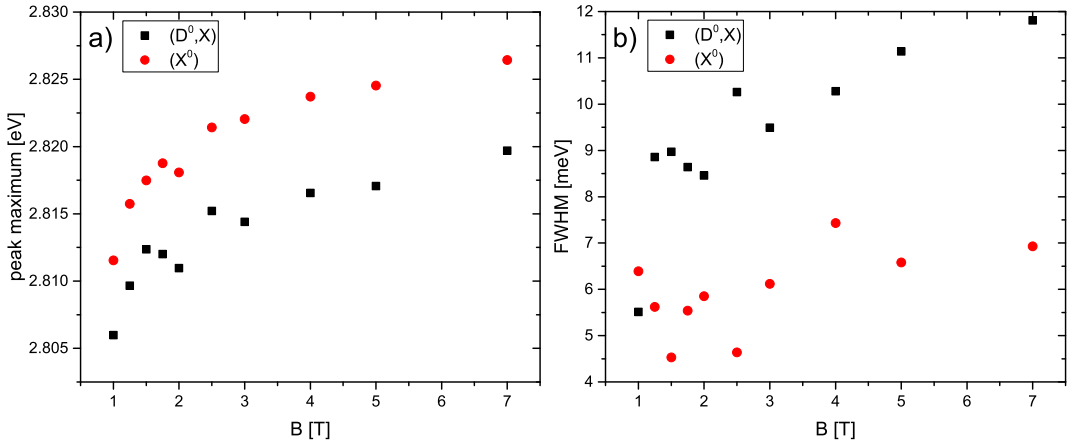

Figure 4.7: a) Excitation energy positions of the (D^0, X) and (X^0) resonance contribution at which the maximum ESFRS enhancement is achieved and in b) the corresponding FWHM of these contributions.

In contrast, the (D^0, X) assisted resonance width increases from 5.5 meV at $B = 1.0$ T to 11.8 meV at $B = 7.0$ T, which equals to more than a doubling of the FWHM. Moreover, the FWHM of the (D^0, X) contribution seems to show a "Brillouin like" behavior. In the next section, a model is introduced to explain these observations and, moreover, giving access to the (D^0, X) and (X^0) radii.

4.2.2 Impact of local fluctuations of the Mn-ion concentration on the dopant electron distribution

Due to the finite size of the excitons (D^0, X) and (X^0), each of them encompasses a distinct number N_{Mn} of Mn-ions in its expansion volume. For a Mn concentration of $x = 0.05$ and an exciton radius of a few nm, N_{Mn} can be calculated to be about 50. Assuming a random distribution of the Mn-ions on the cation sublattice, N_{Mn} will vary statistically for each individual exciton. Thus, it is useful to introduce a local Mn concentration x_{loc} to include the effect of spatial fluctuations of the Mn concentration. Considering the x_{loc} values for an ensemble of excitons, these are normally distributed centered at the chemical concentration x_0 and with a FWHM Γ_x. The justification for this assumption is verified by Monte Carlo simulations (see appendix A).
Due to (s-d) and (p-d) exchange interactions, the Mn concentration determines the splitting of the VB and CB levels in an external B-field, described

by Eqs. (1.28) and (1.29). Consequently the local fluctuations of the Mn-ion concentration directly affect the energy distribution of the energy levels, which also applies for the energy distribution of excitons. Furthermore, each exciton has its individual resonance energy of the ESFRS process, depending on x_{loc}. Consequently, it is plausible that the x_{loc} distribution affects the width of the ESFRS resonance Γ_{res}. Therefore the results of the measurements of the ESFRS resonance can be used to determine the x_{loc} distribution.
For a quantitative analysis, the concentrations $x^+ = x_0 + \Gamma_x/2$ and $x^- = x_0 - \Gamma_x/2$ are defined. Then, using Eq. (1.29), the B-field induced broadening of the ESFRS resonance can be described as follows:

$$\begin{aligned}\Gamma_{res}(B,T) = \Gamma_0 + \frac{1}{2}N_0\alpha \cdot \frac{5}{2}\Bigg(& x_{eff}(x^+)B_{5/2}\left[\frac{5g_{\mathrm{Mn}}\mu_{\mathrm{B}}B}{2k_{\mathrm{B}}(T+T_{AF}(x^+))}\right] \\ & -x_{eff}(x^-)B_{5/2}\left[\frac{5g_{\mathrm{Mn}}\mu_{\mathrm{B}}B}{2k_{\mathrm{B}}(T+T_{AF}(x^-))}\right]\Bigg)\end{aligned} \tag{4.1}$$

with Γ_0 as the intrinsic FWHM of the ESFRS scattering process due to the finite lifetime of the intermediate levels in the scattering process, i.e., without taking into account the random distribution of the Mn ions. Assuming a narrow distribution, the approximation $T_{AF}(x^+) = T_{AF}(x^-) = T_{AF}(x_0)$ is justified, which enables the substitution in Eq. (4.1) and the following simplification:

$$\begin{aligned}\Gamma_{res}(B,T) = \Gamma_0 + \frac{1}{2}N_0\alpha \cdot [x_{eff}(x^+) - x_{eff}(x^-)] \\ \cdot\frac{5}{2}\cdot B_{5/2}\left[\frac{5g_{\mathrm{Mn}}\mu_{\mathrm{B}}B}{2k_{\mathrm{B}}(T+T_{AF}(x_0))}\right].\end{aligned} \tag{4.2}$$

Here, it can be seen that the broadening of the ESFRS resonance has a Brillouin-like dependence with increasing B-field.
The resonance excitation energy $E_{in,res}$, for which the ESFRS efficiency maximum is achieved, refers to PL transition no. 6 with the highest probability of x_{loc}, which is in this situation equal to x_0. Thus the B-field dependence for the $E_{in,res}$ can be described as:

$$\begin{aligned}E_{in,res}(B,T) = E_0 + \frac{1}{2}(N_0\alpha - 1/3N_0\beta)\cdot x_{eff}(x_0) \\ \cdot\frac{5}{2}B_{5/2}\left[\frac{5g_{\mathrm{Mn}}\mu_{\mathrm{B}}B}{2k_{\mathrm{B}}(T+T_{AF}(x_0))}\right]\end{aligned} \tag{4.3}$$

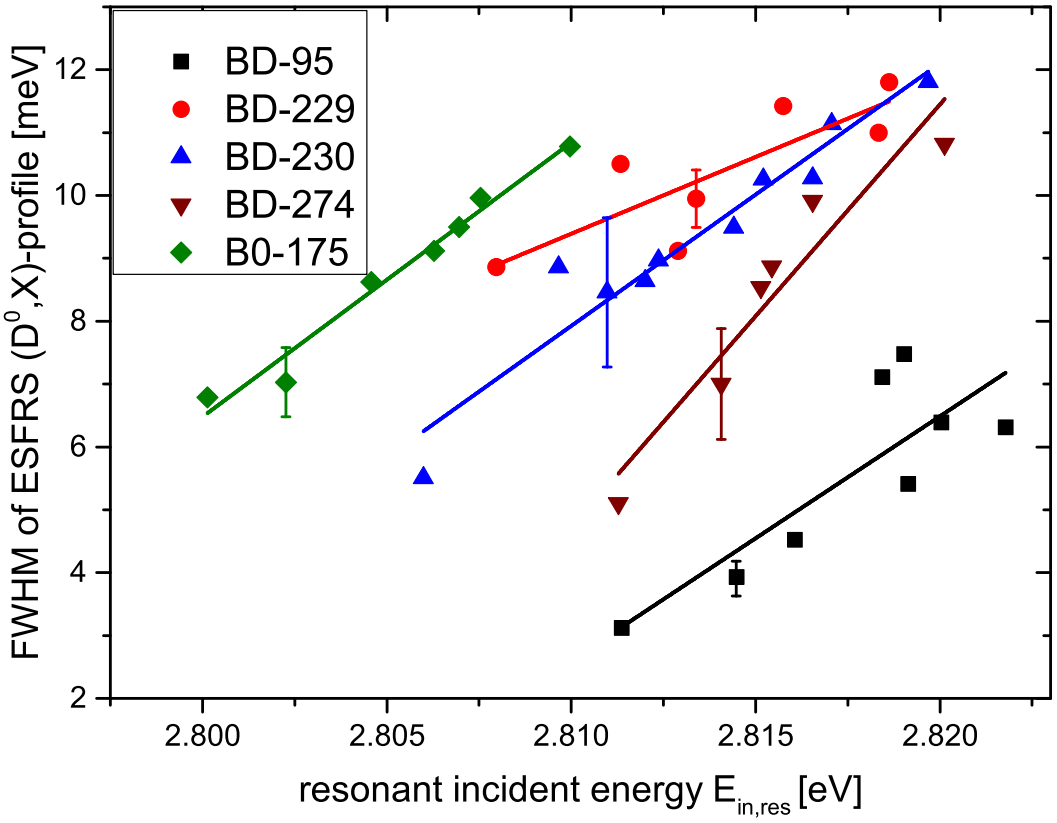

Figure 4.8: FWHM of the (D^0, X) contribution to the ESFRS resonance profile vs. the resonant excitation energy $E_{in,res}$ for all investigated samples. For each sample, the leftmost data point corresponds to the lowest B-field, the rightmost to $B = 7\,\mathrm{T}$. A typical error bar is shown exemplarily for each sample. The full lines are linear fits of the data points.

When substituting Eq. (4.3) into Eq. (4.2), Γ_{res} is expressed by a linear function:

$$\Gamma_{res}(E_{in,res}(B,T)) = \Gamma_0 + m \cdot [E_{in,res}(B,T) - E_0], \tag{4.4}$$

with

$$m = \frac{x_{eff}(x^+) - x_{eff}(x^-)}{x_{eff}(x_0)} \cdot \frac{N_0\alpha}{N_0\alpha - \frac{1}{3}N_0\beta}. \tag{4.5}$$

Here, the prefactor m is related to the maximum of the distribution x_0 and the width of the distribution Γ_x.

In Fig. 4.8, the FWHM values Γ_{res} of the Gaussian fits of the (D^0, X)-contribution to the ESFRS resonance profiles of each investigated sample are

plotted versus the resonant incident energy $E_{in,res}$. Each sample gives rise to a series of data points, the leftmost belonging to the lowest and the rightmost to the highest B-field, with values ranging from 1 T to 7 T. The FWHM values for the lowest B-fields are 3 meV for the intrinsic sample and 5 meV to 8.9 meV for the doped ones. The n-doping can induce a reduced lifetime of the (D^0, X), which enhances Γ_0 and consequently increases B-field-independently the value of Γ_{res}. This effect of Γ_0 on Γ_{res} is most pronounced at low B-fields and can explain the variation of Γ_{res} for the set of samples with different n-doping concentrations. For $B = 7$ T, the FWHM values range between 7 meV and 12 meV. For all samples, the expected linear increase of the FWHM with increasing $E_{in,res}$ according to Eq. (4.4) is observed. The resulting prefactors m are between 0.244 and 0.674 and listed in table 4.1. The positive values of the prefactors confirm the inhomogeneous broadening of the dopant electron level splitting. This is caused by the statistical distribution of Mn ions, which is reflected in the electron energy distribution via the (s-d) exchange interaction.

For the (X^0) contribution, the FWHM versus the incident photon energy $E_{in,res}$ is plotted in Fig. 4.9. In comparison to the (D^0, X)-contribution, the FWHM values are tendentially lower, ranging from 2.2 meV to 4.4 meV for the undoped sample and 3.2 meV to 8.2 meV for the doped ones. We assign this behavior to the unbound nature of the (X^0), thus it spans over a larger area and captures a higher number of Mn ions. Therefore, the impact of local fluctuations of the Mn concentration on the individual (X^0) should be reduced, which consequently harmonizes the (X^0) energy levels, resulting in a narrower distribution of x_{loc}, i.e. a less pronounced B-induced enhancement of the resonance profile width of the (X^0)-induced ESFRS process. This also explains, why a less pronounced linear trend of the FWHM of the (X^0) ESFRS resonance versus the resonant incident energy $E_{in,res}$ for all samples is observed. Nevertheless the data sets are fitted by linear curves and thee different resulting behaviors occur.

For the three samples with $x_0 = 0.05$ and n-doping concentrations below the metal-insulator transition of $n_{crit} = 7 \cdot 10^{17} cm^{-3}$ [JWN$^+$14, NJW$^+$13] (samples: BD-95, BD-229, BD-230), the FWHM increases slightly with the resonant incident energy, giving m-values between $m = 0.026$ to $m = 0.082$. Sample BD-274, which has an n-doping concentration of $n = 1.3 \cdot 10^{18} cm^{-3}$ clearly shows a broadening of the (X^0) assisted ESFRS resonance, comparable

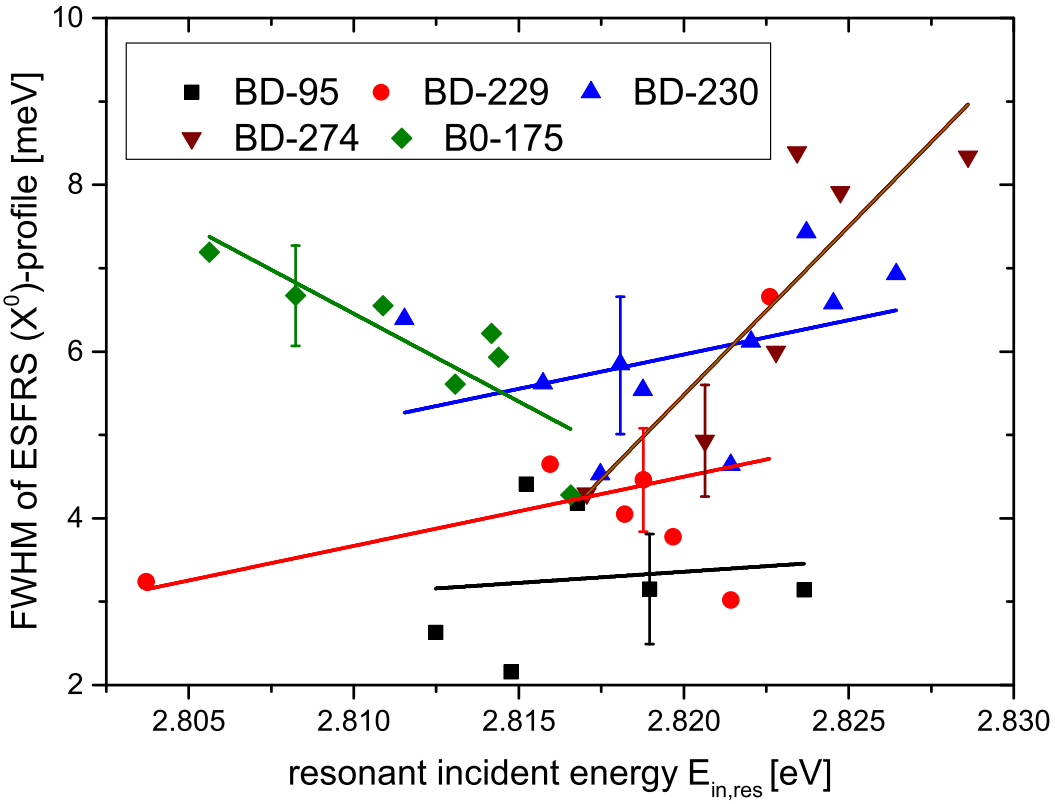

Figure 4.9: FWHM of the (X^0) contribution to the ESFRS resonance profile vs the resonant incident photon energy $E_{in,res}$ for all investigated samples. For each sample, the leftmost data point corresponds to lowest B-field, the rightmost to $B = 7\,\mathrm{T}$. A typical error bar is shown exemplarily for each sample. The full lines are linear fits of the data points.

with the observation for the (D^0, X) ESFRS resonance. The slope m is equal to 0.404, which is up to 15 times larger than the values of the samples with n-doping concentrations below the metal-insulator transition. The FWHM of the sample BD-95 with $x_0 = 0.01$ decreases with increasing $E_{in,res}$, i.e. increasing B-field. This cannot be explained by the introduced model, because the influence of the local fluctuation of the Mn concentration on the ESFRS resonance should never decrease the FWHM of the ESFRS resonance with increasing B-field. It should be noted that due to the lower Mn concentration of $x_0 = 0.01$, the absolute splitting of the energy levels is also reduced. Thus, there is a noticeable PL background even when the ESFRS process is in resonance, even at the maximum applied magnetic field of 7 T. This can affect the accuracy of the ESFRS scattering efficiency determination and hence increases the uncertainty of the measured resonance profile. As an result, the uncertainty of the

(X^0) ESFRS resonance FWHM is between 7% and 18% for this sample. Consequently, this could falsely appear as a narrowing of the (X^0) assisted resonance.

4.2.3 Determination of the radii of the excitons (D^0, X) and (X^0) by ESFRS resonance widening

Beside the confirmation of the B-field induced broadening of the (D^0, X) and (X^0) levels, the analysis of the B-induced inhomogeneous broadening of the ESFRS resonance curve can also be applied as a novel tool for the approximation of the (D^0, X) and (X^0) radii, because these determine the spatial scale of this probe. This procedure relies on the statistics of the Mn ions incorporation. Each cation site can either be occupied by a Mn^{2+} or a Zn^{2+} ion. For a Mn concentration x_0, the respective occupation probabilities are $p = x_0$ and $q = (1 - x_0)$. The random positioning of the Mn ions on the cation sublattice yields a binomial distribution, with the mentioned statistical parameters p and q. Considering this random distribution of Mn ions and a large set of (D^0, X) or (X^0) excitons, which act as the intermediate state of the ESFRS process, each (D^0, X) and (X^0) encompasses a random quantity N of Mn ions. Therefore, the half-width Γ_x of the corresponding bionomial distribution is $\Gamma_x = 2\sqrt{2ln(2)}\sqrt{x_0(1-x_0)/N}$; for $x_0 = 0.05$ one obtains $\Gamma_{0.05} = 0.513/\sqrt{N}$. Eq. (4.5) gives a correlation between the experimentally determined slope m, obtained by the ESFRS resonance broadening and the distribution of the local Mn concentration. Furthermore, the equation $x_0 = (x^+ + x^-)/2$ allows the calculation of x^+ and x^- and consequently also of the width of the Mn distribution Γ_x. Inversely, the knowledge of Γ_x enables the determination of the number N of Mn ions, which are encompassed by the (D^0, X) or (X^0):

$$N = 8 \cdot ln(2) \frac{x_0(1-x_0)}{\Gamma_x^2} \tag{4.6}$$

Finally, the radius of the (D^0, X) and (X^0) can be determined by considering the presence of four cations per cubic unit cell of the fcc crystal as follows:

$$r = \sqrt[3]{\frac{3 \cdot NV}{16 \cdot \pi}} \tag{4.7}$$

Table 4.1: Evaluation of the (D^0, X) and (X^0) radii of the $Zn_{1-x}Mn_xSe$:Cl samples: Mn contents x_0, doping levels N_{Cl}, slope m of the B-induced ESRFS resonance broadening (from Figs. 4.8 and 4.9), FWHM Γ_x of the Mn distribution, and resulting (D^0, X) and (X^0) radii.

			(D^0, X)			(X^0)		
sample	Mn x_0	N_{Cl} (cm^{-3})	slope m	FWHM Γ_x	radius (nm)	slope m	FWHM Γ_x	radius (nm)
BD-95	0.07	$<10^{16}$	0.388	0.023	1.96	0.027	0.002	11.5
BD-229	0.05	$2.0{\cdot}10^{17}$	0.244	0.010	3.18	0.083	0.003	7.23
BD-230	0.05	$4.2{\cdot}10^{17}$	0.418	0.019	2.04	0.082	0.003	7.00
BD-274	0.05	$1.3{\cdot}10^{18}$	0.674	0.028	1.55	0.404	0.018	2.09
B0-175	0.01	$4.3{\cdot}10^{17}$	0.436	0.002	5.90	-0.211	-	-

with the cubic unit cell volume V, which is $V_{ZnSe} = (0.567\text{nm})^3$ for ZnSe [MRS]. The resulting radii obtained by this method for all samples are listed in Table 4.1.

Radii of the donor bound exciton

The determined (D^0, X) radii for the three samples with $x_0 = 0.05$ and n-doping concentrations between $2{\cdot}10^{17}\text{cm}^{-3}$ and $1.3{\cdot}10^{18}\text{cm}^{-3}$ are between 1.55 nm and 3.18 nm, decreasing with increasing dopant concentration. This might be caused by an enhanced interaction between the (D^0, X), which leads to a hampering of the expansion of the (D^0, X). Comparing the obtained (D^0, X) radii of sample BD-95, BD-230 and B0-175 with $x_0 = 0.07$, $x_0 = 0.05$ and $x_0 = 0.01$, respectively, a decrease of the radius is also observed for increasing Mn concentration. Kavokin et al. studied the (D^0, X) radii by magneto-optical probing of the magnetic polarons, for a set of $Cd_{1-x}Mn_xTe$ samples with Mn concentrations varying from $x = 0.1$ to $x = 0.4$. Here, a decrease of the (D^0, X) radius from 5 nm to 2 nm with increasing Mn content was detected [KMY+99]. Thus, these data show the same trend and the same scaling as the ESFRS-derived results for (Zn,Mn)Se, which are presented here.

Radii of the free exciton

The ESFRS-derived (X^0) radii of the four samples BD-95, BD-229, BD-230 and BD-274 are between 2.1 nm and 11.5 nm. Overall, the resulting (X^0) radii are larger than the corresponding (D^0, X) radii. Due to the unbound charac-

ter of the (X^0) it can encompass a larger area, which effectively has the same consequence as an apparently increased radius of the (X^0). Thus, the obtained larger radii of the (X^0) seem reasonable. Moreover, the (X^0) radius decreases with increasing n-doping concentration. This might be caused by a increased scattering probability of the (X^0) with the Cl donors. This potentially decreases the lifetime of the (X^0) and therefore, decreases the effective covered area of the (X^0). Especially for sample BD-274 with an n-doping concentration of $n = 1.3 \cdot 10^{18}\text{cm}^{-3}$, which lies above the metal-insulator transition $n_c \approx 7 \cdot 10^{17}\text{cm}^{-3}$, a drastic decrease of the (X^0) occurs and the determined (X^0) radius $r = 2.09\,\text{nm}$ is comparable to the obtained (D^0, X) radius of this sample. In the regime of such a high doping concentration, the (X^0) can scatter on free carriers [CPS93] [KH81]. Moreover, in this n-doping regime, the average distance of the dopants approaches the exciton radius and the energy of the Coulomb interaction of electron and hole is comparable to the Coulomb potential screening. As a consequence, the exciton becomes unstable and decays into a separated electron and hole [DRA+91]. Both effects shortened the (X^0) lifetime, which manifests itself as the observed reduction of the (X^0) radius.

4.3 Heating of the Mn spin system by photoexcitation

In the previous section, the B-field dependence on the ESFRS resonance profile width was presented. The analysis is based on local Mn fluctuations, which cause Mn concentration dependent splitting of the energy levels with opposite spin in an external B-field. According to Eq. (1.29), the splitting not only depends on the external B-field but also on the temperature, or to be more precise on the ratio of B/T. The bath temperature during all experiments was kept between $T = 1.4\,\text{K}$ and $1.7\,\text{K}$. Considering the anti ferromagnetic temperature T_{AF} of up to $2.2\,\text{K}$ for the set of studied samples (see Eq. (1.19)), the variation of the relevant temperature $T + T_{AF}$ is about 8 %. When considering the antiferromagnetic temperature T_{AF}, which is between $1\,\text{K}$ and $2.2\,\text{K}$ for the studied samples [see Eq. (1.19)], the bath temperature fluctuations have only a minor effect on the experimental results. However, it was shown by Keller et al., that optical excitation can heat the Mn spin system and a temperature

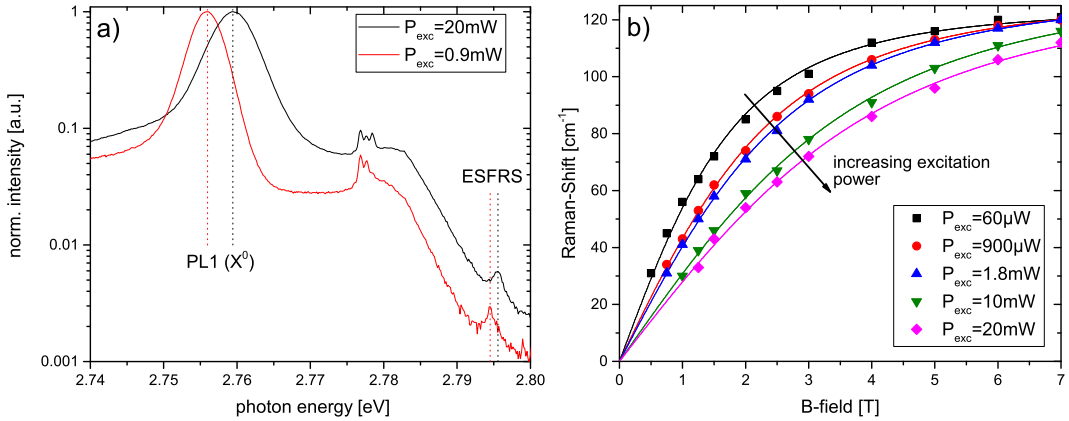

Figure 4.10: a) Spectra of sample BD-230 in (σ, π) Voigt configuration at $B = 7\,\mathrm{T}$, excitation energy $E_{exc} = 2.8095\,\mathrm{eV}$, with an excitation power $P_{exc,1} = 0.9\,\mathrm{mW}$ (red) and $P_{exc,2} = 20\,\mathrm{mW}$ (black). The dotted lines mark the PL 1 (X^0) transition and ESFRS peak. b) The Raman-shift of the ESFRS peak at B-fields ranging from 0.5 T to 7 T and excitation energies from $60\mu W$ up to 20 mW. The lines are Brillouin function fits to the data points.

increase of up to $T = 40\,\mathrm{K}$ was observed [KYK+01]. This possible temperature increase is one order of magnitude larger than the sum of the bath and antiferromagnetic temperature. Therefore, it is important to consider any heating effects, when a B-field dependence behavior is analyzed. In this section, the impact of the excitation power on the ESFRS process is studied.

In Fig. 4.10 a), two spectra of sample BD-230 at $B = 7\,\mathrm{T}$, excitation energy $E_{exc} = 2.8095\,\mathrm{eV}$ and the excitation powers $P_{exc,1} = 0.9\,\mathrm{mW}$ and $P_{exc,2} = 20\,\mathrm{mW}$ in (σ, π)-configuration are plotted. For reason of better comparability, both spectra are normalized to their respective maximum PL signal, which corresponds to PL 1 of the (X^0). The PL and the ESFRS peak are shifted to higher absolute scattered photon energies by 3.5 meV and 1 meV, respectively, when the excitation power is increased from 0.9 mW to 20 mW. This implies that the splitting of the electronic states with opposite spin by their exchange interaction with the spin-polarized Mn ions is reduced with increasing excitation power. Therefore it clearly indicates an irradiation-induced heating of the Mn spin system.

For a quantitative study of the Mn spin system heating, the ESFRS signal is measured at B-fields between 0 T to 7 T, with the excitation energy $E_{exc} = 2.8095\,\mathrm{eV}$ and excitation powers ranging from 0.06 mW to 20 mW. The B-field sweeps of the ESFRS signal for the set of excitation powers is plotted

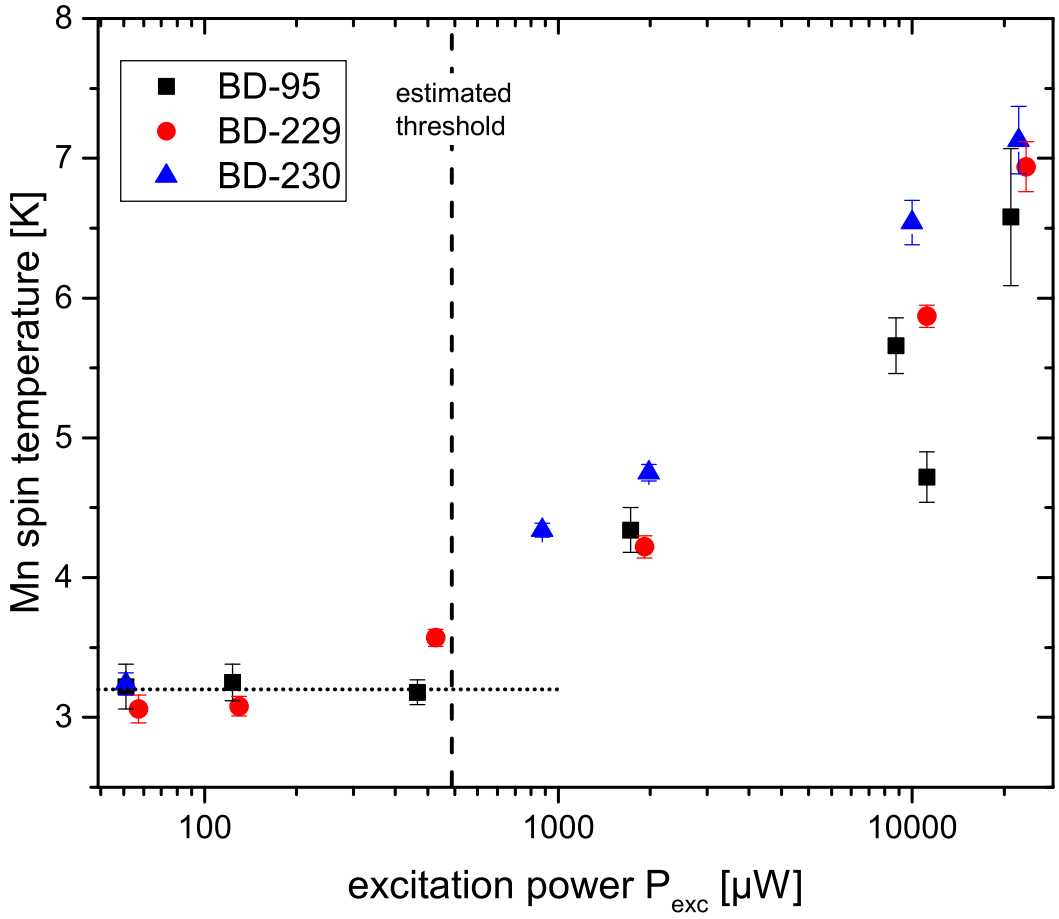

Figure 4.11: Experimentally determined Mn spin temperature for excitation powers P_{exc} ranging from $60\mu W$ to 20 mW for samples BD-95 (black squares), BD-229 (red circles) and BD-230 (blue triangles). The dotted horizontal line marks the expected Mn temperature, calculated by the sum of the bath temperature $T = 1.5\,\mathrm{K}$ and the antiferromagnetic temperature $T_{AF} = 1.8\,\mathrm{K}$ for $x = 0.05$ without additional heating. Above the power threshold of $P_{crit} = 0.5\,\mathrm{mW}$, an increase of the Mn spin temperature up to 7.1 K occurs.

in Fig. (4.10) b). Each curve shows a Brillouin-like behavior. The ESFRS peak position curve is flattened with increasing excitation power. The fits of the curves by Brillouin functions according to Eq. 1.29 allow an accurate determination of the Mn spin temperature values and the Raman-shift of ESFRS energy in saturation, i.e. $B \to \infty$. The saturation is power independent $\tilde{\nu}_{B\to\infty} = (127 \pm 2)\mathrm{cm}^{-1}$, whereas the spin temperature rises from 3.2 K to 7.2 K with increasing excitation power. The lowest observed temperature is identical to $T + T_{AF}$, hence in this case no detectable optical heating of the spin system occurs. The increase of the spin temperature to $T = 7.2\,\mathrm{K}$ effectively reduces

the spin orientation induced by the external magnetic field by a factor of two, which is especially noticeable in the linear regime of the Brillouin function. For example, the observed Raman-Shift of the ESFRS peak, at $B = 1.5\,\mathrm{T}$ and $P_{exc} = 60\mu W$ is almost identical to the value at $B = 3\,\mathrm{T}$ and $P_{exc} = 20\,\mathrm{mW}$. The evaluated Mn spin temperature of samples BD-95; BD-229 and BD-230 for excitation powers between $P_{exc} = 60\mu W$ and $P_{exc} = 20\,\mathrm{mW}$ are plotted in Fig. 4.11. For excitation powers below 0.5 mW, the experimentally determined Mn spin temperature is close to the calculated temperature of 3.2 K without a temperature increase caused by optical excitation of the electron system. Above $P_{exc} = 0.5\,\mathrm{mW}$ an increase of the Mn spin temperature occurs. This observation is in good agreement with results by Keller et al. [KYK$^+$01]. To ensure that a possible heating effect does not distort the ESFRS resonance analysis, all previously shown resonance curves were measured at excitation powers below 0.5 mW.

In principle, the power dependent behavior of the PL could also be used to calculate the spin temperature. However, this has two major drawbacks: first, the transition from the (D^0, X) to the (X^0) thermally stable state with increasing B-fields hinders the exact determination of the energy position of (D^0, X) and (X^0) assigned PL peaks for the whole B-field range. This leads to a larger fit error, when the Brillouin function is fitted to the data points.

Second, the hot electron gas, generated by photoexcited carriers, can interact with Mn ions and thereby increase the Mn spin temperature. König et al. showed, that the relevant interaction strength depends on the Mn concentration, the optically pumped carrier concentration, and the external B-field [KMY$^+$00]. Due to the B-field dependence of the Mn spin temperature, the shift of the PL in an external B-Field cannot be described by the Brillouin function, when an hot electron gas is induced. Therefore, the ESFRS method manifests itself as a comparatively straightforward tool for a direct determination of the irradiation-induced heating of the Mn spin system.

Chapter 5

Analysis of the ESFRS peak shape

In this chapter, the shape of the ESFRS peak is studied in detail. The motivation for the analysis is the unusual asymmetry of this peak, manifested as a tail at the low Raman-shift side. The peak shape is analyzed for B-fields between $1.25\,\mathrm{T}$ *and* $7\,\mathrm{T}$ *and various excitation energies. The asymmetry of the ESFRS peak shape is especially noticeable, when the ESFRS signal is enhanced by fulfilling the ingoing resonance condition (see chapter 4) and at high external magnetic fields.*

A model is proposed explaining these observations. It is based on the antiferromagnetic (d-d) interaction between neighboring Mn-ions and the finite size of the donor-bound (D^0, X) and free exciton (X^0), thus offering an additional approach for the estimation of the (D^0, X) and (X^0) radii. The obtained radii are between $2.4\,\mathrm{nm}$ *and* $2.6\,\mathrm{nm}$ *for the (D^0, X) and* $3.9\,\mathrm{nm}$ *for the (X^0). These results are compared with the findings obtained by the analysis of the ESFRS resonance broadening presented in chapter 4.*

5.1 Introduction

The formation of clusters of magnetic ions in a DMS reduces the number of magnetically active Mn ions, which are responsible for the giant Zeeman effect and hence for the ESFRS. To include the impact of the reducded number of magnetically active Mn ions on optical experiments, an effective concentration x_{eff} must be considered. A model for the calculation of x_{eff} is presented in section 1.3.1, which will be extended in this chapter to consider the effect of local manganese concentrations on the ESFRS peak shape.
At a critical chemical concentration, the cluster formation exceeds the effect of new incorporated magnetic ions, thus even reducing x_{eff} by increasing x. Hence, between x and x_{eff} a nonlinear relation exists, which is either calculated by a theoretical model [SFR$^+$84] or often obtained by experimental results, for example by photoluminescence or Raman spectroscopy measurements [KYK$^+$01] [TAT$^+$99]. Usually, the determined x_{eff} parameter is treated as one single value, valid for the entire sample. This implies the assumption that the magnetic ions are distributed homogeneously and no spatially local effects contribute to the studied physical process. However, as shown in chapter 4, the ESFRS process can be mediated via the spatially confined donor bound exciton (D^0, X). In this case, the fluctuation of the local Mn concentration x_{loc} caused by the random distribution of these ions on the sublattice must be considered. As as consequence, to include the (d-d) interaction on a small local scale, an effective local Mn concentration $x_{eff,loc}$ is introduced here. The influence of the $x_{eff,loc}$ distribution on the ESFRS peak shape is subject of this chapter.

Key element of the model to calculate x_{eff}, introduced by Shapira et al., is the consideration of the probability for finding single magnetic ions, pairs of magnetic ions and closed or open chains of three particles on the sublattice of the crystal, in combination with their magnetic moment [SFR$^+$84]. According to Saphira et al. larger structures must only be considered for concentrations $x > 0.1$. The calculation of x_{eff} for $x < 0.1$, which is the relevant range for the set of studied samples, reads as follows:

$$x_{eff}(x) = \frac{1}{5}x \cdot (x-1)^{12} \cdot \{5 + 2x^2 \cdot (x-1)^{10} \cdot [109 + 15x \cdot (5x-12)]\} \quad (5.1)$$

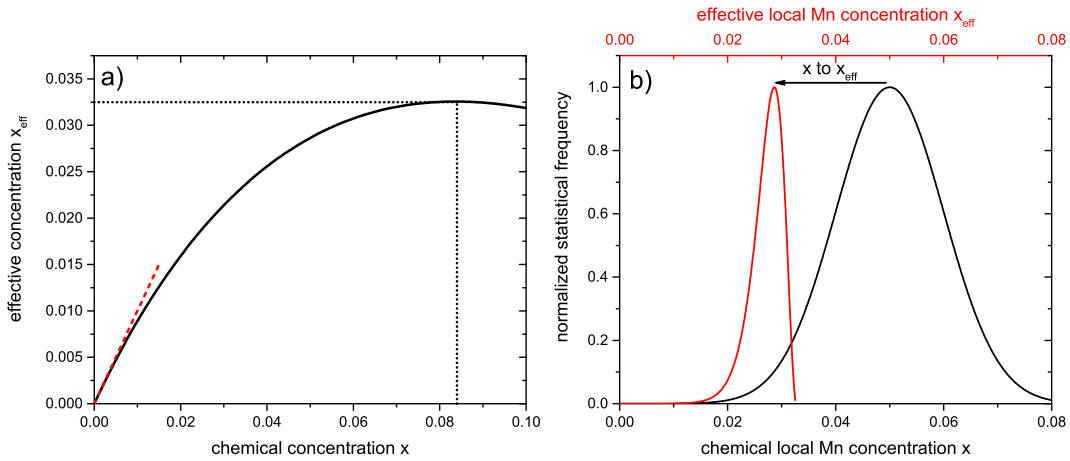

Figure 5.1: a) The x to x_{eff} relation according to Shapira et al. The black dotted horizontal line marks the maximum $x_{eff} = 0.033$ at $x = 0.084$, the red dashed line is a linear x to x_{eff} approximation for x<0.015 [SFR$^+$84]. b) Local Mn concentration distribution. Black: A normal distributed local Mn concentration centered at $x = 0.05$ with FWHM = 0.024. Red: The deviating concentration distribution after transforming x to x_{eff}. The maximum is shifted to $x_{eff} = 0.029$ and the width reduced to FWHM = 0.006.

For x ranging from 0 to 0.1, the resulting x_{eff} values are plotted in Fig. 5.1 a). For $x < 0.01$, $x_{eff}(x)$ can be approximated linearly, which is visualized by the red dashed line. Above $x = 0.01$ the effect of cluster formation arises and thus, a deviation from the linear trend appears. Moreover, these clusters start to become dominant for concentrations above $x = 0.084$, reducing the effective concentration. Hence, the maximum effective concentration of $x_{eff} = 0.033$ is achieved at a chemical concentration of $x = 0.084$.

When local effects like the (D^0, X) assisted electron spin flip are studied, the effective local Mn concentration $x_{eff,loc}$ must be considered, which is derived from the local concentration x_{loc}. The local concentration is defined as the number of Mn ions within a specific volume (e.g. the (D^0, X) volume) normalized to the total number of cation sites in this volume. Assuming that the Mn ions are randomly distributed on the sublattice, the local concentration for a set of (D^0, X) is described by a normal distribution (for more details, see appendix section A). An exemplary x_{loc} distribution, with a maximum at $x_0 = 0.05$ and a standard deviation $\sigma = 0.01$, equal to a FWHM = 0.024 is plotted in Fig. 5.1 b) (black curve). To include local effects and the reduction of the magnetically active Mn ions due to (d-d) interaction, the x_{loc} distribution must be transformed according to Eq. (5.1). The resulting $x_{eff,loc}$ distribution

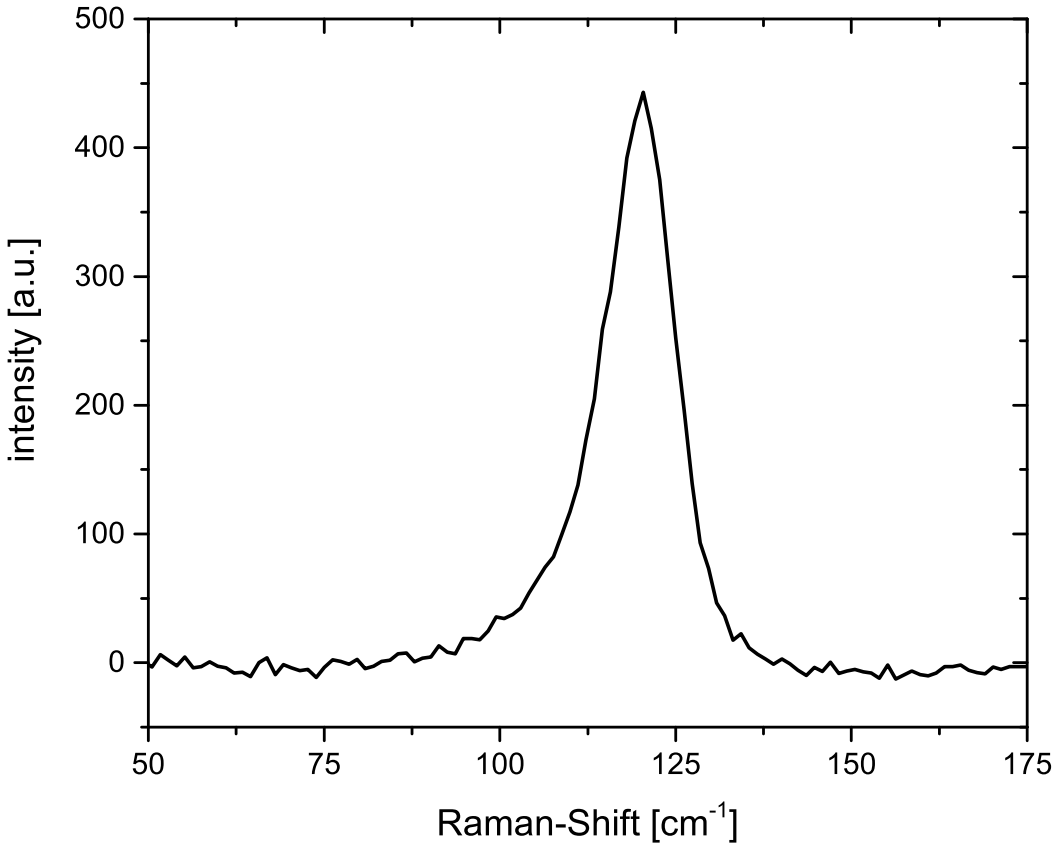

Figure 5.2: Background corrected resonant ESFRS spectrum of sample BD-230 at $B = 7\,\mathrm{T}$, $T = 1.7\,\mathrm{K}$ and an excitation energy of $E_{exc} = 2.8177\,\mathrm{eV}$.

is also plotted in Fig. 5.1 b) (red curve). It is striking, that the former normal distribution becomes distorted. Not only the maximum is shifted from $x = 0.05$ to $x_{eff} = 0.029$, but moreover the FWHM is reduced to $\sigma = 0.006$ and the shape of the distribution becomes asymmetric. This is due to the non-linear reduction of $x_{eff,loc}$ for larger x_{loc}, which shifts the distribution unevenly.
Due to the (s-d) and the (p-d) interaction, the spin splitting of the CB and VB states in an external magnetic field B depends on the temperature T and on the effective concentration of the Mn ions x_{eff}. According to Eqs. (1.28) and (1.29), the band splitting is directly proportional to x_{eff}. Thus, it is reasonable to assume that the x_{eff} distribution will directly affect the energy distribution of the band splitting. The CB splitting is directly probed by energy of the ESFRS transition. Therefore the ESFRS peak shape analysis is a useful method to study the influence of the x_{eff} distribution on the CB splitting.

To investigate this assumption, the ESFRS peak is experimentally recorded at $B = 7\,\mathrm{T}$ and a helium bath temperature of $T = 1.7\,\mathrm{K}$. At these experi-

mental parameters, virtually all single Mn ions are in their ground state with $m_j = -5/2$, which leads to a saturation of the band splitting. Consequently, the effect of the varying local Mn concentrations on the CB states is maximized. This is the optimal condition to study the variation of the $x_{eff,loc}$ distribution. A typical, background subtracted ESFRS spectrum of sample BD-230 at these experimental conditions and an excitation energy E_{exc} of 2.8177 eV is shown in Fig. 5.2. This excitation energy is almost identical with the energy of the optical transition no. 6, leading to a strong resonance enhancement of the ESFRS process. The advantage to study the ESFRS peak at resonance conditions is a high signal to noise ratio, which allows a more reliable analysis of the ESFRS peak. Here, the observed ESFRS peak shows an asymmetry, especially pronounced at the low Raman-Shift side. At the first glance, the ESFRS peak resembles the shape of the exemplary x_{eff} distribution, shown in Fig. 5.1 b). The Raman shift of the peak maximum at $\tilde{\nu} = 120\,\mathrm{cm}^{-1}$ is below the expected value of $\tilde{\nu} = 144\,\mathrm{cm}^{-1}$ for $x = 0.05$ according to Eq. (1.29). Lentze et al. showed that for heavily n-doped samples electron states with wave vector $q \neq 0$ have to be considered, which carry an admixture of p-type wavefunctions. Therefore, the (p-d) interaction must also be considered for the CB splitting which results in a reduction of the exchange constant $N_0\alpha$ [LGG+07]. This effect is also included in the proposed ESFRS peak shape model. It will be shown, that the additional (p-d) interaction mixing even supports the model for the shape analysis.

5.2 ESFRS peak shape model

At a fixed external B-field and temperature, each effective Mn concentration x_{eff} yields one specific energy splitting of the CB [see Eq. (1.29)]. This energy is identical to the ESFRS energy, detected in this thesis by Raman spectroscopy. Hence, in the following section, the energy difference is defined as Raman-Shift in cm^{-1}. The B-field dependence of the CB splitting is described by the Brillouin function, thus detecting the ESFRS peak energy enables the evaluation of x_{eff} by the inverse of the Brillouin function. Eq. (5.1) is solved to calculate x by the obtained x_{eff} value. Due to the non linear relation between x and x_{eff}, there are two possible x values for one x_{eff}. Hence an additional restriction is required, to determine the physically reasonable solution. This

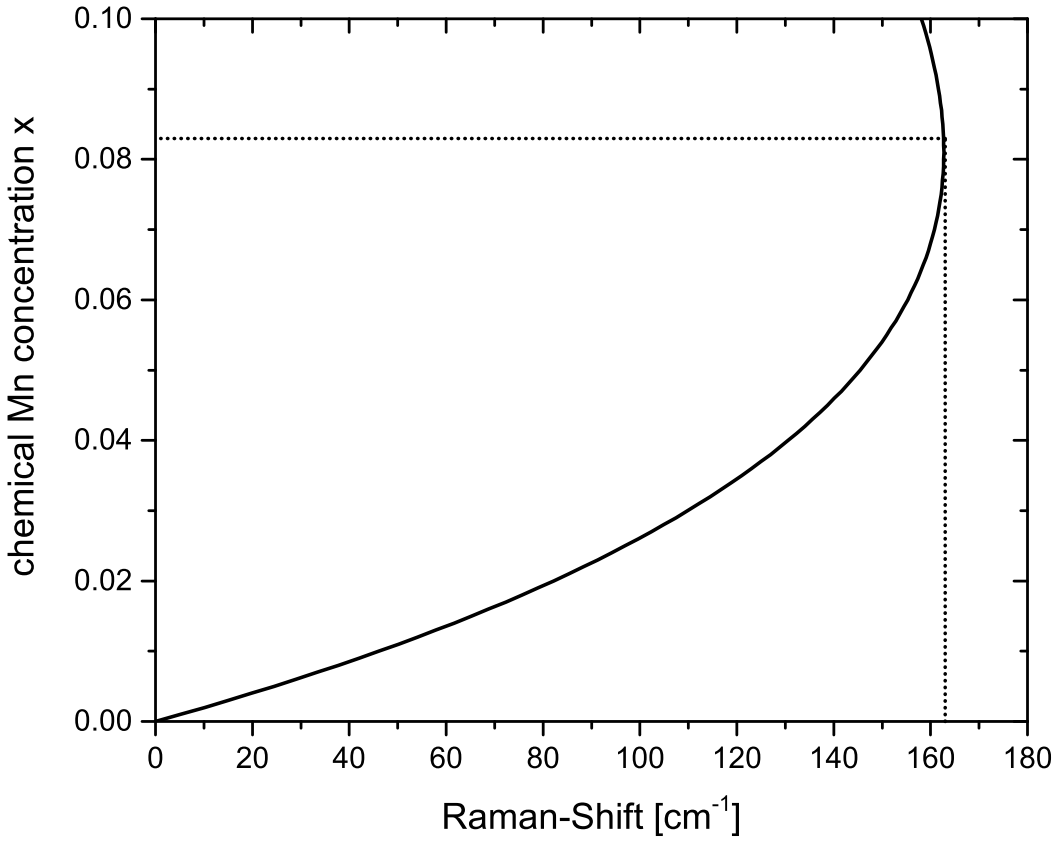

Figure 5.3: Chemical Mn concentration x vs. ESFRS spectral position at $B = 7\,\mathrm{T}$ and $T = 1.5\,\mathrm{K}$. Dashed lines mark the maximum achievable Raman-Shift of $\tilde{\nu} = 163\,\mathrm{cm}^{-1}$ resulting in $x = 0.084$.

is achieved by limiting the range of x in the transformation of Eq. (5.1). In the following quantitative analysis, this range is set to $x \in \{0 \leq x \leq 0.084\}$, which covers the x concentrations of the studied samples. Furthermore, the phenomenological parameter $T_{AF}(x)$ [Eq. (1.19)] depends on the Mn concentration x and therefore is also considered, in the inverse function $E_{CB}^{-1}(B, T, x)$ of Eq. (1.29). The resulting $E_{CB}^{-1}(B, T, x)$ at typical experimental parameters $B = 7\,\mathrm{T}$ and $T = 1.5\,\mathrm{K}$ versus the Raman-Shift is plotted in Fig. 5.3. For low chemical concentrations, the effect of the (d-d) interaction only slightly reduces x_{eff}, meaning $x_{eff} \approx x$. In contrast, above $\tilde{\nu} = 100\,\mathrm{cm}^{-1}$ ($x \approx 0.025$), the inverse function starts to deviate from the linear trend, caused by the increasing chance of the formation of Mn pairs at the corresponding Mn concentrations x. The effect of pair and cluster formations is seen by the observation that a maximum ESFRS Raman-Shift value of $\tilde{\nu}_{max} = 163\,\mathrm{cm}^{-1}$ at $x = 0.084$ is reached. Even higher x concentrations decrease x_{eff} and consequently also

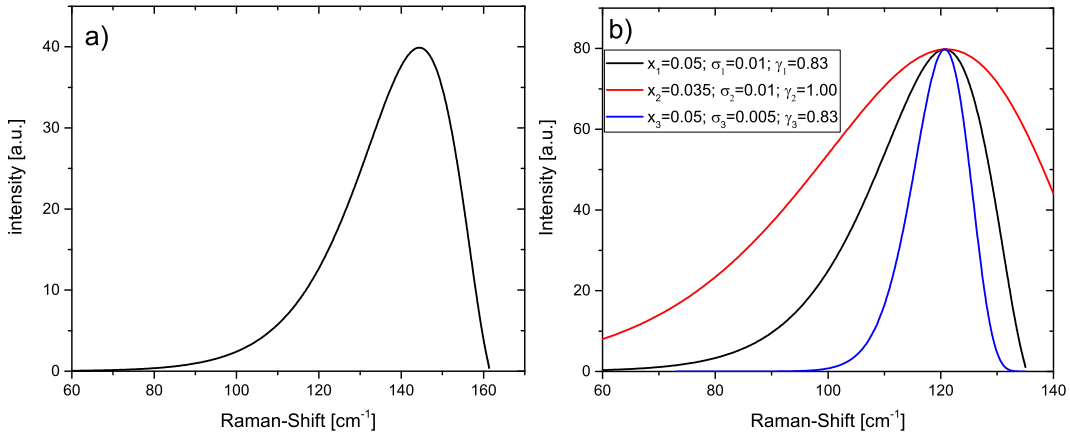

Figure 5.4: Simulated ESFRS peak at $B = 7\,\mathrm{T}$ and $T = 1.5\,\mathrm{K}$. a) For $x = 0.05$, $\sigma = 0.01$ and $\gamma = 1.00$, i.e. without (s-p) mixing. b) Impact of the simulation parameters on the ESFRS peak shape, considering the chemical concentration x, the standard deviation σ of the x distribution and the (s-p) mixing-induced reduction factor γ. The parameters used for the simulations are listed in the legend.

the ESFRS Raman-Shift, visualized in Fig. 5.3.
Besides the inverse function $E_{CB}^{-1}(B,T,x)$ an underlying distribution of x must be considered for the quantitative analysis of the ESFRS peak shape. As shown in section A, randomly located Mn ions on the cation sites lead to a normally distributed local chemical concentration, with its maximum at the mean chemical concentration. Hence, applying a normal distribution for x enables the simulation of the ESFRS peak shape via $E_{CB}^{-1}(B,T,x)$. Such a calculated ESFRS peak for $x = 0.05$ and a standard deviation of the normal distribution of $\sigma = 0.005$ at $B = 7\,\mathrm{T}$ and $T = 1.5\,\mathrm{K}$ is plotted in Fig. 5.4 a). The peak is asymmetric with a larger optical weight at lower Raman-Shifts. This resembles the shape of the experimentally measured ESFRS peak, shown in Fig. 5.2. Obviously the maximum of the calculated peaks, located at $\tilde{\nu} = 144\,\mathrm{cm}^{-1}$ does not coincide with the experimentally obtained value of $\tilde{\nu} = 120\,\mathrm{cm}^{-1}$. The deviation is caused by the n-doping of the sample, which induces an (s-p) mixing and lowers the CB splitting [LGG+07]. Consequently, an adjustment of $E_{CB}(B,T,x)$ is required.

The lowering of the ESFRS energy is described by the introduction of (s-p) mixing-induced reduction factor γ as prefactor in Eq. (1.29). At $B = 7\,\mathrm{T}$ and $T = 1.5\,\mathrm{K}$, a Mn concentration $x_1 = 0.05$, yielding $x_{eff,1} = 0.029$ and $\gamma_1 = 0.83$ results in the simulated ESFRS maximum at $\tilde{\nu} = 120\,\mathrm{cm}^{-1}$. This is identical

to the experimentally observed value, shown in Fig. 5.2. $\gamma = 0.83$ is reasonable for an n-doping concentration of $n = 4.2 \cdot 10^{17} cm^{-3}$ [LGG+07]. In principle, a reduction of the ESFRS spectral position might not only originate from (s-p) mixing, (i.e. $\gamma < 1$), but might also result from a lower Mn concentration. The obtained ESFRS maximum of $\tilde{\nu} = 120\,\mathrm{cm}^{-1}$ could result from a chemical concentration $x_2 = 0.035$ which corresponds to a effective concentration $x_{eff,2} = 0.024$. Assuming a standard deviation $\sigma = 0.01$ of the x distribution, the simulated ESFRS peaks for $x_{eff,1} = 0.029$ & $\gamma_1 = 0.83$ and $x_{eff,2} = 0.024$ & $\gamma_2 = 1.00$ are shown in Fig. 5.4 b) as the black and red curve, respectively. As expected, the peak maxima occur at the identical Raman-Shift of $\tilde{\nu} = 120\,\mathrm{cm}^{-1}$. Thus, the maximum position is not sufficient to determine x and γ without the use of additional experimentally obtained results.

Although the maximum position of the simulated peaks are identical, they show a clearly distinguishable peak shape. The ESFRS peak for $x = 0.035$ is less asymmetric and much broader compared to $x = 0.05$, although the identical σ is used for the simulation. For $x = 0.035$, the peak remains almost Gaussian, due to the less pronounced influence of the (d-d) interaction on x_{eff} close to this x concentration. Thus, the shape analysis can be used to verify influence of the (s-p) mixing on the CB splitting, without requiring the input parameter of an n-doping or Mn concentration. Instead, here the two parameters are the disentangled outcome of the peak shape analysis.

To show the influence of the width of the x distribution, an additional ESFRS peak is simulated, with the parameters $x_3 = 0.05$, $\gamma_3 = 0.83$ and $\sigma_3 = 0.005$, which is half the width used for the two previous simulations and plotted in Fig. 5.4 b). Not surprisingly, the maximum of all three ESFRS peaks is identical at $\tilde{\nu} = 120\,\mathrm{cm}^{-1}$, because the relevant parameters to determine the maximum position of the ESFRS peak, x_3 and γ_3 are identical to x_2 and γ_2. However, the width of the x distribution is reflected directly in the width of their corresponding ESFRS peaks. Thus, a narrower distribution results in the narrower ESFRS peak and a less pronounced asymmetry arises. This can be explained by the relation between x and x_{eff}. Comparable x result in similar x_{eff} values, therefore the different strength of the (d-d) interaction becomes more noticeable for a broader x range. This leads to a pronounced asymmetry of the x_{eff} distribution for a larger standard deviation σ, especially in the concentration regime $x > 0.01$ where the x_{eff} values start to deviate from the x values.

5.3 Quantitative ESFRS peak shape analysis

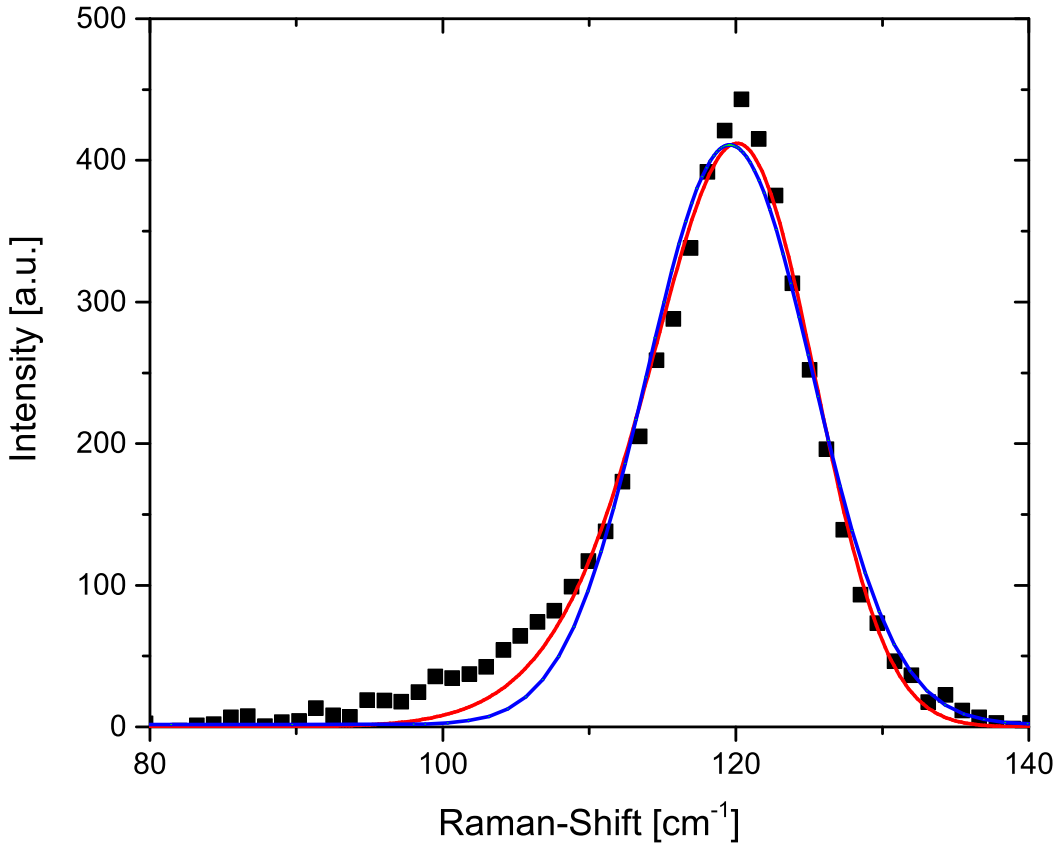

Figure 5.5: Near resonance ESFRS spectrum of BD-229 at $B = 7\,\mathrm{T}$ and $T = 1.7\,\mathrm{K}$. The red curve is the fit to the data based on the proposed model, yielding $x = 0.0049$, $\sigma = 0.005$ and $\gamma = 0.84$. The blue curve is a simple Gaussian fit.

The ESFRS peak of sample BD-229 at $B = 7\,\mathrm{T}$ and $T = 1.7\,\mathrm{K}$ near resonance excitation is fitted according to the previously introduced model. The experimentally recorded ESFRS signal and the corresponding fit results are shown in Fig. 5.5. Here, the fit nicely matches experimental results, yielding $x = 0.049$, $\sigma = 0.005$ and $\gamma = 0.84$. The fit result especially coincides with the asymmetric shape of the ESFRS peak. This becomes more striking when comparing the curve with a symmetrical Gaussian fit, plotted as the blue curve in Fig. 5.5. The fit according to the introduced model coincides better with the experimental results, indicating that the implemented assumptions describing the fit model are plausible. Moreover, the obtained fit result for x is in good agreement with XRD measurements on the identical sample. The obtained γ

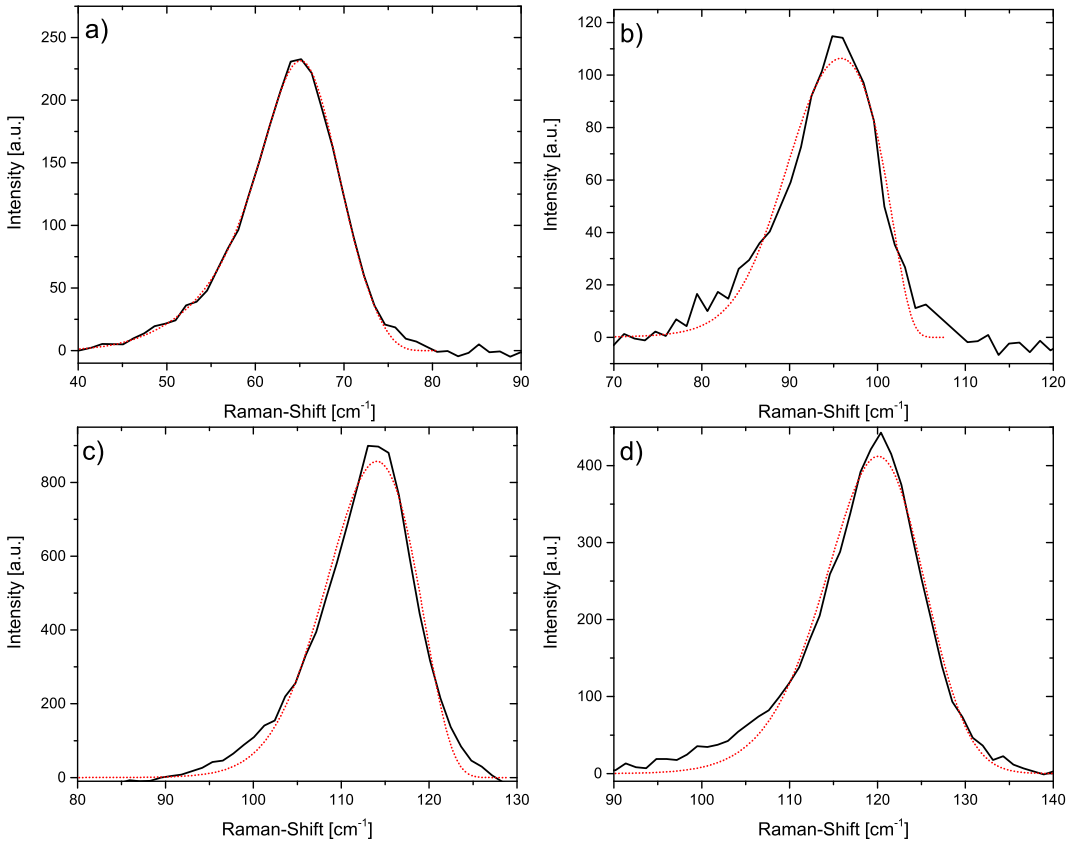

Figure 5.6: B-field dependent near resonance ESFRS spectra of sample BD-230 at $T = 1.5\,\mathrm{K}$. a) $B = 1.25\,\mathrm{T}$, b) $B = 2.5\,\mathrm{T}$, c) $B = 5\,\mathrm{T}$ and d) $B = 7\,\mathrm{T}$. The red dotted lines are fits based on the introduced model.

value nicely coincides with an estimated $\gamma \approx 0.77$ at a doping concentration of $n = 2{\cdot}10^{17}\mathrm{cm}^{-3}$, which is caused by the carrier induced (s-p) mixing [LGG^{+}07]. Due to the non constant PL background in the relevant spectral range for the ESFRS resonance, the PL background subtraction can lead to uncertainties of the data points plotted in Fig. 5.5. This can explain the deviation of the experimental results and the asymmetric fit at low Raman-Shifts. For a validation of the obtained σ, its value is compared to the results of the analysis of the ESFRS resonance broadening, which yields $\sigma = 0.004$ [see Tab. 4.1 ($\sigma \approx$ FWHM/2.35)]. Both methods give similar results, strengthening the validity of the introduced model.

According to Eq. (1.29) the CB splitting depends on the B-field and therefore the B-field possibly affects the ESFRS peak shape. Thus, the next step is the ESFRS peak shape analysis at various B-fields. Spectra of sample BD-230 at $B = 1.25\,\mathrm{T}$, $2.5\,\mathrm{T}$, $5\,\mathrm{T}$, and $7\,\mathrm{T}$ are plotted in Fig. 5.6. a) to d). For each

Table 5.1: Fit results based on the asymmetric ESFRS shape model of sample BD-230 for different B-fields, with the Raman-Shift of the ESFRS peak $\tilde{\nu}$, the maximum and width of the chemical concentration distribution x and σ, the prefactor γ and the estimated (D^0, X) radius.

B[T]	$\tilde{\nu}$ [cm^{-1}]	$x[10^{-2}]$	σ [10^{-3}]	γ	(D^0, X) radius [nm]
1.25	65	2.8	4.7	1.09	2.38
2.5	95	4.3	5.5	0.90	2.46
5	114	4.8	4.9	0.84	2.75
7	120	4.9	5.3	0.84	2.62

magnetic field, the excitation energy is adjusted to fulfill the resonance condition of the (D^0, X) assisted ESFRS process (see chapter 4), leading to an E_{exc} ranging from 2.8084 eV to 2.8177 eV. The observed ESFRS peak shifts from $\tilde{\nu} = 65\,\text{cm}^{-1}$ at $B = 1.25\,\text{T}$ to $\tilde{\nu} = 120\,\text{cm}^{-1}$ at $B = 7\,\text{T}$, reflecting the larger CB splitting at higher B-fields. Moreover, the peak asymmetry becomes more pronounced with increasing B-field. For a quantitative analysis of these peaks, each one is fitted by the introduced asymmetric fit function. The resulting fits are shown in Fig. 5.6. a) to d), which nicely reproduce the measured ESFRS peak at each B-field and the corresponding degree of asymmetry. The obtained fit parameters are listed in Tab. 5.1. The measurements at the two highest B-fields yield almost identical parameters because the CB splitting is near saturation at these magnetic fields. This is seen when comparing the positions of the ESFRS peak maxima, which show an increase of only $\Delta\tilde{\nu} = 6\,\text{cm}^{-1}$ for B from 5 T to 7 T. Therefore, the peak shape should also not change dramatically. With decreasing B-field, the calculated x value becomes smaller, due to the more symmetrical peak shape at low magnetic fields. At $B = 1.25\,\text{T}$ the CB splitting is roughly only half the value of the splitting at $B = 7\,\text{T}$. Hence, the variation of x causes a less pronounced broadening of the CB splitting and therefore, the asymmetry of the ESFRS peak becomes not resolvable by the used experimental method and this can explain why γ exceeds the value one at $B = 1.25\,\text{T}$, which is is physically not reasonable. This demonstrates the limitation of the peak shape analysis.

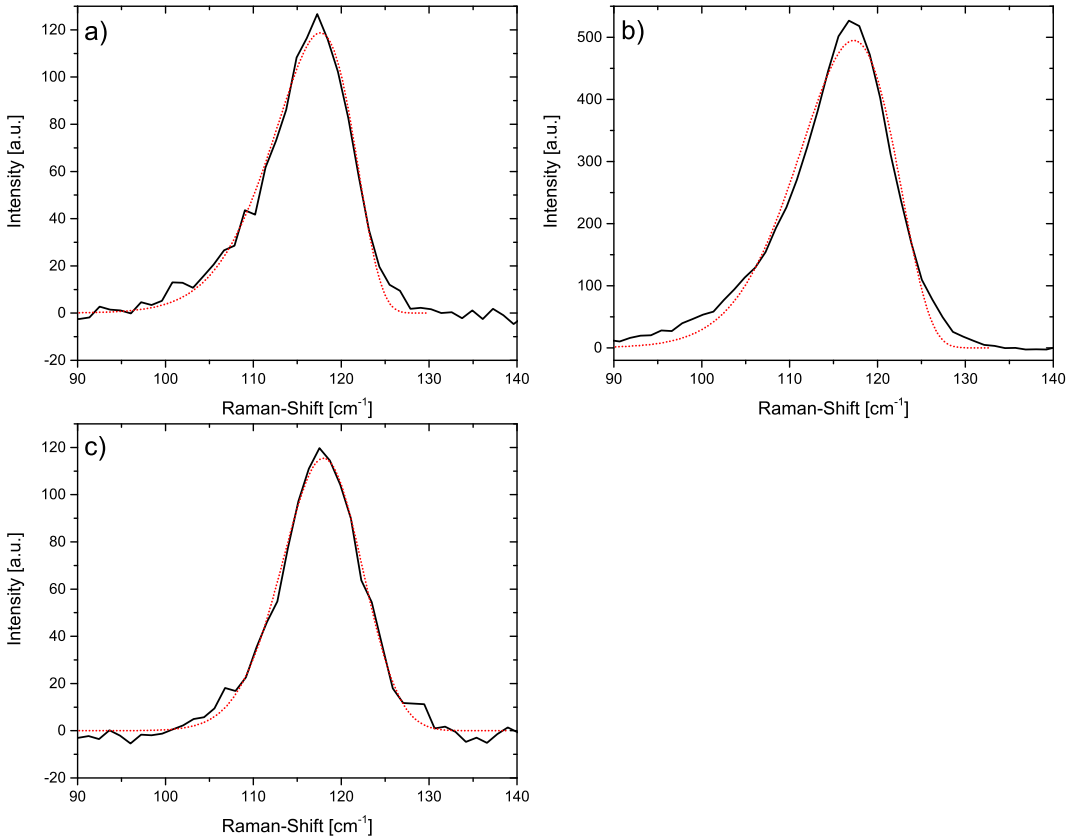

Figure 5.7: Excitation energy dependent spectra of sample BD-229 at $B = 5\,\mathrm{T}$. a) below resonance excitation $E_{exc} = 2.8117\,\mathrm{eV}$ b) in resonance excitation $E_{exc} = 2.8194\,\mathrm{eV}$ and c) above resonance excitation $E_{exc} = 2.8285\,\mathrm{eV}$. The red dotted lines are fits based on the introduced model.

5.3.1 Determination of the (D^0, X) and (X^0) radii by ESFRS peak shape analysis

As explained in chapter 4, due to the statistical properties of the x distribution, an estimation of the spatial extent of (D^0, X) and (X^0) is possible. As mentioned before, at each B-field the excitation energy is adjusted to fulfill the (D^0, X) assisted ESFRS resonance. Hence, the resulting radii listed in Tab. 5.1, are related to the (D^0, X). These range between 2.38 nm and 2.75 nm, which is similar to the value of 2.04 nm determined by the ESFRS resonance broadening. Thus, the ESFRS shape analysis and the ESFRS resonance broadening are equally valid methods to estimate the (D^0, X) radius.

Besides the B-field dependence of the ESFRS peak shape, the influence of the excitation energy can reveal further information about the transition from the (D^0, X) to the (X^0) assisted ESFRS process. Three spectra, with an ex-

Table 5.2: Fit results based on the asymmetric ESFRS shape model of sample BD-229 for different excitation energies E_{exc}, with the maximum and width of the chemical concentration distribution x and σ, the prefactor γ and the estimated radius, which is either attributed to the (D^0, X) or (X^0).

E_{exc}[eV]	$x[10^{-2}]$	σ $[10^{-3}]$	γ	radius [nm]	note
2.8117	5.3	6.0	0.83	2.48	below resonance
2.8194	4.9	5.7	0.85	2.50	in resonance
2.8285	3.6	2.5	1.00	3.92	above resonance

citation energy above, in, and below the ESFRS resonance of sample BD-230 at $B = 7\,\mathrm{T}$ and their corresponding asymmetric fits are plotted in Fig. 5.7. The calculated fit parameters are listed in Tab. 5.2. In the case of near and below resonance excitation, the ESFRS peaks show a noticeable asymmetry and hence, yield comparable fit results. Furthermore, the estimated radii are in accordance with the result of the (D^0, X) obtained by the analysis of the ESFRS resonance broadening. This is reasonable, because at an excitation energy below and near the ESFRS resonance, the (D^0, X) assisted ESFRS process is mainly probed.

At the highest excitation energy, the ESFRS peak becomes more symmetrical, leading to a lower x and a larger γ value. As explained for the low B-field measurements, the obtained fit results of x and γ are not reliable, when the ESFRS peak shows no pronounced asymmetry. However, the calculated σ still gives further insight into the underlying ESFRS process. It is about half the value, compared to the σ value at the other two excitation energies. This results in a distinct increase of the calculated particle radius. At the excitation energy of $E_{exc} = 2.8285\,\mathrm{eV}$, the ($X^0$) mainly contribute to the ESFRS scattering efficiency, thus the calculated radius is assigned to the (X^0). The larger radius of the (X^0) compared to the (D^0, X), reflects the unbound character of the (X^0). This is in line with the results obtained by the ESFRS resonance broadening (see chapter 4).

The Mn concentration x is the last accessible parameter, which can have an effect on the ESFRS peak shape. To study the influence of the Mn concentration x on the ESFRS shape, spectra of sample B0-175 and BD-230 are compared. These two samples have comparable n-doping concentrations of about $n = 4.2{\cdot}10^{17}\mathrm{cm}^{-3}$ but differ in Mn concentration: $x = 0.01$ for B0-175 and $x = 0.05$ for BD-230. Fig. 5.8 shows typical ESFRS spectra of both sam-

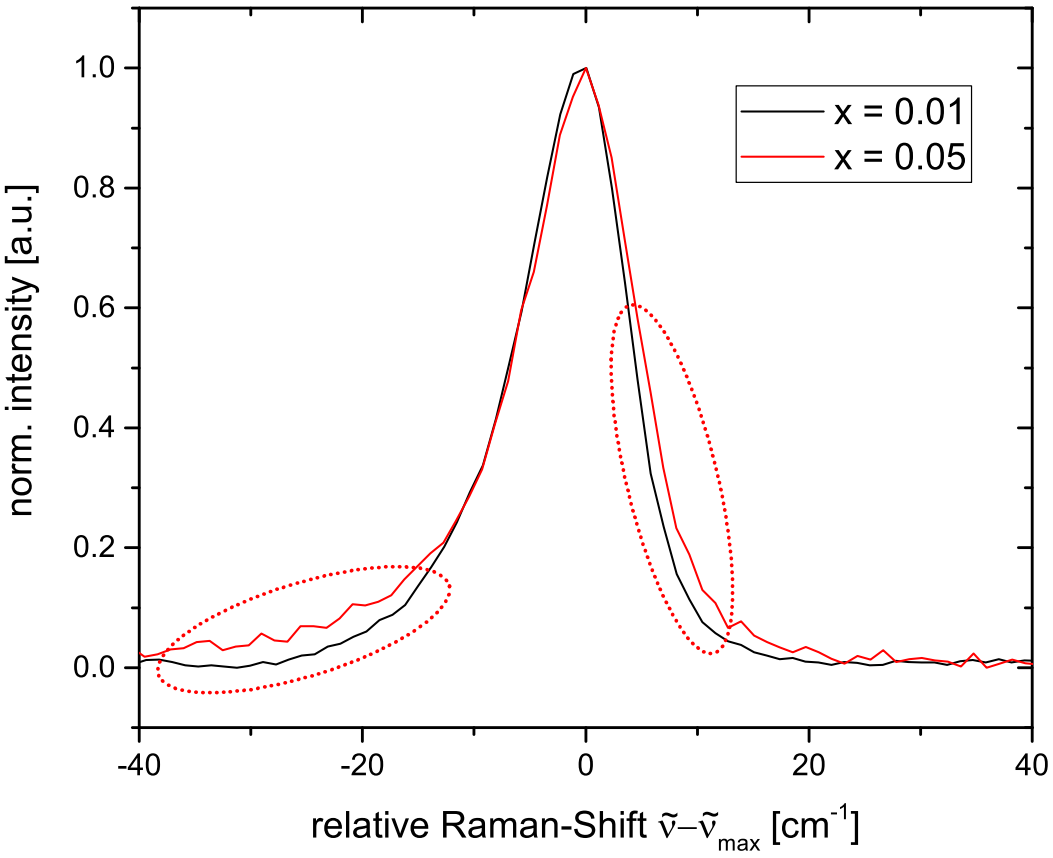

Figure 5.8: Spectra of sample B0-175, $x = 0.01$ (black curve) and BD-230, $x = 0.05$ (red curve). For a visual comparison, the peaks are centered at the frequency position $\tilde{\nu}_{max}$ of their maximum intensity. The red dotted ellipses are guides to the eye, to mark the area of maximum deviation between the two spectra.

ples at $B = 7\,\mathrm{T}$ and $T = 1.5\,\mathrm{K}$. In both cases the excitation energy is adjusted to match the ESFRS resonance, to ensure that the (D^0, X) is probed and to yield the maximum signal to noise ratio. For a better visual comparison, both spectra are background subtracted and centered at the frequency of their respective ESFRS peak maximum $\tilde{\nu}_{max}$.

The peak of sample B0-175 is slightly narrower and less asymmetric compared to the peak of sample BD-230, which differences are highlighted by the red dashed ellipsis. This is a first hint that the local Mn concentration indeed has an effect on the ESFRS peak shape. Due to the linear trend of the x to x_{eff} function at low concentrations, a more symmetrical peak for the low concentration sample is indeed expected.

For a quantitative analysis, the ESFRS peak of sample B0-175 is fitted by the

introduced model, which yields $x = 0.037$, $\sigma = 0.0048$ and $\gamma = 0.59$. The calculated x is larger than the value obtained by XRD measurements and consequently γ is smaller than the expected value for a n-doping concentration of $n = 4.2 \cdot 10^{17} cm^{-3}$. There are two major factors to consider, to explain this deviation. Due to the smaller x concentration, the CB and VB energy levels and therefore also the corresponding PL peaks are less separated. This leads to a more intense PL background at the ESFRS peak position, which hampers the correct background subtraction and hence, increases the inaccuracy of the background subtracted ESFRS peak shape. This could falsely create an asymmetry of the ESFRS peak, which would severely affect the fit result. A second reason for the deviation of the expected and observed ESFRS peak shape at low Mn concentration is an incorrect representation by the used x to x_{eff} transformation for $x < 0.01$. Shapira et al. used a strictly statistical method to determine the $x_{eff}(x)$ function. Here, they also presented experimental data, which in particular deviate from their model at concentrations below 0.05. This suggests that at low manganese concentrations, a complex non-linear x to x_{eff} dependence could exists, resulting in an asymmetric ESFRS peak even at low Mn concentrations.

Chapter 6

Direct and LO-assisted paramagnetic resonance of Mn^{2+}

In this chapter, the paramagnetic resonance of the magnetic Mn^{2+} ions in (ZnMn)Se:Cl is analyzed. The variation of the excitation energy results in a pronounced enhancement of the spin flip signal, i.e. of the probability of the Mn^{2+} d-electron spin flip process. Furthermore, the combined process of the creation of an LO phonon and a Mn spin flip is observed. This combined process shows a resonance at an excitation energy one LO phonon energy higher compared to the direct Mn spin flip resonance. The advantage of this sum process is the possibility to observe the Stokes and anti-Stokes Mn spin flip process simultaneously. The probability of the LO-assisted anti-Stokes Mn spin flip process not only depends on the excitation energy but also on the excitation power. At specific experimental conditions (i.e. in resonance excitation with high excitation power), even an inversion of the anti-Stokes to Stokes intensity occurs. This cannot be explained by the probability of occupancy of the d-electrons of the Mn^{2+} ions. Furthermore a detailed analysis of the LO-assisted anti-Stokes resonance reveals that the resonance consists of two partially overlapping peaks. A model is proposed to explain these observations and the influence of the n-doping concentration on this peak is discussed.

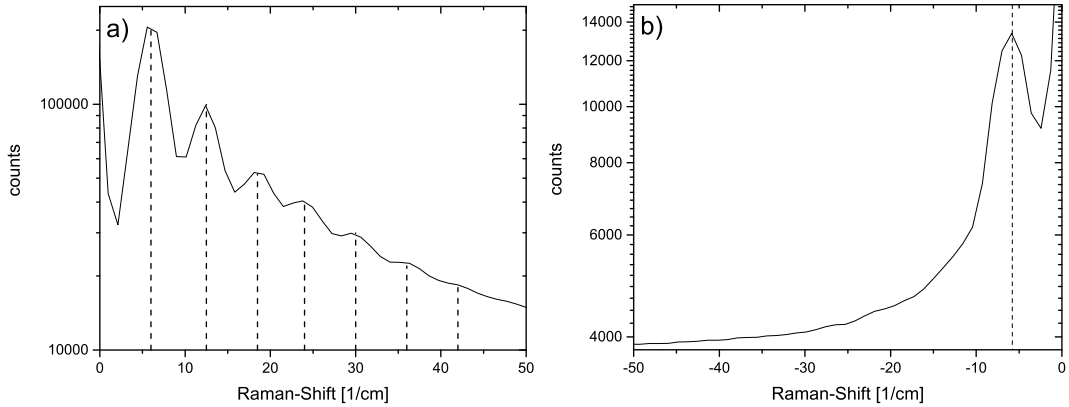

Figure 6.1: Two spectra of sample BD-95 in (σ, π) configuration at $B = 7\,\mathrm{T}$ and an excitation energy $E_{exc} = 2.7813\,\mathrm{eV}$. a) multiple equidistant Stokes Mn spin flip peaks, marked by dashed lines. b) anti-Stokes Mn spin flip, marked by a dashed line, at $\tilde{\nu} = -6\,\mathrm{cm}^{-1}$.

6.1 Resonant Raman spectroscopy of the direct Mn spin flip

A typical spectrum of the undoped sample BD-95 at an excitation energy $E_{exc} = 2.7813\,\mathrm{eV}$ and at helium bath temperature of $T = 1.5\,\mathrm{K}$, in $(\sigma,\ \pi)$ Voigt configuration is shown in Fig. 6.1 a). The Mn spin flip is clearly visible at a Raman-shift of $\tilde{\nu} = 6\,\mathrm{cm}^{-1}$, which yields in a g-factor ~ 2. Besides this peak up to six equidistant peaks separated by a Raman-Shift of $6\,\mathrm{cm}^{-1}$ are detected. These originate from multiple Mn spin flip processes [PPV$^+$83]. To measure the anti-Stokes Mn spin flip the first stage of the triple monochromator (i.e. the pre-monochromator) was repositioned to enable the detection of the high energy spectral range with respect to the laser frequency. All other experimental parameters (B-field, the excitation energy and power) were unchanged. The anti-Stokes Mn spin flip peak appears at $\tilde{\nu} = -6\,\mathrm{cm}^{-1}$ and is about 20 times weaker than the corresponding Stokes peak. This intensity ratio stands in line with the probability of occupancy of excited Mn^{2+} ions at a low temperature of 1.5 K, described by Boltzmann statistics. Furthermore, multiple anti-Stokes Mn spin flip processes are unlikely and hence, are experimentally not detectable.

Similar as for the electron spin flip process, the Mn spin flip Raman scattering efficiency is also expected to depend on the excitation energy. To analyze this assumption, the incident photon energy is tuned and for each step, a spec-

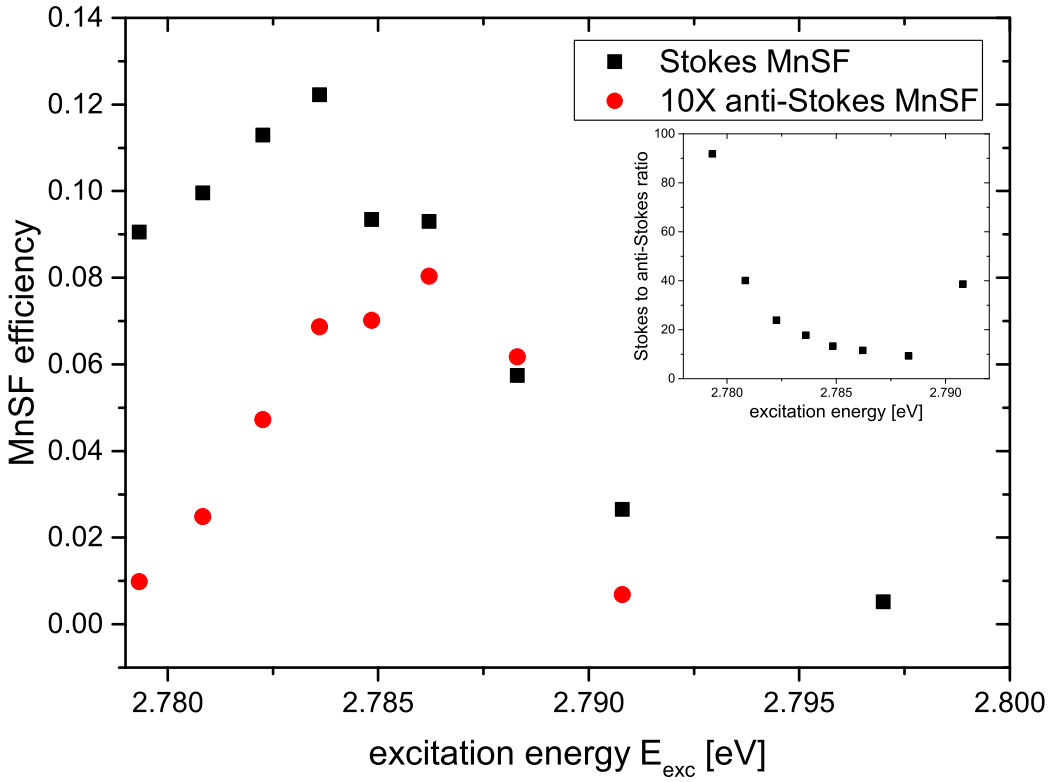

Figure 6.2: Resonance profile of the Stokes and anti-Stokes Mn spin flip. For better visualization, the Anti-Stokes efficiency is multiplied by ten. The inset shows Stokes to anti-Stokes intensity ratio.

trum is taken. The observed Stokes and anti-Stokes spin flip signals are fitted each by a Gaussian curve. The obtained area of the Gaussian fits is used as a measure to determine the scattering efficiency. In Fig. 6.2 the results for the direct Stokes and anti-Stokes Mn spin flip efficiency versus the excitation energy E_{exc} are plotted. For a better visualization of the enhancement profiles, the anti-Stokes Mn spin flip efficiency values are multiplied by ten. Through the full excitation energy range, the Stokes Mn spin flip intensity is larger than the intensity of the corresponding anti-Stokes process. Both processes exhibit a clear enhancement at specific excitation energies, with the intensity maximum at an excitation energy of $E_{res} = 2.7828\,\text{eV}$ and $E_{res} = 2.7856\,\text{eV}$ for the Stokes and anti-Stokes process, respectively. For an outgoing resonance, the excitation energy E_{res} for the maximum enhancement should be lower for the anti-Stokes compared to the Stokes process. This is not observed here. Instead the deviation of excitation energies can be attributed to experimental uncertainty, especially when considering the relatively weak anti-Stokes spin

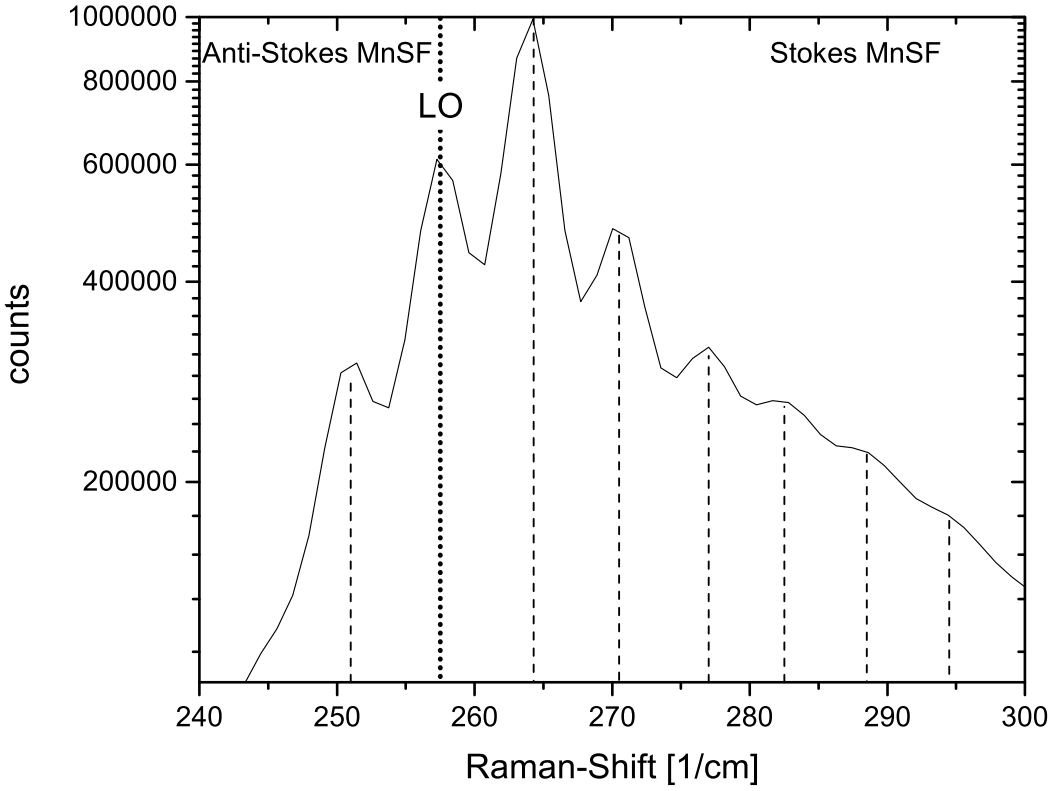

Figure 6.3: Spectrum of sample BD-95 in (σ, π) configuration at $B = 7\,\mathrm{T}$ and excitation energy $E_{exc} = 2.8131\,\mathrm{eV}$. Additional to the LO phonon at $\tilde{\nu} = 257\,\mathrm{cm}^{-1}$ (marked by the dotted line), peaks of the combined LO and Stokes or anti-Stokes Mn spin flip process occur (marked by the dashed lines). The Stokes and anti-Stokes side is denoted with respect to the LO phonon peak.

flip signal intensity which is overlapped by a non constant PL background (see Fig. 6.1 b)).

The Stokes to anti-Stokes ratio is shown as an inset in Fig. 6.2, ranging between nine and 92. The Boltzmann statistics enables the estimation of the Mn spin temperature, which yields $T_{Mn} = 1.9\,\mathrm{K}$ to $3.7\,\mathrm{K}$. Considering a bath temperature of $T = 1.5\,\mathrm{K}$, the obtained higher Mn spin temperature can be explained by the heating of the spin system due to optical excitation and also the previously mentioned difficulties of an exact measurement of the anti-Stokes intensity [KYK+01].

6.2 Resonant Raman spectroscopy of LO-assisted Mn spin flip

Fig. 6.3 shows a spectrum of sample BD-95, with an excitation energy $E_{exc} = 2.8131\,\text{eV}$, which corresponds to an energy increase by 31.8 meV compared to the measurement shown in Fig. 6.1. This energy increase equals the LO phonon energy. Therefore, the absolute energy position of the scattered photon, after a Mn spin flip and the additional excitation of an LO phonon, is equal to the scattered photon energy of the direct Mn spin flip signal. Additional to the LO phonon peak at $257\,\text{cm}^{-1}$, multiple satellite peaks at the high and low energy side of the LO phonon appear. These satellite peaks are separated equidistantly by $\tilde{\nu} = 6\,\text{cm}^{-1}$, indicating a sum process of the excitation of an LO phonon and up to six multiple Mn spin flips. The intensity of the LO peak is much weaker than the intensity of the Rayleigh scattered light and therefore, it is possible to detect the Stokes and anti-Stokes side simultaneously. Furthermore, the intensity of the LO and Stokes Mn spin flip sum process exceeds the intensity of the LO signal. When the wave vector of the incident and scattered photon is perpendicular to the (001) lattice plane, and the incident photon is polarized in (110) and the scattered photon in $(1\bar{1}0)$, which was the chosen experimental condition, the intensity of the LO related Raman signal is suppressed, according to Raman selection rules.
The broad background peak is assigned to PL transition no. 5 (|CB, -1/2 ⟩ to |VB, 1/2 ⟩). For a more detailed explanation of this assignment, see chapter 4.

6.2.1 B-field dependent development of the LO-assisted Mn spin flip

The B-field dependence of the Mn spin flip centered at the LO for the doped sample BD-274 is plotted in Fig. 6.4 a) for B-fields from 3 T to 7 T. The separation of the Stokes and anti-Stokes peak from the LO phonon can be observed for $B \geq 3\,\text{T}$, where a broad structure of three partially overlapping peaks appears. For lower magnetic fields, the spectral resolution of the experimental setup is not sufficient to resolve the individual peaks. Hence, only measurements for $B \geq 3\,\text{T}$ are presented and utilized for the further analysis. An increasing B-field leads to an in- and decreasing Raman-Shift of the Stokes and anti-Stokes

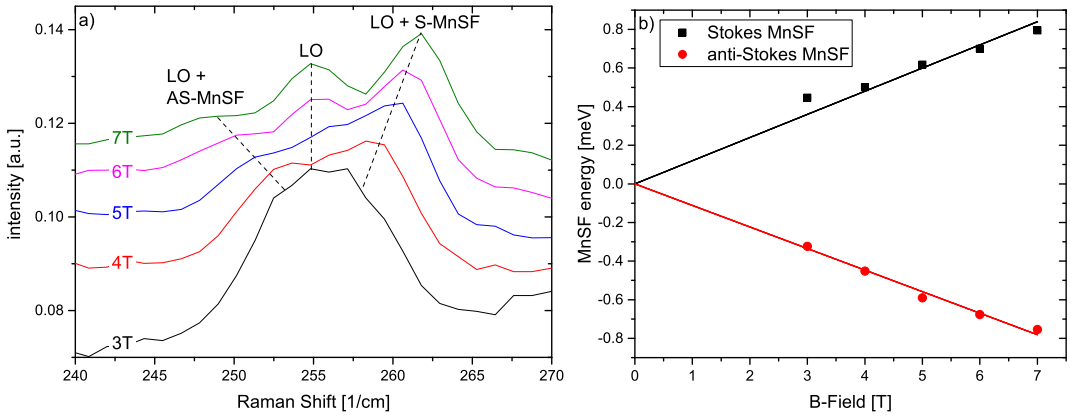

Figure 6.4: B-field dependence of the combined LO and Stokes or anti-Stokes Mn spin flip process (LO + S-MnSF, LO + AS-MnSF), spectra of sample BD-274, for B from 3 T to 7 T are shown in a).The dashed lines are guides for the eyes. b) Resulting peak positions relative to the LO peak, obtained by Gaussian fits of the spectra in a). The lines are linear fits to the data points.

spin flip peak, respectively. For each measured B-field, the three observed peaks between $\tilde{\nu} = 240\,\mathrm{cm}^{-1}$ and $270\,\mathrm{cm}^{-1}$ are fitted by three Gaussians. The obtained maximum positions allow the evaluation of the Mn spin flip energy, by determination of the energy differences between the measured LO peak and the sum processes of the LO phonon and the Stokes or anti-Stokes Mn spin flip. The B-field dependence of these energy differences is shown in Fig. 6.4 b). The resulting data points are fitted by linear functions. The ordinate of the linear fit is set to zero at $B = 0\,\mathrm{T}$, since no splitting of the Mn levels is expected [see Eq. (2.22)]. The resulting linear fits are plotted in Fig. 6.4 b), which yield a slope m of (0.120 ± 0.004) meV/T and (0.112 ± 0.002) meV/T for the Stokes and anti-Stokes signal, respectively. Averaging the absolute values of these two slopes gives $\tilde{m} = (0.116 \pm 0.002)$ meV/T and according to Eq. (2.22) a g-factor of $g_{Mn} = 2.00 \pm 0.03$.

6.2.2 Influence of the n-doping concentration on the LO-assisted Mn spin flip

In Fig. 6.5 two Raman spectra of the LO-assisted Mn spin flip process of the undoped sample and the sample with a doping concentration of $n = 4.2{\cdot}10^{17}\mathrm{cm}^{-3}$ are plotted. The excitation energy is $E_{exc} = 2.8131\,\mathrm{eV}$ and $E_{exc} = 2.8132\,\mathrm{eV}$ for the undoped and doped sample, respectively. The difference of the excitation energy is 0.1 meV and thus this small the difference in excitation energy has

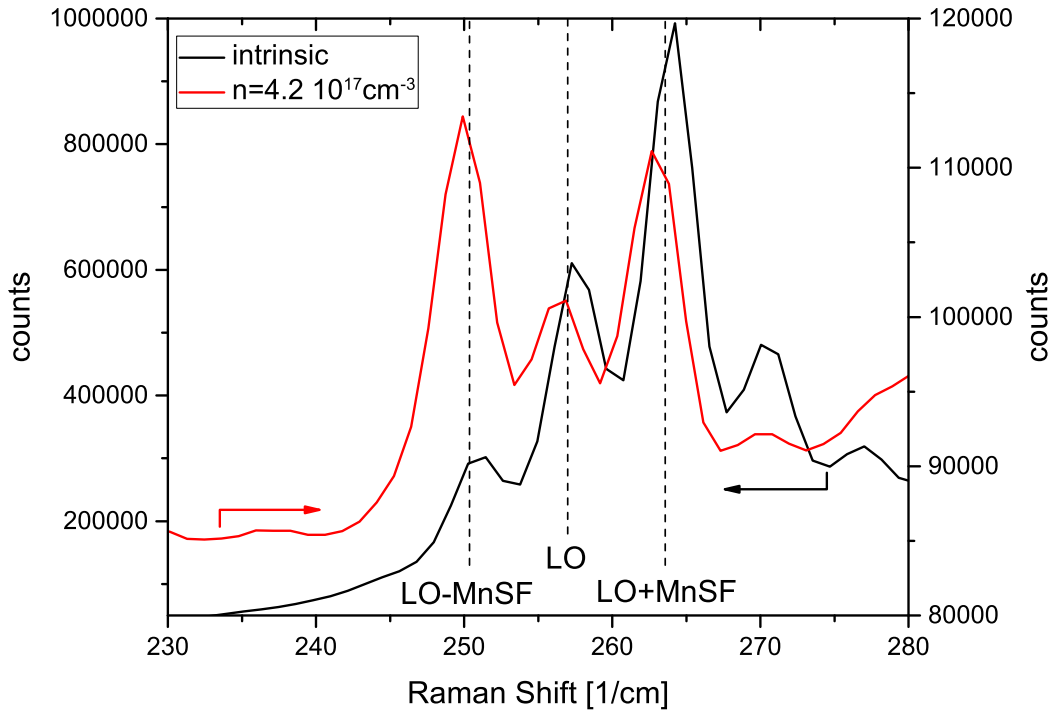

Figure 6.5: LO-assisted Mn spin flip spectra in (σ, π) configuration of the undoped sample BD-95 (black) and BD-230 ($n = 4.2{\cdot}10^{17}$ cm^{-3}) (red) at $B = 7$ T.

no noticeable influence for the comparison of the two spectra. For the doped sample, the multiple Mn spin flips almost disappear and only the single Stokes and anti-Stokes peaks are remaining. This is explained as follows: The Mn spin flip is caused by isolated Mn ions, i.e. Mn ions without nearest neighboring Mn ions. At Mn concentrations of $x = 0.05$, almost 50% of the Mn ions form pairs or even larger clusters, which are inactive for the Mn spin flip. The remaining single Mn ions can interact with donor electrons, causing a randomization of the Mn spin orientation. Thus, the Mn ions which are in the vicinity of a Cl-donor create highly randomized Raman-Shifts, instead of a sharp line. Consequently only single Mn ions, which are located between Cl-donors can produce a sharp Raman signal. The n-doping concentration $n = 4.2{\cdot}10^{17}$cm^{-3} of sample BD-230 is close to the metal-insulator transition, which reduces the number of these isolated Mn ions. Therefore, the probability of multiple Mn spin flips is drastically reduced, explaining the observation that only single Stokes and anti-Stokes Mn spin flips are detected for sample BD-230.

Furthermore, the anti-Stokes peak intensity slightly exceeds the intensity of the Stokes peak for sample BD-230. This effect is pronounced for all n-doped

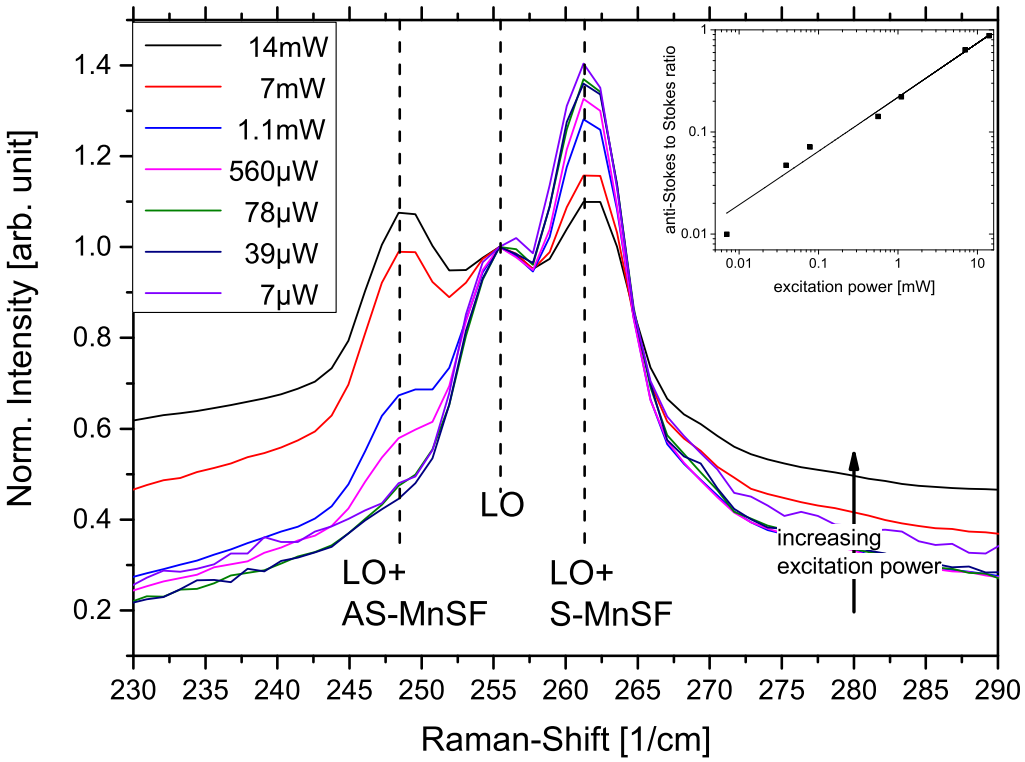

Figure 6.6: Power dependence of the LO-assisted Mn spin flip at B=7 T of sample BD-229. The inset shows the anti-Stokes to Stokes intensity ratio versus the excitation power, in a log-log scale. The line is a fit to the data points.

samples, with concentrations close to the metal-insulator transition. Therefore, experimental results of samples of this type are presented and discussed in the following section.

6.2.3 Excitation power dependence of the Stokes and anti-Stokes LO-assisted Mn spin flip

The optical excitation can increase the Mn spin temperature and consequently, a change of the Stokes and anti-Stokes intensities for varying excitation powers could occur. To analyze this effect, spectra taken at different excitation powers are presented in this section. It is noted that the results for the direct Mn spin flip are not shown, because even at the highest experimentally achievable excitation power, only a weak anti-Stokes peak occurs, which quickly vanishes at a lower excitation power. The observed spectra of the LO-assisted spin flip for

an excitation energy of $E_{exc} = 2.8092\,\text{eV}$ and powers between $P_{exc} = 7\ \mu\text{W}$ and 14 mW, of sample BD-229 are plotted in Fig. 6.6. The intensity scale of each spectrum is normalized to its LO phonon intensity. It can be seen, that the excitation power has a direct influence on the Stokes and also on the anti-Stokes peak intensity. With increasing power, the Stokes Mn spin flip peak decreases, whereas simultaneously the anti-Stokes peak is enhanced. This is explained by a possible heating of the Mn spin system caused by optical injection of hot electrons [KYK$^+$01]. The hot electrons interact with the Mn ions, which leads to larger quantity of excited Mn ions and thus, resulting in a higher intensity of the anti-Stokes signal. Consequently, less Mn ions are in their ground state, which can attribute to the Stokes process intensity. Therefore, a useful measure to analyze this heating effect is the anti-Stokes to Stokes intensity ratio. For the spectra shown in Fig. 6.6, the corresponding anti-Stokes to Stokes ratios versus the excitation power P_{exc} are shown as an inset in a log-log scale. The ratio increases with increasing excitation power and a more careful analysis reveals a linear trend of the ratio in the log-log scale, fitted by $\frac{I_{anti-Stokes}}{I_{Stokes}} = A{\cdot}(P_{exc})^B$. The resulting fit parameters are $A = 0.05$ and $B = 0.53$ and the fit nicely matches the experimental results, as can be seen in the inset of Fig. 6.6. Therefore, an extrapolation of the fit seems reasonable, which would suggest that the ratio could exceed the value of one at an excitation power of $P_{exc} = 17.5\,\text{mW}$. It will be shown in the next section that the anti-Stokes to Stokes ratio not only depends on the excitation power, but even more drastically on the excitation photon energy. For certain experimental parameters, an inversion of the anti-Stokes to Stokes intensities, i.e. anti-Stokes intensity larger than Stokes intensity, is indeed achievable. This behavior cannot simply be explained by an increase of the Mn spin temperature.

6.2.4 Resonant Raman measurements of the LO-assisted Mn spin flip

For further studies the resonance profile of the LO-assisted Mn spin flip process was measured and analyzed. Here, the excitation energy E_{exc} is varied from 2.803 eV to 2.831 eV while the excitation power was kept constant at $P_{exc} = 35\,\text{mW}$. The observed Stokes and anti-Stokes peaks are fitted each by a Gaussian curve and the resulting fit areas are used as the relevant mea-

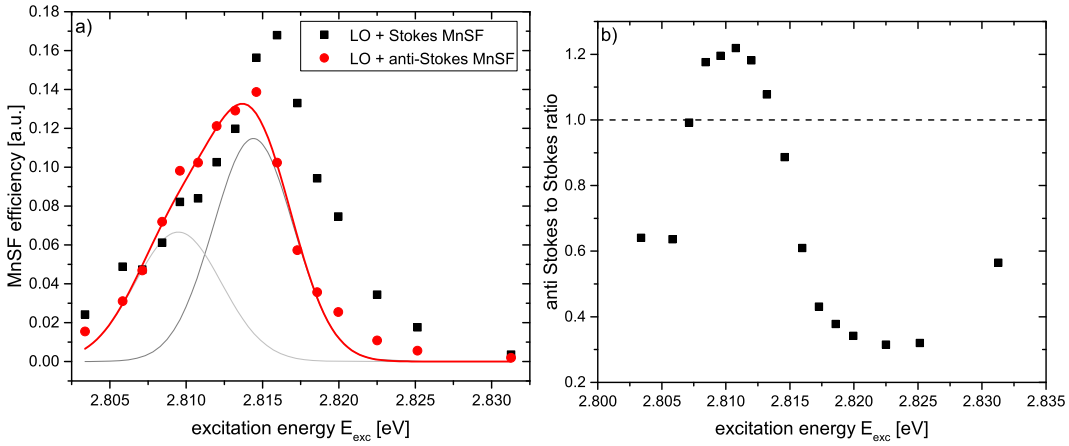

Figure 6.7: a) Resonance profile of the LO-assisted Stokes and anti-Stokes Mn spin flip of sample BD-230 at $B = 7\,\mathrm{T}$. The red curve is the fit result of the anti-Stokes resonance profile, consisting of two Gaussian curves, plotted in dark and light gray. b) The ratio of the anti-Stokes to Stokes intensities of the data shown in a). The dashed line marks the ratio one.

sure of the spin flip scattering efficiency. The obtained Mn spin flip efficiencies for the Stokes and anti-Stokes process are plotted versus the excitation energy E_{exc} in Fig. 6.7. Both, the LO-assisted Stokes and anti-Stokes Mn spin flip intensities show a clear dependence on the excitation energy. The highest absolute intensity occurs for the LO-assisted Stokes Mn spin flip at an excitation energy of $E_{exc} = 2.816\,\mathrm{eV}$ and for the anti-Stokes process at $E_{exc} = 2.815\,\mathrm{eV}$. Remarkably, between E_{exc}=2.808 eV and $E_{exc} = 2.813\,\mathrm{eV}$, the anti-Stokes surpasses the Stokes intensity. The fact that multiple data points of the anti-Stokes scattering efficiency are above the corresponding Stokes scattering efficiency indicates that the observation is not caused by a measurement errors or statistical fluctuations. Moreover, the asymmetric shape of the anti-Stokes resonance profile indicates that contributions with two different intermediate states possibly cause the enhancement of the anti-Stokes process. Therefore, two Gaussian curves are fitted to the anti-Stokes resonance profile, which are also shown in Fig. 6.7. The fits yield a maximum at $E_{res,1} = (2.809 \pm 0.003)$ eV and $E_{res,2} = (2.814 \pm 0.002)$ eV and half-width values of $\mathrm{FWHM}_{res,1} = (6.7 \pm 3.2)$ meV and $\mathrm{FWHM}_{res,2} = (6.2 \pm 1.2)$ meV. Due to the relatively broad partially overlapping Gaussian curves, the exact determination of the maximum of the individual resonance contributions must be treated with some caution.

Assuming that the additional resonance only contributes to the anti-Stokes in-

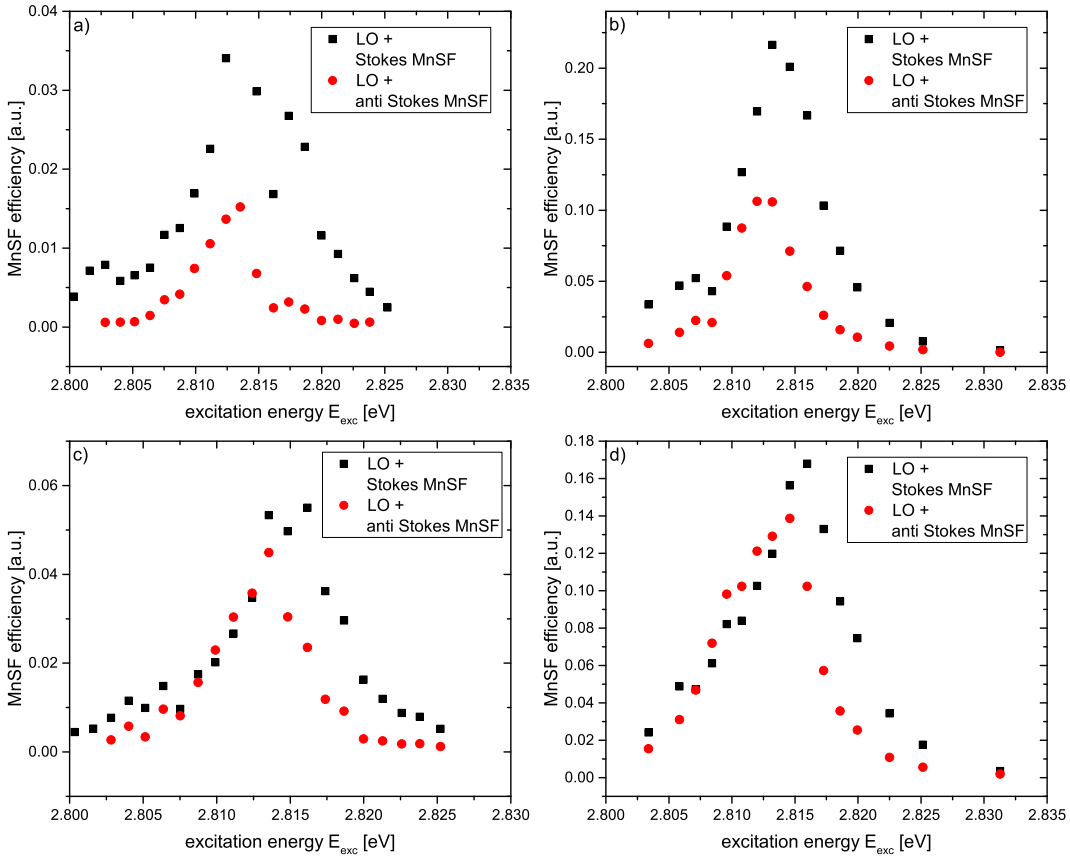

Figure 6.8: Resonance profiles of the LO-assisted Stokes and anti-Stokes Mn spin flip of sample BD-230 at $B = 7\,\mathrm{T}$. a) to d) excitation power $P_{exc} = 0.8\,\mathrm{mW}$, 2 mW, 8 mW and 35 mW

tensity, the ratio of the anti-Stokes to Stokes process is instead used as a more accurate measure to analyze this second anti-Stokes Mn spin flip resonance. This ratio for the previously shown results is plotted in Fig. 6.7 b). The anti-Stokes to Stokes intensity ratios range from 0.32 to 1.21, with the maximum at an excitation energy of $E_{exc} = 2.8107\,\mathrm{eV}$. Here, it becomes even more apparent that the anti-Stokes intensity is larger than the Stokes intensity, indicated by the dashed line at a constant ratio of one. The ratio curve forms a single peak-like structure and does not randomly fluctuate. This verifies that the ratio of the anti-Stokes to Stokes intensity can be used as a suitable parameter to study the underlying resonance process.

As shown before, the excitation power and also the excitation energy influences the intensity of the Stokes and anti-Stokes peak. For this reason, a variation of both parameters was performed. The resulting power dependent resonance profiles of the LO-assisted Stokes and anti-Stokes Mn spin flip in-

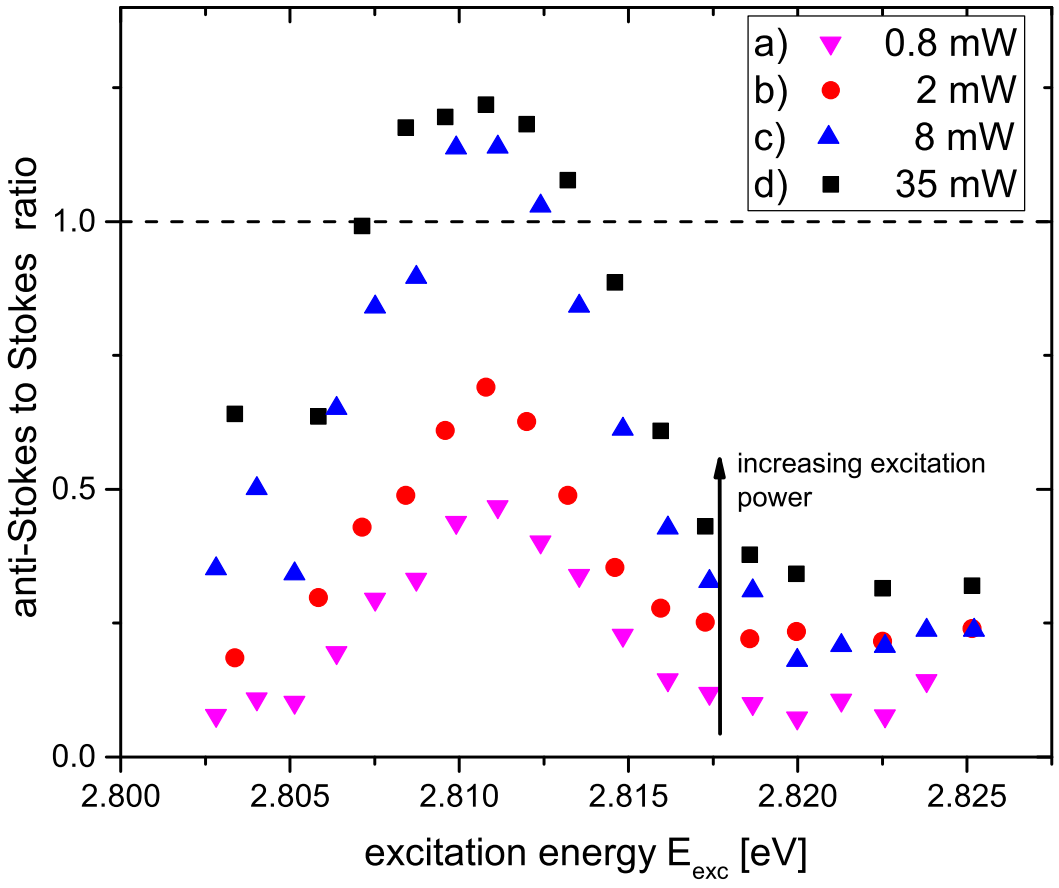

Figure 6.9: Excitation power dependence of the anti-Stokes to Stokes ratio of the LO-assisted Mn spin flip process shown in Fig. 6.8 a) to d). The dashed horizontal line indicates the ratio one.

tensities of sample BD-230 for excitation powers $P_{exc} = 0.8\,\mathrm{mW}$, $2\,\mathrm{mW}$, $8\,\mathrm{mW}$ and $35\,\mathrm{mW}$ are shown in Fig. 6.8 a) to d). For all excitation powers a distinct resonance enhancement of the Stokes and anti-Stokes signal occurs. The absolute maxima of the Stokes and the anti-Stokes Mn spin flip process arise for excitation energies between $2.812\,\mathrm{eV}$ and $2.816\,\mathrm{eV}$. The positions of the maxima do not seem to be influenced by the excitation power, however with increasing excitation power, the Stokes and anti-Stokes intensities rise for all excitation energies. This trend is more pronounced for the anti-Stokes process. Moreover, the anti-Stokes resonance profile becomes more asymmetric and the anti-Stokes intensity exceeds the Stokes intensity for excitation energies between $E_{exc} = 2.810\,\mathrm{eV}$ and $2.812\,\mathrm{eV}$ already at $P_{exc} = 8\,\mathrm{mW}$. This proves that the additional contribution to the LO-assisted anti-Stokes Mn spin flip resonance depends on the excitation power.

For a more detailed analysis, the ratio of the anti-Stokes to Stokes intensity at all four excitation powers is investigated. The corresponding results are plotted in Fig. 6.9. A peak near $E_{exc} = 2.8106\,\text{eV}$ is clearly visible at all excitation powers. Furthermore, as expected, this ratio increases with higher excitation power. For each dataset, a Gaussian fit has been applied to the data points. Comparing the fit results for the lowest and highest excitation power reveals that the peak position shifts only slightly from $E_{res,1} = 2.8109\,\text{eV}$ to $2.8104\,\text{eV}$. As shown in section 4.3, the optical excitation can increase the temperature of the Mn system. This shifts the splitting of the electronic energy levels in an external magnetic field and consequently also the energy position of the resonance process. Hence the obtained shift $\Delta E = 0.5\,\text{meV}$ can be used to determine the transition, which is responsible the additional resonance of the anti-Stokes Mn spin flip process.

At an external magnetic field $B = 7\,\text{T}$, the by far most intense PL is the transition no. 1 of the (X^0) (see chapter 4). Varying excitation power shifts the energy position of this PL. At $P_{exc,1} = 0.8\,\text{mW}$ the PL is detected at $E_{PL1} = 2.7586\,\text{eV}$ and at $P_{exc,2} = 35\,\text{mW}$ at $E_{PL1} = 2.7644\,\text{eV}$ which implies an energy shift of $\Delta E = 5.8\,\text{meV}$. The trend of PL no. 1 is an order of magnitude larger with opposite sign, compared to the spin flip resonance shift. Hence transition no. 1 is excluded to be involved in the additional anti-Stokes Mn spin flip resonance. The B-field induced splitting of the VB band in (Zn,Mn)Se is five times larger than the corresponding CB splitting, i.e. $N_0\beta = -5 \cdot N_0\alpha$. This allows the calculation of the expected shift caused by the heating of the Mn spin system of all other optical transitions with respect to PL no. 1. First, transitions no. 2 and 5 shift to higher energies with increasing spin temperature and can therefore not be involved in the additional resonance and are not subject of a further analysis. The energy shifts of transition no. 1 and the remaining three transitions no. 3, 4, and 6 can be calculated by modifying Eqs. (1.28) and (1.29) and amount to:

$$\Delta E_{PL1}(B,\Delta T) = \frac{1}{2}(N_0\alpha - N_0\beta)x_{eff}\cdot\Delta\langle S_z(B,\Delta T)\rangle = \quad 3\cdot\gamma(B,\Delta T) \tag{6.1}$$

$$\Delta E_{PL3}(B,\Delta T) = (\frac{1}{2}N_0\alpha + \frac{1}{6}N_0\beta)x_{eff}\cdot\Delta\langle S_z(B,\Delta T)\rangle = \quad -\frac{1}{3}\cdot\gamma(B,\Delta T) \tag{6.2}$$

$$\Delta E_{PL4}(B,\Delta T) = -\frac{1}{2}(N_0\alpha - N_0\beta)x_{eff}\cdot\Delta\langle S_z(B,\Delta T)\rangle = \quad -3\cdot\gamma(B,\Delta T) \tag{6.3}$$

$$\Delta E_{PL6}(B,\Delta T) = -(\frac{1}{2}N_0\alpha - \frac{1}{6}N_0\beta)x_{eff}\cdot\Delta\langle S_z(B,\Delta T)\rangle = \quad -\frac{4}{3}\cdot\gamma(B,\Delta T) \tag{6.4}$$

with

$$\gamma(B,\Delta T) = N_0\alpha\cdot x_{eff}\cdot\Delta\langle S_z(B,\Delta T)\rangle \tag{6.5}$$

$$\Delta\langle S_z(B,\Delta T)\rangle = \langle S_z(B,T_1)\rangle - \langle S_z(B,T_2) \tag{6.6}$$

and

$$N_0\alpha = -\frac{N_0\beta}{5}\ \text{[for (Zn, Mn)Se]} \tag{6.7}$$

Here, T_1 and T_2 are the two spin temperatures at the two excitation powers P_{exc}. The values of T_1 as well as T_2 are identical for all transitions. This allows the substitution of Eq. (6.1) into the Eqs. (6.2), (6.3) and (6.4) to give the following relations:

$$\Delta E_{PL3}(B,\Delta T) = -\frac{1}{9}\cdot\Delta E_{PL1}(B,\Delta T) \tag{6.8}$$

$$\Delta E_{PL4}(B,\Delta T) = -\Delta E_{PL1}(B,\Delta T) \tag{6.9}$$

$$\Delta E_{PL6}(B,\Delta T) = -\frac{4}{9}\cdot\Delta E_{PL1}(B,\Delta T) \tag{6.10}$$

As shown before, the energy shift of transition no. 1 equals $\Delta E_{PL1}(7T,\Delta T) = -5.8\,\text{meV}$ for the measurements at $P_{exc} = 0.8\,\text{mW}$ and $P_{exc} = 35\,\text{mW}$. Hence, the calculated shifts of the other three transitions are $\Delta E_{PL3}(B,\Delta T) = 0.6\,\text{meV}$, $\Delta E_{PL4}(B,\Delta T) = 5.8\,\text{meV}$ and $\Delta E_{PL6}(B,\Delta T) = 2.6\,\text{meV}$.

The calculated shift of transition no. 3 (|CB, -1/2⟩ to |VB, 1/2 ⟩) almost

coincides with the observed shift of the resonance position with increasing excitation power. This is an indicator that transition no. 3 is relevant for in the additional LO-assisted anti-Stokes resonance contribution.

6.3 Model of the direct and LO-assisted anti-Stokes Mn spin flip resonance

To give a short summary of the results, presented in the previous section, the direct Mn spin flip shows a resonance profile for the Stokes and also the anti-Stokes process, consisting of one resonance contribution. For the whole investigated excitation energy range, the anti-Stokes peak intensity is up to 100 times weaker than the corresponding Stokes peak. In contrast, the LO-assisted anti-Stokes Mn spin flip peak intensity is similar to the Stokes peak intensity. Moreover, the resonance profile of sum process of the LO phonon and the anti-Stokes Mn spin flip consists of two partially overlapping contributions.
The first contribution of the LO-assisted Mn spin flip resonance profile is shifted by exactly one LO phonon energy compared to the position of the direct Mn spin flip resonance and applies for the LO-assisted Stokes as well as anti-Stokes MnSF. The second contribution mainly affects the LO-assisted anti-Stokes Mn spin flip process and shows a distinct dependence on the excitation power. Furthermore, comparing the energy shift of this contribution, induced by the heating of the Mn spin system, indicates that the electronic CB-VB transition no. 3 between $|\text{VB}, -1/2\rangle$ and $|\text{CB}, -1/2\rangle$ is the cause of the second resonance contribution. In the following sections, the above mentioned observations are explained.

6.3.1 Direct Mn spin flip resonance process

In this section, a model for the resonance of the direct Mn spin flip process is discussed. The insights obtained by the model are used as a foundation for the discussion of the LO-assisted Mn spin flip in section 6.3.2.
In the exchange-induced sub-process of the paramagnetic spin flip Raman process, a Mn spin flip with $\Delta S_{Mn} = \pm 1$ induces a electron spin flip with

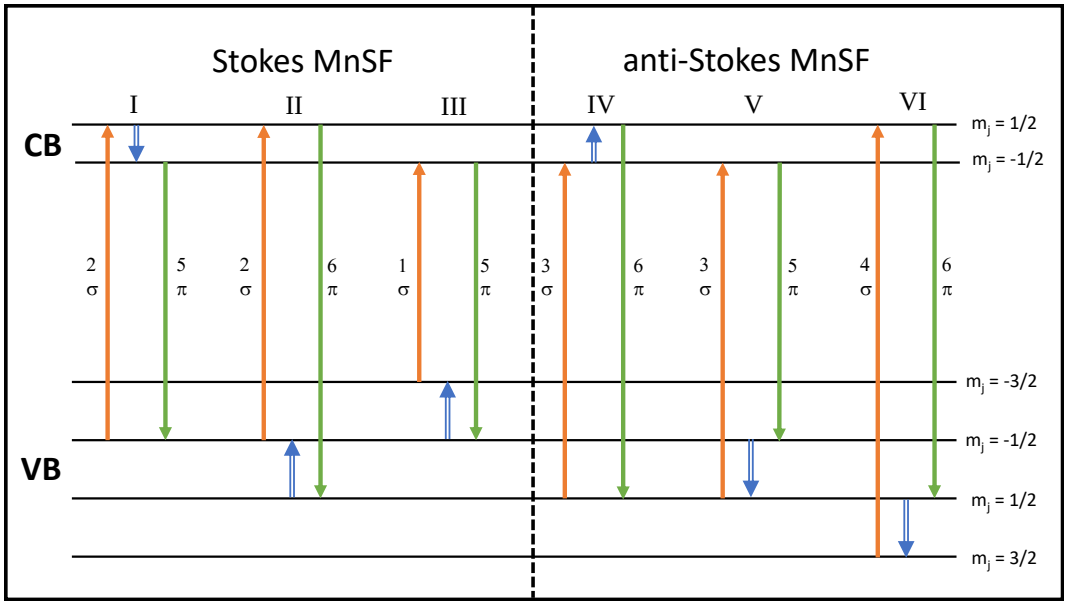

Figure 6.10: Raman mechanism for the Mn spin flip. The conduction (CB) and valence band (VB) are labeled by the electron quantum number m_j. The single arrows indicate virtual electron dipole transitions, with their corresponding numbers as referred in text and polarization σ (red) or π (green), double arrows (blue) refer to transitions induced by the electron-Mn^{2+} exchange interaction. For classification of the three possible Stokes and three anti-Stokes MnSF processes, they are labeled with roman numerals I to VI.

$\Delta S_e = \mp 1$. This leads to the possible paramagnetic resonance Raman scattering processes in (σ, π) Voigt configuration, as visualized in Fig. 6.10. At commonly achievable B-fields it is not possible to achieve an incoming and outgoing resonance simultaneously, because the energy splitting of the electronic spin levels within the VB and CB in (Zn,Mn)Se for $B = 7\,\mathrm{T}$ is more than 15 times larger than the splitting energy of the Mn spin levels. Although the Voigt configuration allows no distinction between a $\Delta m_j = +1$ and $\Delta m_j = -1$ optical transition, the fact that the Stokes and anti-Stokes process are in resonance at almost the identical excitation energy can be used to determine the underlying resonance process. For the complete Raman process, which consists of the excitation step, the Mn spin flip combined with an electron or hole spin flip, and the electron hole recombination, Δm_j has to be zero, when a change of the photon spin $\Delta S = \pm 1$ is involved. Consequently, for a Stokes Mn spin flip with $\Delta m_{j,Mn} = 1$ a spin flip of the electron or hole with $\Delta m_{j,(e,h)} = -1$ is induced in the exchange-interaction step. For the anti-Stokes process, the algebraic sign is reversed. If the sought resonance is an incoming resonance,

in (σ, π) Voigt configuration the identical incoming resonance cannot simultaneously enhance the Stokes and anti-Stokes Mn spin flip process. This is also seen in Fig. 6.10, where none of the optical excitation step of the Stokes MnSF process is identical to the anti-Stokes MnSF excitation steps.
On the other hand, an outgoing resonance for the Stokes and anti-Stokes Mn spin flip process can be achieved simultaneously in (σ, π) Voigt configuration. Comparing the scattered photon energy of transition no. 5 ($|$CB,-1/2$\rangle$ to $|$VB,-1/2$\rangle$ state) with the energy $E_{PL5} = 2.781\,\mathrm{eV}$ at $B = 7\,\mathrm{T}$ and $T = 1.5\,\mathrm{K}$, with the energy position of the direct Mn spin flip resonance at $E_{res} = 2.784\,\mathrm{eV}$, indicates that this transition is the cause of the enhancement of the Mn spin flip scattering efficiency. Among the visualized processes shown in Fig. 6.10, only Stokes processes I and III and the anti-Stokes process VI include the relevant optical transition no. 5.
To identify, which of the two Stokes processes primarily contributes to the resonance enhancement at an incident photon energy of $E_{res} = 2.784\,\mathrm{eV}$, it is useful to consider that incoming and outgoing resonance conditions are typically not achieved simultaneously for the paramagnetic process. Consequently, one of the excited states in the total Raman process must be assumed to be a virtual state. Its lifetime is inversely proportional to the energy difference to its corresponding eigenstate. In (Zn,Mn)Se the total VB levels splitting is five times the splitting of the CB, e.g. for $Zn_{0.95}Mn_{0.05}Se$ at $B = 7\,\mathrm{T}$, the separation of the individual VB levels is 25 meV compared to the 15 meV of the CB splitting. As a consequence the Stokes Mn spin flip process I in Fig. 6.10, which involves an electron spin flip, is more likely than the process III, which includes a hole spin flip, due to the smaller energy mismatch in the former one between the virtual state and the eigenstate involved in the total Raman scattering process. Thus the Stokes process I is identified as the Raman scattering mechanism causing the enhancement of the Stokes Mn spin flip at an excitation energy of $E_{res} = 2.784\,\mathrm{eV}$.

6.3.2 LO-assisted Mn spin flip resonance process

For a qualitative analysis of the LO-assisted Mn spin flip process, it is reasonable to start with a comparison of this process with the direct Mn spin flip process. The LO-assisted anti-Stokes Mn spin flip resonance profile shows two con-

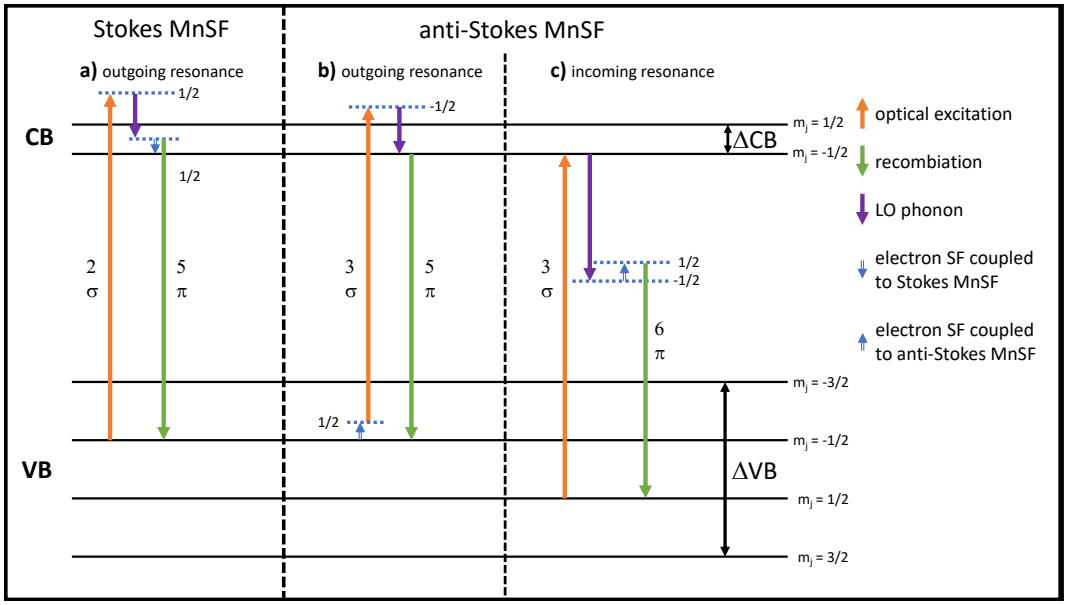

Figure 6.11: Raman mechanisms for the LO-assisted Mn spin flip; only those transitions are shown which are relevant for the observed resonances: a) shows a scheme of the outgoing Stokes MnSF resonance, b) of the outgoing anti-Stokes MnSF resonance and c) of the incoming anti-Stokes MnSF resonance. The single arrows indicate optical electron dipole transitions, with their corresponding numbers as referred in text and polarization σ (red) or π (green), the dashed blue horizontal lines are virtual states and the black solid lines eigenstates labeled by the electronic quantum number m_j. The blue double arrows refer to transitions induced by the electron-Mn^{2+} exchange interaction.

tributions, at about $E_{res,1} = (2.809 \pm 0.003)$ eV and $E_{res,2} = (2.814 \pm 0.002)$ eV (see Fig. 6.7). Calculating the energy difference $E_{res,2}$ and the resonance position of the direct Mn spin flip process at $E_{res} = (2.784 \pm 0.003)$ eV, yields $\Delta E = (30 \pm 4)$ meV, which coincides within the limits of accuracy of the measurements with the LO energy of $E_{LO} = 32$ meV. Therefore, the second contribution to the LO-assisted Mn spin flip resonance is determined as the process, which was identified in the previouse section as the resonance of the direct Mn spin flip process, here in this case in comibation with the additional excitation of an LO phonon. The corresponding transitions for the LO-assisted Stokes and anti-Stokes process are visualized in Fig. 6.11 and labeled as outgoing resonances [processes a) and b)].

The contribution at $E_{res,1} = 2.809$ eV mainly affects the anti-Stokes process, as observed in the analysis of the anti-Stokes to Stokes intensity ratio. This result indicates that the resonance responsible for the enhancement of the anti-Stokes

Mn spin flip signal is presumably an incoming resonance. As explained previously, an incoming resonance in (σ,π) configuration can either be achieved for the Stokes or the anti-Stokes process but not for both simultaneously.
A proposed incoming resonance process of the LO-assisted anti-Stokes Mn spin flip is shown as process c) in Fig. 6.11. It consists of a σ polarized optical excitation from the |VB, 1/2⟩ to the |CB, -1/2⟩ state (transition no. 3), the creation of an LO phonon and the anti-Stokes Mn spin flip with $\Delta m_{j,Mn} = -1$ of the Mn state and consequently a $\Delta m_{j,e} = +1$ flip of the electron system and the recombination step, from an s-like virtual |CB, 1/2⟩ state to the |VB, 1/2⟩ state under emission of a π-polarized photon.
To verify this proposed incoming resonance, the expected energy of the incoming photon can be expressed with respect to PL no 5. as:

$$E_{res,1}(B,T) = E_{PL3}(B,T) = E_{PL5}(B,T) + \frac{1}{3}\Delta VB(B,T) \tag{6.11}$$

with the total energy splitting of the valence band $\Delta VB(B,T)$. The excitation energy for the outgoing anti-Stokes resonance, shown in Fig. 6.11 can be calculated as follows:

$$E_{res,2}(B,T) = E_{PL5}(B,T) + E_{LO} - E_{AS\text{-}MnSF}(B) \tag{6.12}$$

with $E_{LO} = 32\,\text{meV}$ is the LO phonon energy and $E_{AS\text{-}MnSF}(B)$ is the B-field dependent energy of the anti-Stokes Mn spin flip..
The expected energy separation $\Delta E(B,T)_{res,12}$ between $E_{res,1}(B,T)$ and $E_{res,2}(B,T)$ can be determined as:

$$\begin{aligned}\Delta E(B,T)_{res,12} &= E_{res,1}(B,T) - E_{res,2}(B,T) \\ &= \frac{1}{3}\Delta VB(B,T) - E_{LO} + E_{AS\text{-}MnSF}(B)\end{aligned} \tag{6.13}$$

In this form, $\Delta E(B,T)_{res,12}$ is independent of the absolute energy positions of the individual optical transitions. For the investigated sample, with a Mn content of $x = 0.05$, ΔVB(7T, 1.5K) equals 75 meV (see chapter 4), resulting in a ΔE(7T, 1.5K) $= -6.2\,\text{meV}$. This value is almost identical to the experimentally observed separation of the two resonance contributions $\Delta E_{res,12} = 5\,\text{meV}$. This indicates that the proposed incoming resonance is causing the additional enhancement of the LO-assisted anti-Stokes Mn spin flip at an excitation en-

ergy of $E_{exc} = 2.809\,\mathrm{eV}$.
Additionally, the optical dipole transition no. 3 shifts according to Eq. (6.8) to higher energies with increasing B/T. The expected shift due to the heating of the Mn spin system of transition no. 3 was calculated previously. The experimental results of the LO-assisted anti-Stokes Mn spin flip indicate, that transition no. 3 is involved in the additional resonance of the LO-assisted anti-Stokes Mn spin flip process. In conclusion, the at first sight astonishing observation that the anti-Stokes to stokes intensity ratio exceeding one and the concomitant modified anti-Stokes resonance profile can be explained by the Raman scattering mechanisms shown in Fig. 6.11, which considers the effect of an incoming and outgoing resonance on the LO-assisted anti-Stokes Mn spin flip process resonance profile and the fact that the incoming resonance only affects the anti-Stokes Mn spin flip process.

Zusammenfassung

Ziel der vorliegenden Dissertation war das Erlangen neuer Erkenntnisse zur Wechselwirkung der magnetischen Ionen und des Leitungsbandes von verdünnten magnetischen Halbleitern. Diese Interaktion bei magnetischen Halbleitern mit Ladungsträgerkonzentration nahe des Metall-Isolator Übergangs (metal-insulator transition MIT) in externen Magnetfeldern ist bisher kaum erforscht. Daher wurden Untersuchung n-dotierte $Zn_{1-x}Mn_xSe$:Cl Proben von der Gruppe von Herrn Dr. Hetterich, des "Karlsruher Institut für Technologie" (KIT), zur Verfügung gestellt. Das untersuchte Probenset enthält Donatorkonzentration zwischen nominell undotiert bis zu $n_{Cl} = 10^{18}$ cm^{-3} und Mangankonzentrationen zwischen $x = 0.01$ und $x = 0.07$. Aufgrund der Zielsetzung dieser Dissertation wurde bei der Herstellung insbesondere darauf geachtet, Proben mit Ladungsträgerkonzentration nahe des MIT bei $n_{crit} = 7{\cdot}10^{17}$ cm^{-3} von ZnSe zu erhalten.

Als Analysetechnik wurde die resonante Spin Flip Raman-Spektroskopie bei einem externen Magnetfeld zwischen 1 T und 7 T und einer Temperatur von 1,5 K angewandt. Aufgrund der niedrigen Temperatur richten sich die Spins der Mangan-Ionen bereits bei einem schwachen externen Magnetfeld parallel zu diesem aus. Durch die entstehende Magnetisierung des Materials werden die Aufspaltungen der Zustände mit entgegengesetzten Spins sowohl im Valenz- als auch im Leitungsband verstärkt. Dies ist als "giant-Zeeman effect" bekannt.

In dieser Arbeit wurde die Resonanz des Spin Flip Prozesses, d.h. die Signalerhöhung in Abhängigkeit der Anregungsenergie, als Indikator zur Bestimmung der Ladungsträgerzustandsdichte genutzt. Die gemessenen Resonanzprofile aller Proben zeigten dabei eine Struktur, welche aus sich zwei teilweise überlagernden Gaußkurven bestand. Die Analyse ergab, dass die Maxima der beiden Gaußkurven proben- und magnetfeldunabhängig um etwa 5 meV separiert sind, welche der Bindungsenergie des gebundenen Exzitons

(D^0, X) entspricht. Daher nutzt der elektronische Spin Flip Prozess das freie bzw. das gebundene Exziton als angeregten Zwischenzustand, welche separat resonant angesprochen werden können.
Mit steigendem Magnetfeld wurde eine deutliche Zunahme der Halbwertsbreite der Resonanzprofile beobachtet. Die detaillierte Analyse dieses Verhaltens zeigte, dass für alle Proben mit einer Dotierung unterhalb des Metall-Isolator-Übergangs, die Verbreiterung primär auf den Donor gebundenen Exzitonen Anteil der Resonanzkurve entfällt. Zur Deutung dieser Beobachtung wurde ein Modell entwickelt. Dieses beruht auf der grundlegenden Annahme einer räumlich statistisch Verteilung der Mangan-Ionen auf dem Gruppe-II Untergitter des ZnSe Kristalls, sowie der endlichen Ausdehnung der Exzitonen. Somit erfasst jedes einzelne Exziton eine individuelle Anzahl von Mangan-Ionen, was sich als lokale Mangankonzentration manifestiert. Diese lokale Mangankonzentration normalverteilt für ein Set von Exzitonen und deren Auswertung erlauben einen Rückschluss auf die Radien der Exzitonen. Die ermittelten Radien liegen probenabhängig zwischen 1,55 nm und 5,90 nm für das (D^0, X) und zwischen 2,09 nm und 11,5 nm für das ungebundene Exziton (X^0).
Zwei Trends für die (D^0, X) Radien konnten identifiziert werden. Sowohl mit steigender Ladungsträgerkonzentration als auch mit steigendem Mangangehalt nimmt der Radius der gebundenen Exzitonen ab. Es gelangte erstmalig die Bestimmung der (D^0, X) Radien mittels resonanter Spin Flip Raman-Spektroskopie und die Beobachtung des Verhaltens der (D^0, X) Radien in Abhängigkeit der Ladungsträgerkonzentration.
Die ermittelten (X^0) Radien sind für die Proben mit Ladungsträgerkonzentrationen unterhalb des Metall-Isolator-Übergangs im Vergleich zu den (D^0, X) Radien um einen Faktor von bis zu 5,9 größer. Diese Beobachtung lässt sich durch den ungebundenen Charakter der (X^0) erklären. Aufgrund dessen erfasst ein (X^0) während seiner Lebenszeit im Vergleich zu einem (D^0, X) einen räumlich ausgedehnteren Bereich des Kristalls. Dies reduziert den Einfluss der statistisch schwankenden lokalen Mangankonzentrationen auf die (X^0) Energiezustände, was zu einer schmaleren (X^0) Energieverteilung führt und mittels der Resonanzbreite des elektronischen Spin Flip Prozesses gemessen wurde. Zu betonen ist jedoch der ermittelte (X^0) Radius der hochdotierten Probe. Dieser Radius beträgt nur 2,09 nm und ist somit nur um einen Faktor von 1,3 größer als der (D^0, X) Radius dieser Probe. Als mögliche Ursache für diese Beobachtung könnte die Streuung der Exzitonen an freien Ladungsträgern gel-

ten, welche bei dieser Probe selbst bei niedrigen Temperaturen vorhanden sind. Dadurch wird die Lebensdauer der Exzitonen verringert, was deren erfasstes Volumen deutlich senkt und somit einem kleineren Exzitonenradius entspricht. Hierdurch konnte erstmalig mittels Raman-Spektroskopie solch eine Beobachtung gemacht werden.
Neben den Resonanzuntersuchungen des elektronischen Spin Flips wurde dessen Preakform im Ramanspektrum analysiert. Dabei wurde eine deutliche Asymmetrie des Signals beobachtet, sichtbar als Flanke zu niedrigeren Raman-Verschiebungen. Diese Asymmetrie ist am deutlichsten ausgeprägt, wenn der Prozess Spin Flips in der (D^0, X) Resonanz angeregt wird.
Zur Erklärung dieser Beobachtungen kann ebenfalls das eingeführte Modell angewandt werden. Anhand der Asymmetrie des resonant angeregten Spin Flip Signals konnten hiermit die Radien der (D^0, X) bestimmt werden. Bei externen Magnetfeldern zwischen 1,25 T und 7 T betragen die ermittelten Radien zwischen 2,38 nm und 2,75 nm. Diese Werte stimmen im Rahmen ihrer Fehler mit den ermittelten Radien, basierend auf den Messungen der Resonanzverbreiterung, überein.
Zusätzlich wurde die Asymmetrie bei unterschiedlichen Anregungsenergien sichtbar. Hierbei fiel auf, dass diese mit steigender Anregungsenergie abnimmt. Bei der höchsten Anregungsenergie, die eine Messung des elektronischen Spin Flips erlaubt, erhielt man hierbei einen Radius von 3,92 nm. Begründen lässt sich dies durch den Wechsel von dem (D^0, X) zum (X^0) dominierten Resonanzregime des Spin Flip Prozesses. Die in diesem Fall deutliche Abweichung gegenüber den Resonanzmessungen, welche einen Wert von 7 nm für den (X^0) Radius der untersuchten Probe ergab, kann primär auf die steigende Ungenauigkeit der Analysemethode bei stark abnehmender Asymmetrie zurückgeführt werden.
Desweiteren wurde zusätzlich zu den Beobachtungen des elektronischen Spin Flips, das Resonanzverhalten des Spin Flips der einzelnen Mn-Ionen in dieser Arbeit untersucht. Dies wurde sowohl für den direkten Mn Spin Flip Prozess, als auch den Summenprozesses aus einem longitudinal optischen Phonon und einem Mn Spin Flip durchgeführt. Jeweils eine Resonanz wurde sowohl für die direkten Stokes und anti-Stokes Prozesse, als auch für den Stokes Summenprozess beobachtet. Im Gegensatz hierzu besteht das Resonanzprofil des Summenprozesses, bei dem ein Anti-Stokes Mn Spin Flip involviert ist, aus zwei sich überlappenden Resonanzanteile. Eine genaue Analyse dieses Reso-

nanzprofils ergab, dass es bei (Zn,Mn)Se und den gewählten experimentellen Parametern möglich ist, sowohl eine eingehende als auch eine ausgehende Resonanz für diesen Summenprozess mit einer Energiedifferenz von wenigen meV zu erhalten. Die zusätzlich auftretende eingehende Resonanz konnte dabei dem optischen Übergang von dem m_j = 1/2 Valenzband- zum m_j = -1/2 Leitungsbandzustand zugeordnet werden. Die daraufhin folgende Anregung eines LO Phonons führt zu einer Reduzierung der Energie des gestreuten Photons. Dies erzeugt die beobachtete Überlagerung der Resonanzen, gemessen in der Energie der gestreuten Photonen. Hierdurch war es möglich, bei geeigneter Anregungsenergie und hoher Anregungsleistung eine Inversion der Anti-Stokes zu Stokes Intensität zu beobachten, da die eingehende Resonanz in diesem Fall nur für den Anti-Stokes Mn Spin Flip auftrat.

Summary

Main focus of the present dissertation was to gain new insight about the interaction between magnetic ions and the conduction band of diluted magnetic semiconductors. This interaction in magnetic semiconductors with carrier concentrations near the metal-insulator transition (MIT) in an external magnetic field is barely researched. Hence, n-doped $Zn_{1-x}Mn_xSe$:Cl samples were provided by the group of Dr. Hetterich of the Karlsruher Institut für Technologie (KIT). The studied set of samples consists of carrier concentrations between nominally undoped and up to $n_{Cl} \approx 10^{18}$ cm^{-3} and manganese concentrations between $x = 0.01$ and $x = 0.07$. Due to the objective of this dissertation special attention was paid during the sample fabrication, to get samples with carrier concentration close to the MIT of $n_{crit} = 7{\cdot}10^{17}$ cm^{-3} for ZnSe.
Resonant Raman spectroscopy was employed at an external magnetic field between 1 T and 7 T and a temperature of 1.5 K. Due to the low temperature, the spins of the manganese ions align already parallel at weak external magnetic fields. The resulting magnetization of the material amplifies the splitting of states with opposite spins both in the valence and the conduction band. This is known as the "giant-Zeeman-effect".
In this thesis, the resonance of the electron spin flip process, i.e. the enhancement of the signal depending on the excitation energy, was used as an indicator to determine the density of states of the charge carriers. The measured resonance profiles of each sample showed a structure, which consist of two partially overlapping Gaussian curves. The analysis of the Gaussian curves revealed that their respective maxima are separated independent of the magnetic field strenght by about 5 meV, which matches the binding energy of the donor bound exciton (D^0, X). Consequently, the electron spin flip process utilizes the free or the bound exciton as excited intermediate states, which can be addressed separately.
A widening of the full width at half maximum of the resonance profile was

observed with increasing magnetic field. A detailed analysis of this behavior showed that the donor bound exciton spin flip resonance primarily accounts for the widening for all samples with doping concentrations below the metal insulator transition. A model was proposed for the interpretation of this observation. This is based on the fundamental assumptions of a spatially random distribution of the manganese ions on the group-II sublattice of the ZnSe crystal and the finite extension of the excitons. Thus, each exciton covers an individual quantity of manganese ions, which manifest as a local manganese concentration. This local manganese concentration is normally distributed for a set of excitons and hence, the evaluation of the distribution allows the determination of exciton radii. The obtained radii lie between 1.55 nm and 5.90 nm for the (D^0, X) and between 2.09 nm and 11.5 nm for the free exciton.

Two trends were identified for the (D^0, X) radii. The radius of the bound exciton decreases with increasing carrier concentration as well as with increasing manganese concentration. The determination of the (D^0, X) radii by the use of resonant spin flip Raman spectroscopy and also the observation of the behavior of the (D^0, X) radius depending on the carrier concentration, was achieved for the first time.

For all samples with carrier concentrations below the metal-insulator transition, the obtained (X^0) radii are up to a factor of 5.9 larger than the respective (D^0, X) radii. This observation is explained by the unbound character of the (X^0). As a result, in comparison to the (D^0, X) the (X^0) encompass a larger area of the crystal during their lifetime. This reduces the influence of the fluctuating local manganese concentration on the (X^0) energy levels, which leads to a narrower energy distribution of the (X^0) energy levels and consequently, also to a reduction of the FWHM of the ESFRS resonance. The determined (X^0) radius of the highly doped sample must be pointed out. It is 2.09 nm, which only about 1.3 times larger than the (D^0, X) radius of this sample. A possible cause of this observation can be the scattering of the excitons on free carriers, which exists for this sample even at low temperatures. Thereby, the lifetime of the excitons is shortened, which reduced the captured volume by the excitons and therefore is equivalent to a smaller exciton radius. For the first time, such an observation could be made by Raman spectroscopy

Beside the resonance studies, the shape of the Raman signal of the electron spin flip was analyzed. Thereby an obvious asymmetry of the signal, with a clear flank to lower Raman shifts, was observed. This asymmetry is most

pronounced, when the spin flip process is excited near the (D^0, X) resonance. To explain this observation, a theoretical model was introduced in this thesis. Based on the asymmetry of the resonantly excited spin flip signal, it was possible to estimate the (D^0, X) radii, too. At external magnetic fields between 1.25 T and 7 T, the obtained radii lie between 2.38 nm and 2.75 nm. Within the context of measurement accuracy, these values match the determined radii by the resonance widening.

Additionally, the asymmetry of the electron spin flip signal was observed at different excitation energies. Here it is striking that the asymmetry vanishes with increasing excitation energy. At the highest excitation energy, where the electron spin flip was still detectable, the estimated radius of the exciton is 3.92 nm. This can be explained by the transition from the (D^0, X) dominated to the (X^0) resonance regime of the electron spin flip process. The deviation of the determined (X^0) radius in comparison to the value obtained by the analysis of the widening of the resonance profile, is primarily attributed to the increased uncertainty of this analysis method, when the asymmetry significantly decreases.

Beside the observations on the electron spin flip, the resonance behavior of the spin flip processes in the d-shell of the incorporated Mn ions was studied in this thesis. This was performed for the direct Mn spin flip process as well as for the sum process of the longitudinal optical phonon with the Mn spin flip. For the Stokes and anti-Stokes direct spin flip process and for the Stokes sum process, each the resonance curve is described by considering only one resonance mechanism. In contrast, resonance for the sum process in which an anti-Stokes Mn spin flip is involved, consists of two partially overlapping resonances due to different mechanisms. A detailed analysis of this resonance profile showed that for (Zn,Mn)Se at the chosen experimental parameters, an incoming and outgoing resonance can be achieved, separated by a few meV. The additional occurring resonance was assigned to the transition between the m_j = 1/2 valence and the m_j = -1/2 conduction band. The subsequent excitation of the LO phonon reduces the energy of the scattered photon, which leads to the observed overlapping of the two resonance contributions, when they are measured in the energy of the scattered photon. Hereby, at a specific excitation energy range and a high excitation power, it was possible to achieve an inversion of the anti-Stokes to Stokes intensity, because only the anti-Stokes Mn spin flip process was enhanced resonantly.

Bibliography

[AAC84] Aoki, K. ; Anastassakis, E. ; Cardona, M.: Dependence of Raman frequencies and scattering intensities on pressure in GaSb, InAs, and InSb semiconductors. In: *Phys. Rev. B* 30 (1984), Jul, 681–687. http://dx.doi.org/10.1103/PhysRevB.30.681. – DOI 10.1103/PhysRevB.30.681

[ADKH06] Agarwal, K. C. ; Daniel, B. ; Klingshirn, C. ; Hetterich, M.: Phonon and free-charge-carrier properties of $Zn_{1-x}Mn_xSe$ epilayers grown by molecular-beam epitaxy. In: *Phys. Rev. B* 73 (2006), Jan, 045211. http://dx.doi.org/10.1103/PhysRevB.73.045211. – DOI 10.1103/PhysRevB.73.045211

[BBK+86] Bylsma, R. B. ; Becker, W. M. ; Kossut, J. ; Debska, U. ; Yoder-Short, D.: Dependence of energy gap on x and T in $Zn_{1-x}Mn_xSe$: The role of exchange interaction. In: *Phys. Rev. B* 33 (1986), Jun, 8207–8215. http://dx.doi.org/10.1103/PhysRevB.33.8207. – DOI 10.1103/PhysRevB.33.8207

[Beh58] Behringer, Robert E.: Number of Single, Double, and Triple Clusters in a System Containing Two Types of Atoms. In: *The Journal of Chemical Physics* 29 (1958), Nr. 3, 537-539. http://dx.doi.org/10.1063/1.1744537. – DOI 10.1063/1.1744537

[BFC83] Bhattacharjee, A.K. ; Fishman, G. ; Coqblin, B.: Virtual bound state model for the exchange interaction in semimagnetic semiconductors such as $Cd_{1-x}Mn_xTe$. In: *Physica B+C* 117-118 (1983), 449 - 451. http://dx.doi.org/https://doi.org/10.1016/0378-4363(83)90555-7. – DOI https://doi.org/10.1016/0378–4363(83)90555–7. – ISSN 0378–4363

[BS92] Bergmann, L. ; Schaefer, C.: *Lehrbuch der Experimentalphysik, Festkörper*. Bd. 6. de Gruyter, 1992

[CC88] Cohen, M.L. ; Chelikowsky, J.R.: *Electronic Structure and Optical Properties of Semiconductors*. Springer, Berlin, Heidelberg, 1988

[CPS93] Capozzi, Vito ; Pavesi, Lorenzo ; Staehli, Jean L.: Exciton-carrier scattering in gallium selenide. In: *Phys. Rev. B* 47 (1993), Mar, 6340–6349. http://dx.doi.org/10.1103/PhysRevB.47.6340. – DOI 10.1103/PhysRevB.47.6340

[DNS84] Douglas, K. ; Nakashima, S. ; Scott, J. F.: Spin-flip light scattering in semimagnetic semiconductors $Cd_{1-x}Mn_xS$ and $Zn_{1-x}Mn_xSe$. In: *Phys. Rev. B* 29 (1984), May, 5602–5610. http://dx.doi.org/10.1103/PhysRevB.29.5602. – DOI 10.1103/PhysRevB.29.5602

[DRA+91] Dzhafarova, S. Z. ; Ragimova, N. A. ; Abutalybov, G. I. ; Guseinov, A. M. ; Abdinov, A. S.: Effect of Doping on Exciton States in InSe and GaSe Lamellar Semiconductors. In: *physica status solidi (a)* 128 (1991), Nr. 1, 235-242. http://dx.doi.org/10.1002/pssa.2211280126. – DOI 10.1002/pssa.2211280126

[DSP+88] DePuydt, J.M. ; Smith, T.L. ; Potts, J.E. ; Cheng, H. ; Mohapatra, S.K.: Detection and control of impurity incorporation in MBE-grown ZnSe. In: *Journal of Crystal Growth* 86 (1988), Nr. 1, 318 - 323. http://dx.doi.org/http://dx.doi.org/10.1016/0022-0248(90)90736-5. – DOI http://dx.doi.org/10.1016/0022–0248(90)90736–5. – ISSN 0022–0248

[FKR+99] Fiederling, R. ; Keim, M. ; Reuscher, G. ; Ossau, W. ; Schmidt, G. ; Waag, A. ; Molenkamp, L. W.: Injection and detection of a spin-polarized current in a light-emitting diode. In: *Nature* 402 (1999), Dec, 787 - 790. http://dx.doi.org/10.1038/45502

[Fur88] Furdyna, J. K.: Diluted magnetic semiconductors. In: *Journal of Applied Physics* 64 (1988), Nr. 4, R29-R64. http://dx.doi.org/10.1063/1.341700. – DOI 10.1063/1.341700

[Gas12] Gasiorowicz, S.: *Quantenphysik*. Bd. 10. Oldenbourg Wissenschaftsverlag, 2012

[Geu93] Geurts, J.: Analysis of band bending at III-V semiconductor interfaces by Raman spectroscopy. In: *Surface Science Reports* 18 (1993), Nr. 1, 1 - 89. http://dx.doi.org/https://doi.org/10.1016/0167-5729(93)90015-H. – DOI https://doi.org/10.1016/0167–5729(93)90015–H. – ISSN 0167–5729

[GK10] Gaj, J.A. ; Kossut, J.: *Introduction to the Physics of Diluted Magnetic Semiconductors*. Bd. 1. Springer-Verlag Berlin Heidelberg, 2010. http://dx.doi.org/10.1007/978-3-642-15856-8. http://dx.doi.org/10.1007/978-3-642-15856-8

[GPK90] Gutowski, J. ; Presser, N. ; Kudlek, G.: Optical Properties of ZnSe Epilayers and Films. In: *physica status solidi (a)* 120 (1990), Nr. 1, 11–59. http://dx.doi.org/10.1002/pssa.2211200102. – DOI 10.1002/pssa.2211200102. – ISSN 1521–396X

[HBK+86] Heiman, D. ; Becla, P. ; Kershaw, R. ; Ridgley, D. ; Dwight, K. ; Wold, A. ; Galazka, R. R.: Field-induced exchange effects in (Cd,Mn)Te and (Cd,Mn)Se from photoluminescence measurements. In: *Phys. Rev. B* 34 (1986), Sep, 3961–3969. http://dx.doi.org/10.1103/PhysRevB.34.3961. – DOI 10.1103/PhysRevB.34.3961

[HGT+93] Heimbrodt, W. ; Goede, O. ; Tschentscher, I. ; Weinhold, V. ; Klimakow, A. ; Pohl, U. ; Jacobs, K. ; Hoffmann, N.: Optical study of octahedrally and tetrahedrally coordinated MnSe. In: *Physica B: Condensed Matter* 185 (1993), Nr. 1, 357 - 361. http://dx.doi.org/https://doi.org/10.1016/0921-4526(93)90261-4. – DOI https://doi.org/10.1016/0921–4526(93)90261–4. – ISSN 0921–4526

[HK04] Heimbrodt, W. ; Klar, P. J.: *Encycl. Nanosci. Nanotechnol.*. Bd. 4. 2004. – 835 S.

[HMW93] Hirsch, M. ; Meyer, R. ; Waag, A.: Excitons as intermediate states in spin-flip Raman scattering of electrons bound to donors

in $Cd_{1-x}Mn_xTe$ epilayers. In: *Phys. Rev. B* 48 (1993), Aug, 5217–5224. http://dx.doi.org/10.1103/PhysRevB.48.5217. – DOI 10.1103/PhysRevB.48.5217

[Hum72] Humphreys, L. B.: Ionic Raman Effect. III. First- and Second-Order Ionic Raman Effects. In: *Phys. Rev. B* 6 (1972), Nov, 3886–3897. http://dx.doi.org/10.1103/PhysRevB.6.3886. – DOI 10.1103/PhysRevB.6.3886

[HWW83] Heiman, D. ; Wolff, P. A. ; Warnock, J.: Spin-flip Raman scattering, bound magnetic polaron, and fluctuations in (Cd,Mn)Se. In: *Phys. Rev. B* 27 (1983), Apr, 4848–4860. http://dx.doi.org/10.1103/PhysRevB.27.4848. – DOI 10.1103/PhysRevB.27.4848

[JBGO08] Jansson, F. ; Baranovskii, S. D. ; Gebhard, F. ; Österbacka, R.: Effective temperature for hopping transport in a Gaussian density of states. In: *Phys. Rev. B* 77 (2008), May, 195211. http://dx.doi.org/10.1103/PhysRevB.77.195211. – DOI 10.1103/PhysRevB.77.195211

[JWN+14] Jansson, F. ; Wiemer, M. ; Nenashev, A. V. ; Petznick, S. ; Klar, P. J. ; Hetterich, M. ; Gebhard, F. ; Baranovskii, S. D.: Large positive magnetoresistance effects in the dilute magnetic semiconductor (Zn,Mn)Se in the regime of electron hopping. In: *Journal of Applied Physics* 116 (2014), Nr. 8, 083710. http://dx.doi.org/10.1063/1.4894236. – DOI 10.1063/1.4894236

[KH81] Klingshirn, C. ; Haug, H.: Optical properties of highly excited direct gap semiconductors. In: *Physics Reports* 70 (1981), Nr. 5, 315 - 398. http://dx.doi.org/https://doi.org/10.1016/0370-1573(81)90190-3. – DOI https://doi.org/10.1016/0370–1573(81)90190–3. – ISSN 0370–1573

[KM97] Kavokin, K. V. ; Merkulov, I. A.: Multispin Raman paramagnetic resonance: Quantum dynamics of classically large angular momenta. In: *Phys. Rev. B* 55 (1997), Mar, R7371–

R7374. http://dx.doi.org/10.1103/PhysRevB.55.R7371. – DOI 10.1103/PhysRevB.55.R7371

[KMY+99] Kavokin, K. V. ; Merkulov, I. A. ; Yakovlev, D. R. ; Ossau, W. ; Landwehr, G.: Exciton localization in semimagnetic semiconductors probed by magnetic polarons. In: *Phys. Rev. B* 60 (1999), Dec, 16499–16505. http://dx.doi.org/10.1103/PhysRevB.60.16499. – DOI 10.1103/PhysRevB.60.16499

[KMY+00] König, B. ; Merkulov, I. A. ; Yakovlev, D. R. ; Ossau, W. ; Ryabchenko, S. M. ; Kutrowski, M. ; Wojtowicz, T. ; Karczewski, G. ; Kossut, J.: Energy transfer from photocarriers into the magnetic ion system mediated by a two-dimensional electron gas in (Cd,Mn)Te/(Cd,Mg)Te quantum wells. In: *Phys. Rev. B* 61 (2000), Jun, 16870–16882. http://dx.doi.org/10.1103/PhysRevB.61.16870. – DOI 10.1103/PhysRevB.61.16870

[KYK+01] Keller, D. ; Yakovlev, D. R. ; König, B. ; Ossau, W. ; Gruber, Th. ; Waag, A. ; Molenkamp, L. W. ; Scherbakov, A. V.: Heating of the magnetic ion system in (Zn, Mn)Se/(Zn, Be)Se semimagnetic quantum wells by means of photoexcitation. In: *Phys. Rev. B* 65 (2001), Dec, 035313. http://dx.doi.org/10.1103/PhysRevB.65.035313. – DOI 10.1103/PhysRevB.65.035313

[LE89] Larson, B. E. ; Ehrenreich, H.: Anisotropic superexchange and spin-resonance linewidth in diluted magnetic semiconductors. In: *Phys. Rev. B* 39 (1989), Jan, 1747–1759. http://dx.doi.org/10.1103/PhysRevB.39.1747. – DOI 10.1103/PhysRevB.39.1747

[LGG+07] Lentze, M. ; Grabs, P. ; Geurts, J. ; Rönneburg, K. ; Mohler, E. ; Roskos, H.: Carrier-density dependence of the exchange coupling between magnetic Ions and conduction band electrons in heavily -Type $Zn_{1-x}Mn_xSe$ and optically pumped $Cd_{1-x}Mn_xTe$. In: *International Journal of Modern Physics B* 21 (2007), Nr. 08n09, 1632-1637. http://dx.doi.org/10.1142/S0217979207043336. – DOI 10.1142/S0217979207043336

[Liu61] Liu, S. H.: Exchange Interaction between Conduction Electrons and Magnetic Shell Electrons in Rare-Earth Metals. In: *Phys.*

Rev. 121 (1961), Jan, 451–455. http://dx.doi.org/10.1103/PhysRev.121.451. – DOI 10.1103/PhysRev.121.451

[Lou63] Loudon, R.: Theory of the first-order Raman effect in crystals. In: *Proceedings of the Royal Society of London A: Mathematical, Physical and Engineering Sciences* 275 (1963), Nr. 1361, 218–232. http://dx.doi.org/10.1098/rspa.1963.0166. – DOI 10.1098/rspa.1963.0166. – ISSN 0080–4630

[LRA88] Lee, Y. R. ; Ramdas, A. K. ; Aggarwal, R. L.: Energy gap, excitonic, and "internal" Mn^{2+} optical transition in Mn-based II-VI diluted magnetic semiconductors. In: *Phys. Rev. B* 38 (1988), Nov, 10600–10610. http://dx.doi.org/10.1103/PhysRevB.38.10600. – DOI 10.1103/PhysRevB.38.10600

[MI11] Momma, Koichi ; Izumi, Fujio: *VESTA3* for three-dimensional visualization of crystal, volumetric and morphology data. In: *Journal of Applied Crystallography* 44 (2011), Dec, Nr. 6, 1272–1276. http://dx.doi.org/10.1107/S0021889811038970. – DOI 10.1107/S0021889811038970

[MMB80] McIntyre, G. J. ; Moss, G. ; Barnea, Z.: Anharmonic temperature factors of zinc selenide determined by X-ray diffraction from an extended-face crystal. In: *Acta Crystallographica Section A* 36 (1980), May, Nr. 3, 482–490. http://dx.doi.org/10.1107/S0567739480001003. – DOI 10.1107/S0567739480001003

[Mor60] Moriya, Tôru: Anisotropic Superexchange Interaction and Weak Ferromagnetism. In: *Phys. Rev.* 120 (1960), Oct, 91–98. http://dx.doi.org/10.1103/PhysRev.120.91. – DOI 10.1103/PhysRev.120.91

[MRS] Madelung, O. ; Rössler, U. ; Schulz, M.: *Zinc selenide (ZnSe) band structure: Datasheet from Landolt-Börnstein - Group III Condensed Matter · Volume 41B: "II-VI and I-VII Compounds; Semimagnetic Compounds" in SpringerMaterials (http://dx.doi.org/10.1007/10681719_413).* http://dx.doi.org/10.1007/10681719_413. – Copyright 1999 Springer-Verlag Berlin Heidelberg

[MRS01] Madelung, O. ; Rössler, U. ; Schulz, M.: *Gallium arsenide (GaAs) lattice parameters, thermal expansion: Datasheet from Landolt-Börnstein - Group III Condensed Matter · Volume 41A1α: "Group IV Elements, IV-IV and III-V Compounds. Part a - Lattice Properties" in SpringerMaterials (http://dx.doi.org/10.1007/10551045_104).* http://dx.doi.org/10.1007/10551045_104. Version: 2001. – Copyright 2001 Springer-Verlag Berlin Heidelberg

[NGM+80] Nagata, Shoichi ; Galazka, R. R. ; Mullin, D. P. ; Akbarzadeh, H. ; Khattak, G. D. ; Furdyna, J. K. ; Keesom, P. H.: Magnetic susceptibility, specific heat, and the spin-glass transition in $Hg_{1-x}Mn_xTe$. In: *Phys. Rev. B* 22 (1980), Oct, 3331–3343. http://dx.doi.org/10.1103/PhysRevB.22.3331. – DOI 10.1103/PhysRevB.22.3331

[NJW+13] Nenashev, A. V. ; Jansson, F. ; Wiemer, M. ; Petznick, S. ; Klar, P. J. ; Hetterich, M. ; Dvurechenskii, A. V. ; Gebhard, F. ; Baranovskii, S. D.: Scaling approach to hopping magnetoresistivity in dilute magnetic semiconductors. In: *Phys. Rev. B* 88 (2013), Sep, 115210. http://dx.doi.org/10.1103/PhysRevB.88.115210. – DOI 10.1103/PhysRevB.88.115210

[NPFG81] Nawrocki, M. ; Planel, R. ; Fishman, G. ; Galazka, R.: Exchange-Induced Spin-Flip Raman Scattering in a Semimagnetic Semiconductor. In: *Phys. Rev. Lett.* 46 (1981), Mar, 735–738. http://dx.doi.org/10.1103/PhysRevLett.46.735. – DOI 10.1103/PhysRevLett.46.735

[NST03] Nazmul, Ahsan M. ; Sugahara, S. ; Tanaka, M.: Ferromagnetism and high Curie temperature in semiconductor heterostructures with Mn δ-doped GaAs and p-type selective doping. In: *Phys. Rev. B* 67 (2003), Jun, 241308. http://dx.doi.org/10.1103/PhysRevB.67.241308. – DOI 10.1103/PhysRevB.67.241308

[PPV+83] Petrou, A. ; Peterson, D. L. ; Venugopalan, S. ; Galazka, R. R. ; Ramdas, A. K. ; Rodriguez, S.: Raman scattering study of the magnetic excitations in diluted magnetic semiconductors in the presence of an external magnetic field. In: *Phys.*

Rev. B 27 (1983), Mar, 3471–3482. http://dx.doi.org/10.1103/PhysRevB.27.3471. – DOI 10.1103/PhysRevB.27.3471

[Ric68] Riccius, H. D.: Infrared Lattice Vibrations of Zinc Selenide and Zinc Telluride. In: *Journal of Applied Physics* 39 (1968), August, S. 4381–4382. http://dx.doi.org/10.1063/1.1656980. – DOI 10.1063/1.1656980

[RK28] Raman, C. V. ; Krishnan, K. S.: A New Type of Secondary Radiation. In: *Nature* 121 (1928), Mar, 501-502. http://dx.doi.org/10.1038/121501c0

[SFR+84] Shapira, Y. ; Foner, S. ; Ridgley, D. H. ; Dwight, K. ; Wold, A.: Technical saturation and magnetization steps in diluted magnetic semiconductors: Predictions and observations. In: *Phys. Rev. B* 30 (1984), Oct, 4021–4023. http://dx.doi.org/10.1103/PhysRevB.30.4021. – DOI 10.1103/PhysRevB.30.4021

[SO87] Shapira, Y. ; Oliveira, N. F.: High-field magnetization steps and the nearest-neighbor exchange constant in $Cd_{1-x}Mn_xS$, $Cd_{1-x}Mn_xTe$, and $Zn_{1-x}Mn_xSe$. In: *Phys. Rev. B* 35 (1987), May, 6888–6893. http://dx.doi.org/10.1103/PhysRevB.35.6888. – DOI 10.1103/PhysRevB.35.6888

[SSD+95] Stühler, J. ; Schaack, G. ; Dahl, M. ; Waag, A. ; Landwehr, G. ; Kavokin, K. V. ; Merkulov, I. A.: Multiple Mn^{2+}-Spin-Flip Raman Scattering at High Fields via Magnetic Polaron States in Semimagnetic Quantum Wells. In: *Phys. Rev. Lett.* 74 (1995), Mar, 2567–2570. http://dx.doi.org/10.1103/PhysRevLett.74.2567. – DOI 10.1103/PhysRevLett.74.2567

[TAT+99] Takeyama, S. ; Adachi, S. ; Takagi, Y. ; Karczewski, G. ; Wojtowicz, T. ; Kossut, J. ; Karasawa, T.: Photo-induced magnetic polarons in low-dimensional dilute magnetic semiconductors. In: *Materials Science and Engineering: B* 63 (1999), Nr. 1, 111 - 118. http://dx.doi.org/https://doi.org/10.1016/S0921-5107(99)00060-4. – DOI https://doi.org/10.1016/S0921–5107(99)00060–4. – ISSN 0921–5107

[TMR+04] Tsoi, S. ; Miotkowski, I. ; Rodriguez, S. ; Ramdas, A. K. ; Alawadhi, H. ; Pekarek, T. M.: Resonant electron spin-flip Raman scattering in CdTe and the diluted magnetic semiconductor $Cd_{1-x}V_xTe$. In: *Phys. Rev. B* 69 (2004), Jan, 035209. http://dx.doi.org/10.1103/PhysRevB.69.035209. – DOI 10.1103/PhysRevB.69.035209

[TODP84] Twardowski, A. ; Ortenberg, M. von ; Demianiuk, M. ; Pauthenet, R.: Magnetization and exchange constants in $Zn_{1-x}Mn_xSe$. In: *Solid State Communications* 51 (1984), Nr. 11, 849 - 852. http://dx.doi.org/http://dx.doi.org/10.1016/0038-1098(84)91085-8. – DOI http://dx.doi.org/10.1016/0038–1098(84)91085–8. – ISSN 0038–1098

[WGR+97] Wörz, M. ; Griebl, E. ; Reisinger, Th. ; Flierl, R. ; Haserer, B. ; Semmler, T. ; Frey, T. ; Gebhardt, W.: Gap Energies, Exciton Binding Energies and Band Offsets in Ternary ZnMgSe Compounds and ZnSe/ZnMgSe Heterostructures. In: *physica status solidi (b)* 202 (1997), Nr. 2, 805–816. http://dx.doi.org/10.1002/1521-3951(199708)202:2<805::AID-PSSB805>3.0.CO;2-O. – DOI 10.1002/1521–3951(199708)202:2<805::AID–PSSB805>3.0.CO;2–O. – ISSN 1521–3951

[YC10] Yu, P. ; Cardona, M.: *Fundamentals of Semiconductors*. Bd. 4. Springer-Verlag Berlin Heidelberg, 2010. http://dx.doi.org/10.1007/978-3-642-00710-1. http://dx.doi.org/10.1007/978-3-642-00710-1

[YSDF85] Yoder-Short, D. R. ; Debska, U. ; Furdyna, J. K.: Lattice parameters of $Zn_{1-x}Mn_xSe$ and tetrahedral bond lengths in $A^{II}_{1-x}Mn_xBVI$ alloys. In: *Journal of Applied Physics* 58 (1985), Nr. 11, 4056-4060. http://dx.doi.org/10.1063/1.335585. – DOI 10.1063/1.335585

Appendix A

Monte Carlo simulations of the local Mn concentration distribution

A finding of this thesis are the estimated radii of the (D^0,X) and (X^0) in n-doped (Zn,Mn)Se. The key element to calculate the radii is based on the spatial distribution of the Mn ions within the (Zn,Mn)Se crystal and the finite size of the excitons. Thus, each of these excitons encompasses a particular number of Mn ions, also described by a local Mn concentration x_{loc}. For a large set of excitons, x_{loc} is described by a binomial distribution.
A two dimensional grid is drawn in Fig. A.1, representing a simplified, two dimensional visualization of a crystal. The crossing points of the grid represent atomic sites and the gray stars are randomly distributed Mn ions. Differently sized excitons are shown by the black, dashed, dotted and dashed-dotted circles. Not surprisingly, the total number of the magnetic ions within the exciton dependence on its size. With increasing exciton size, the effect of the Mn fluctuations on the concentration within the area of the exciton becomes less significant and the number of Mn ions per atomic site, i.e. the local Mn concentration x_{loc}, converges to the mean concentration value.
No interaction between the Mn ions is considered, thus all values presented in this section represent the local chemical concentration. It should be noted that for magneto optical experiments, e.g. electron spin flip Raman spectroscopy, the splitting of the CB and VB is described by Eqs. (1.28) and (1.29). Here the effective concentration is used to include the anti-ferromagnetic interac-

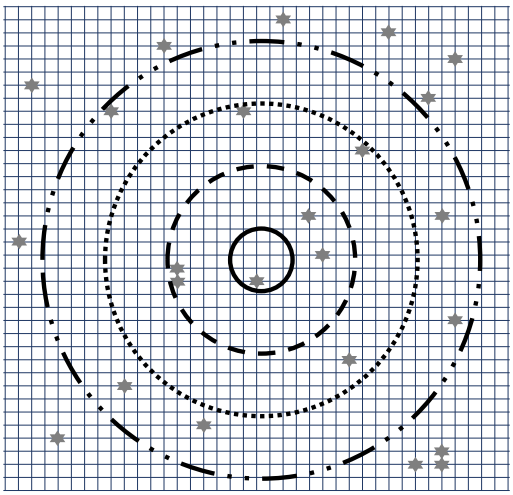

Figure A.1: Visualization of excitons with different sizes, which are shown by the black solid, dashed, dotted and dashed dotted circles. The grid represents the crystal, in which the excitons are located and each crossing point of the grid is a cation site. The gray stars are magnetic ions, randomly positioned on the cation sites.

tion of neighboring Mn ions. Therefore when comparing the results obtained by by ESFRS measurements with the here presented Monte Carlo simulations transition from x to x_{eff} according to Eq. (1.24) must be considered.

The Monte Carlo simulations are performed to verify the assumption that with increasing size of the excitons, the relevant local concentration within its expansion range tends to the average chemical concentration x_0. The input parameters of the simulations are as follows:

- the simulated ensemble consists of 40 excitons
- A Bernoulli process is assumed, where the cation sites are either occupied by a magnetic ion with probability p or by a non magnetic ion with probability $q = (1-p)$. The probabilities are set to $p = 0.05$ and $q = 0.95$, because these parameters are identical to the chemical composition of most of the studied $Zn_{(1-x)}Mn_xSe$ samples.
- For each iteration step, the size is increased by one cation site and the total number of Mn ions is counted. The local concentration is defined as the number of Mn ions per cation site.

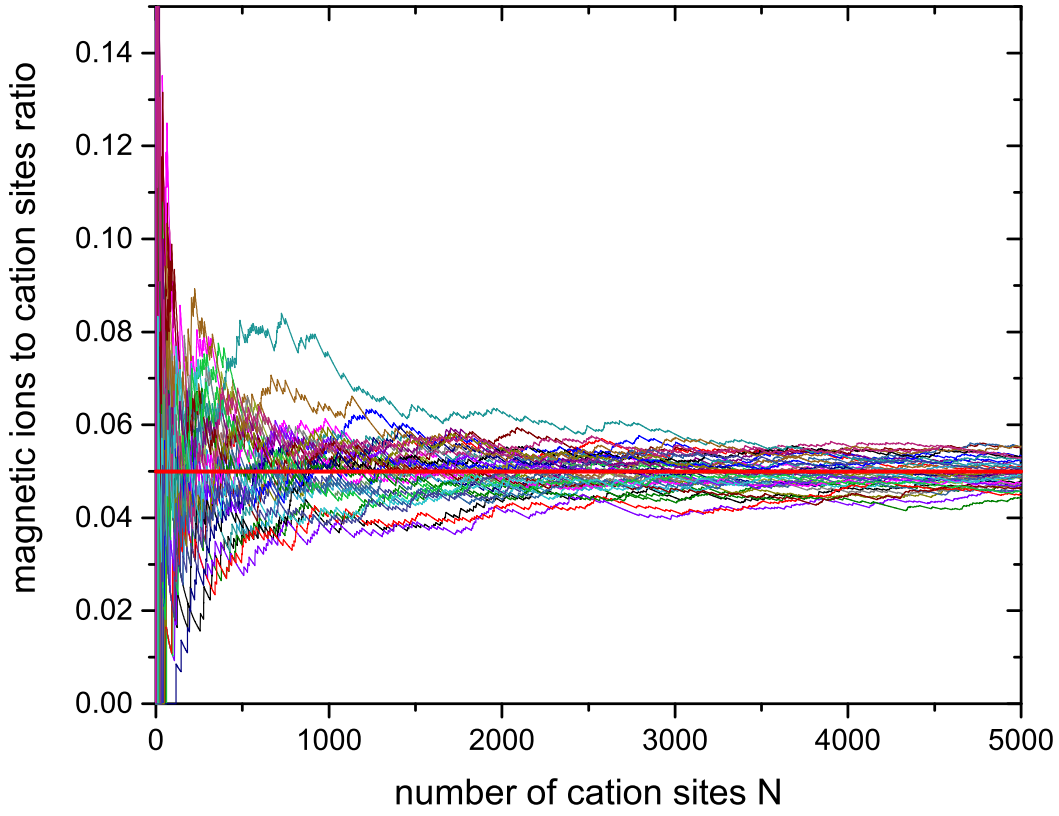

Figure A.2: Simulated magnetic ions to cation sites ratio (i.e. local concentration x_{loc}) for 40 excitons in dependence of the absolute number of cation sites N, with probability of occupancy of the magnetic ion $p = 0.05$. For low N a distinct variation of x_{loc} occurs. For increasing N, x_{loc} approaches the expectancy value 0.05, denoted by the red horizontal line.

The result is plotted in Fig. A.2. Each curve represents the ratio of magnetic ions to the total number of cation sites for one exciton. For a low number of cation sites, i.e. a small excitons, a pronounced variation of the local concentration for the set of excitons is observed. This is particularly striking at the first simulation step. The local Mn concentration converges to $p = 0.05$ with increasing exciton size and consequently, the variation of the concentrations between the individual excitons becomes less pronounced. Hence, the width of the local concentration distribution allows an inference of the average exciton size.

To quantitatively analyze the distribution width, a second simulation is performed. Here, the local concentrations of 1000 excitons, each with six different numbers of cation sites N (N$\in \{20; 50; 100; 250; 500; 1000\}$) are simulated. The frequency distributions of the magnetic ions to cation sites ratio are shown as

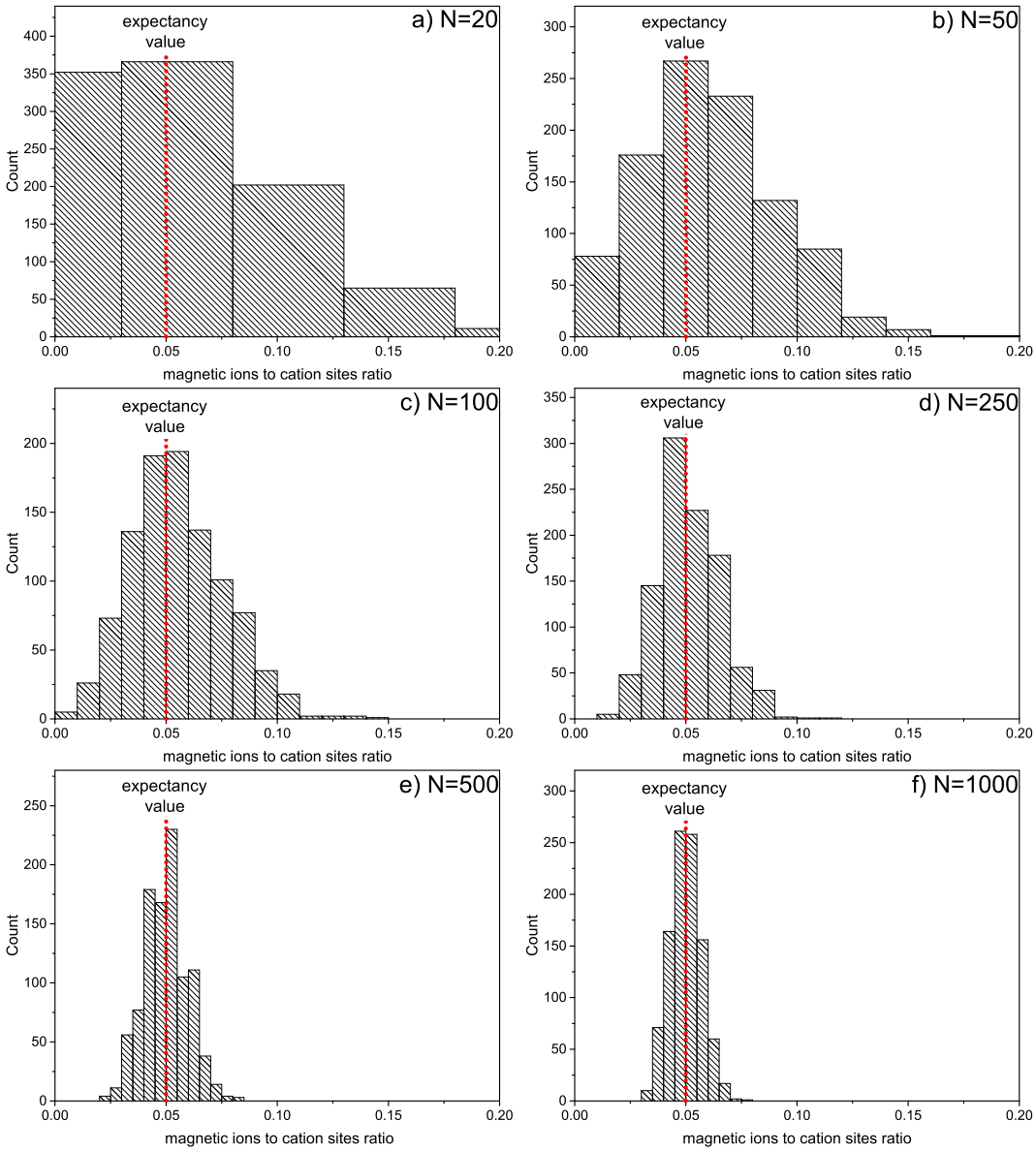

Figure A.3: Histograms of simulated magnetic ions to cation sites ratio (i.e. local magnetic ion concentration x_{loc}) each for 1000 excitons, with probability $p = 0.05$ and cation sites sizes N ranging from $N = 20$ to 1000. The expectancy value 0.05 is marked by the red dotted lines. With increasing N, the distribution becomes narrower and resembles a normal distribution.

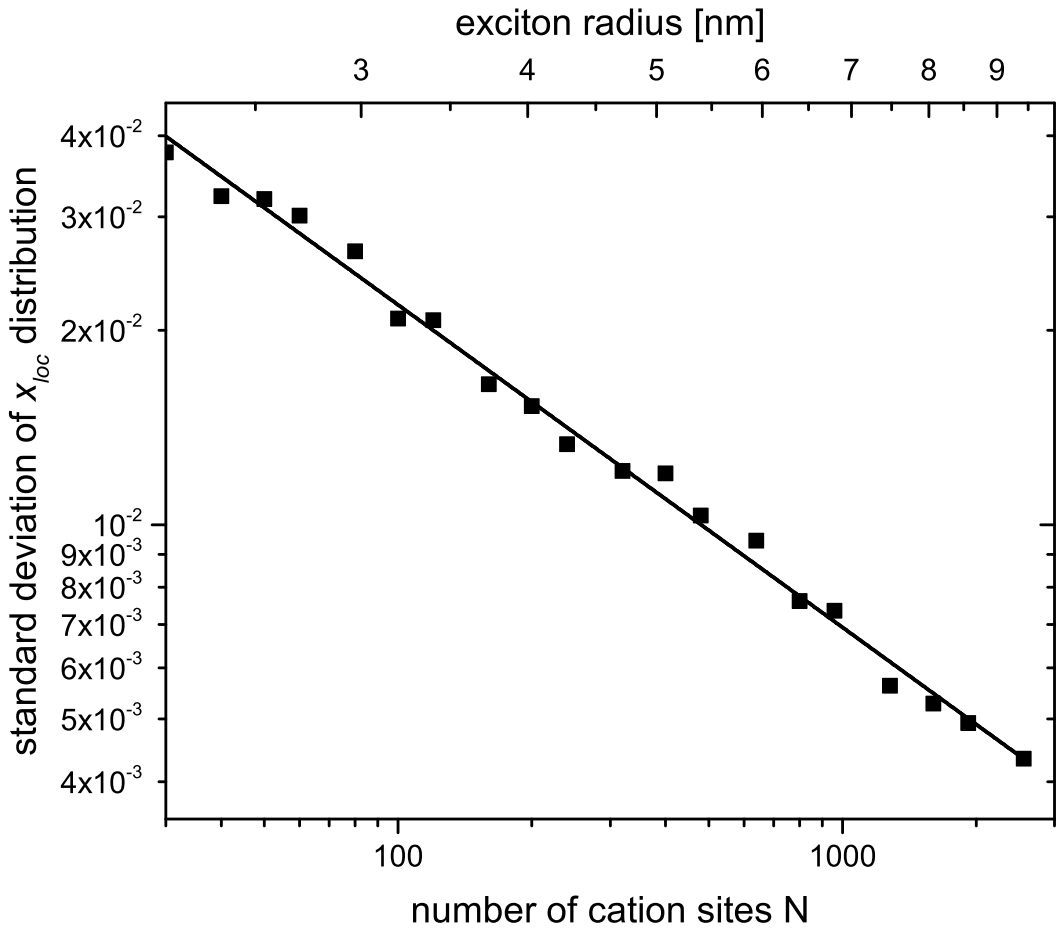

Figure A.4: Log-log plot of the standard deviation of the simulated x_{loc} distribution for different number of cation sites N. The linear curve is a polynomial fit to the data.

histograms in Fig. A.3 a) to f). The maximum of each histogram occurs at $x_{loc} = 0.05$, which is equal to the input parameter p. As expected for a Bernoulli process, for $N = 25$ and $N = 50$, the histogram is similar to a Poisson distribution, whereas for larger N the histogram resembles a normal distribution. Moreover, the width of the distribution becomes narrower with increasing N, strengthening the observed trend plotted in Fig. A.2.

To study this observation in more detail, each simulated distribution is fitted by a Gaussian, with the number of cation sites N ranging from 30 to 2560. The resulting standard deviation σ in dependence of the number of cation sites are presented as a log-log plot in Fig. A.4. In this scale, a striking linear decrease of $\sigma = 0.037$ at $N = 30$ to $\sigma = 0.004$ at $N = 2560$ is found. This indicates that $\sigma(N) = a \cdot N^b$ can be fitted to the data. The fit result yields $a = 0.218$ and

b = -0.50 and is plotted in Fig. A.4. The results of the simulated data are in a perfect agreement with the mathematically expected values, calculated by the mathematical properties of a binomial function $\sigma = \sqrt{p \cdot q}/\sqrt{N}$, which gives σ= 0.218 $N^{-1/2}$ for $p = 0.05$. This confirms that the analysis for the estimation of the (D^0,X) and (X^0) radii presented in section 4.2.3 is reasonable.

Appendix B

Formality

Publications and conferences

- *Investigation of the B -field-induced widening of the donor-electron energy distribution in n-doped (Zn,Mn)Se by resonant electron spin-flip Raman spectroscopy*, Knapp, A. G.; Hetterich, M. and Geurts, J., Journal of Physics Communications 2, 2, 2018

- *Electron spin flip Raman spectroscopy of the diluted magnetic semiconductor $Zn_{1-x}Mn_xSe$ below the metal-insulator transition*, Knapp, A. G.; Petznick, S.; Jansson, F.; Wiemer, M.; Hetterich, M.; Gebhard, F.; Baranovskii, S. D.; Klar, P. J. and Geurts, J., Physica Status Solidi (c) 13, 7-9, 542-545, 2016, https://doi.org/10.1002/pssc.201510267

- *Series of "fractional" peaks in multiple paramagnetic resonance Raman scattering by (Cd,Mn)Te quantum wells*, Koudinov, A. V.; Knapp, A.; Karczewski, G. and Geurts, J., Phys. Rev. B 96, 241303(R), 2017, https://doi.org/10.1103/PhysRevB.96.241303

- *Electrically Connected Resonant Optical Antennas*, Prangsma, J. C.; Kern, J.; Knapp, A. G.; Grossmann, S.; Emmerling, M.; Kamp, M. and Hecht, B., Nano Letters 12, 8, 3915-3919, 2012, https://doi.org/10.1021/nl3007374

- *Electron Spin Flip Raman Spectroscopy and Magneto-Resistance of the Diluted Magnetic Semiconductor $Zn_{1-x}Mn_xSe$ below the Metal-Insulator Transition*, conference contribution, 17th International Conference on II-VI Compounds and Related Materials, 2015, Paris

- *Determination of the Mn-spin temperature of photo-excited n-doped $Zn_{1-x}Mn_xSe$ by magneto-luminescence and spinflip Raman spectroscopy*, Beitrag zur Konferenz, Frühjahrstagung der Deutschen Physikalischen Gesellschaft 2015, Berlin

- *Electron Spin Flip Raman Spectroscopy of the Diluted Magnetic Semiconductor $Zn_{1-x}Mn_xSe$ below the Metal-Insulator Transition*, Beitrag zur Konferenz, Frühjahrstagung der Deutschen Physikalischen Gesellschaft 2016, Regensburg

Danksagungen

An dieser Stelle möchte ich mich nun bei denen bedanken, die bei der Durchführung der Doktorarbeit und dem Erstellung dieser Schrift direkt oder indirekt beigetragen haben:

- Meinem Doktorvater, Prof. Dr. Jean Geurts, für die Möglichkeit zur Durchführung der Doktorarbeit in seiner Arbeitsgruppe; den zahlreichen, didaktisch sehr hochwertigen Gesprächen bei denen es immer gelang, auch komplexe physikalische Sachverhalte sehr anschaulich zu verdeutlichen.

- Dem Zweitgutachter dieser Arbeit, Prof. Dr. Edwin Batke, für Begutachtung und die Bewertung dieser Dissertation.

- Herrn Priv.-Doz. Dr. Michael Hetterich, sowie seiner AG für die Herstellung der im Zuge dieser Arbeit untersuchten (Zn,Mn)Se:Cl Proben, denn hochwertige, spezifisch gefertigte Proben sind insbesondere für die Raman-Spektroskopie an Halbleitern unerlässlich.

- Den Kollegen der AG Geurts, insbesondere Sebastian, für den regelmäßigen Austausch zur eigenen wissenschaftlichen Arbeit, sowie hilfreiche Tipps und Tricks die Kryotechnik betreffend.

- Den Kooperationspartnern Prof. Dr. Klar und Prof. Dr. Baranovskii für die Transportuntersuchungen an den (Zn,Mn)Se:Cl Proben, sowie die Ausarbeitung eines theoretischen Modells zur Beschreibung der Transportphänomene, welches unter anderem Auslöser war, diese Dissertation durchzuführen.

- Den Kollegen aus der Heliumverflüssigung, die wichtige Ratschläge zur Kryotechnik geben konnten und mir immer zügig eine Kanne flüssiges Helium zur Verfügung gestellt haben, sodass ich meine Experimente ohne Verzögerung durchführen konnte.

- Der Kaffeerunde für die zahlreichen, immer wieder erhellenden und erfreuenden Gespräche, sowohl über Physik aber auch Gott und die Welt.

- Meinen Eltern für die allgemeine Unterstützung, nicht nur während der Promotion sondern bereits während der Schulzeit und dem Physikstudium.

- Meiner Freundin Eva dafür, dass sie mir immer zur Seite stand, gerade in Zeiten in denen die Arbeit stressig und anstrengend wurde.

- Der Sekretärin Angelika Berger für die immer eine große Hilfe bei der Bewältigung des Verwaltungsaufwandes.